NASA-CR-201077

Final Report

NASA
Grant NAG-5-902
UW 144-Z203

Lidar measurements of boundary Layers, aerosol scattering and clouds during project FIFE

Edwin W. Eloranta
Principal Investigator

University of Wisconsin
Department of Meteorology
1225 W. Dayton St.
Madison,Wis
Tel (608)-262-7327

May 9, 1995

1 Introduction

A detailed account of progress achieved under this grant funding is contained in five journal papers. The titles and authors of these papers are:

- Schols, J. and E. W. Eloranta, 1992: The calculation of area-averaged vertical profiles of the horizontal wind velocity using volume imaging lidar data, *Journal of Geophysical Research*, **97**, 18395-18408
- Eloranta, E. W. and D. K. Forrest, 1992: Volume imaging lidar observation of the convective structure surrounding the flight path of an instrumented aircraft, *Journal of Geophysical Research*, **97**, 18383-18394.
- Piironen, A. and E. W. Eloranta, 1995: Convective boundary layer mean depths, cloud base altitudes, cloud top altitudes, cloud coverages, and cloud shadows obtained from Volume Imaging Lidar data. Accepted for publication in the *Journal of Geophysical Research.*
- Piironen, A. and E. W. Eloranta, 1995: An accuracy analysis of the wind profiles calculated from Volume Imaging Lidar data. Accepted for publication in the *Journal of Geophysical Research.*
- Young, P. and E. W. Eloranta, 1995: Calculation of divergence and vertical motion from volume-imaging lidar data, Accepted for publication in the *Journal of Geophysical Research.*

Copies of these papers form the body of this report.

JOURNAL OF GEOPHYSICAL RESEARCH, VOL. 97, NO. D17, PAGES 18,395–18,407, NOVEMBER 30, 1992

Calculation of Area-Averaged Vertical Profiles of the Horizontal Wind Velocity From Volume-Imaging Lidar Data

J. L. SCHOLS[1] AND E. W. ELORANTA

Department of Meteorology, University of Wisconsin, Madison

Area-averaged horizontal wind measurements are derived from the motion of spatial inhomogeneities in aerosol backscattering observed with a volume-imaging lidar. Spatial averaging provides high precision, reducing sample variations of wind measurements well below the level of turbulent fluctuations, even under conditions of very light mean winds and strong convection or under the difficult conditions represented by roll convection. Wind velocities are measured using the two-dimensional spatial cross correlation computed between successive horizontal plane maps of aerosol backscattering, assembled from three-dimensional lidar scans. Prior to calculation of the correlation function, three crucial steps are performed: (1) the scans are corrected for image distortion by the wind during a finite scan time; (2) a temporal high pass median filtering is applied to eliminate structures that do not move with the wind; and (3) a histogram equalization is employed to reduce biases to the brightest features.

1. INTRODUCTION

Convective motions in an unstable atmospheric boundary layer produce fluctuations in wind speed and direction. These velocity fluctuations scale with the convective scaling velocity (w^*) and have typical magnitudes of 1 m s^{-1} [*Kaimal et al.*, 1976], which are spatially correlated within individual thermals. Thermal sizes scale on the boundary layer depth and have typical dimensions of the order of 1 km; when longitudinal rolls exist the stream-wise correlation length becomes much larger. These velocity fluctuations limit the accuracy with which the mean boundary layer wind can be estimated. To reduce errors in the mean much below w_*, instruments that make point measurements must rely on temporal averaging over a period that is long compared to the lifetime of a thermal or long compared to the time for a thermal to advect over the instrument. When the mean wind is small, the required averaging times become long. For example, with a 1 m s^{-1} mean wind and a 1-km-deep boundary layer, a single cell requires approximately 1000 s to pass a fixed sensor. Reduction of the sampling error to a level much below w_* requires the passage of many thermals; this in turn requires many hours of averaging.

Spatial averaging offers the possibility of reducing thermal-scale fluctuations in the wind without long averaging times. This paper describes a lidar technique for obtaining area-averaged winds measured using lidar observations of the drift of inhomogeneities in naturally occurring atmospheric aerosols. Spatial inhomogeneities in atmospheric boundary layer aerosol content are produced by a variety of processes, including localized sources, and by the vertical entrainment of air from above. The displacement of these inhomogeneities can be measured between successive observations by an incoherent lidar system. These displacements allow calculation of wind velocities without the use of Doppler techniques. Wind measurements have been obtained by calculating correlations between a time sequence of lidar profiles acquired from a small number of discrete lidar printing directions [*Eloranta et al.*, 1975; *Kunkel et al.*, 1980; *Sroga et al.*, 1980; *Hooper and Eloranta*, 1986; *Kolev et al.*, 1988] and by calculating cross correlations from a sequence of two dimensional lidar images [*Leese and Epstein*, 1963; *Sasano et al.*, 1982; *Ferrare et al.*, 1991].

The University of Wisconsin (UW) volume imaging lidar (VIL) is designed to produce a continuous sequence of three-dimensional maps of aerosol backscattering [*Eloranta*, 1987, 1988]. A relatively fast laser pulse repetition rate, fast angular beam scanning, and a fast data acquisition system allow this lidar to image atmospheric boundary layer (ABL) structure over an approximately 50- to 70-km^2 area at approximately 3- to 4-min intervals. Each volume image contains approximately 6 million measurements of aerosol backscattering.

In the present paper, lidar profiles observed with the VIL are used to produce images of the aerosol structure on vertically stacked horizontal planes. These images are compared to similar images obtained a short time later to obtain independent estimates of the wind velocity at the altitude of each plane. The vertical profiles of the horizontal wind obtained by this process represent an area average over ≈ 50 to 70 km^2.

2. METHOD OF DATA ANALYSIS

The backscattered power incident on the lidar receiver from a pulse of laser light is described by the single-scatter lidar equation [*Collis and Russell*, 1976], which, in a slightly modified form, reads

$$P(r) = \frac{E}{r^2}\frac{Ac}{2}\beta'(\pi, r)\exp\left(-2\int_0^r \beta_e(r')\,dr\right) \quad (1)$$

where

r = range from lidar;
$P(r)$ = received power;
E = transmitted laser pulse energy;
A = area of receiver;
c = speed of light;
$\beta'(\pi, r)$ = volume backscatter coefficient per steradian,

[1]Now at General Sciences Corporation, Laurel, Maryland.

Paper number 92JD01051.
0148-0227/92/92JD-01051$05.00

which is equal to the product of the aerosol scattering cross section, per unit volume and the aerosol backscatter phase function;

$\beta_e(r)$ = extinction cross section per unit volume.

Before recording lidar profiles on the optical disk, the VIL data system (1) normalizes each lidar profile to remove the energy variations between laser pulses, (2) corrects for the inverse range squared dependence; and (3) forms the natural logarithm of the normalized lidar profile. The recorded logarithm of the range corrected energy normalized data points S_{ij} are given by

$$S_{ij} = \ln\left(\frac{P_{ij} \cdot r_j^2}{E_i}\right) \tag{2}$$

where

$r_j = \delta r j$, the distance between the lidar and jth scattering range element;

i = index for ith lidar profile;

j = index for jth range element;

δr = range increment between successive data points.

As a first step in the data analysis each lidar profile is high-pass filtered by subtracting a moving median of data points in a range-centered interval around the jth range element. The filtered lidar profile, S_{ij}^f, is given by

$$S_{ij}^f = S_{ij} - S_{ij}^m \tag{3}$$

where

$$S_{ij}^m = \text{median}\ \{S_{il}\} \qquad j - n \le l \le j + n \tag{4}$$

and $2n$ is the width of the spatial median. This filter eliminates small intensity fluctuations produced by errors in the energy normalization of individual lidar profiles and large-scale spatial variations produced by atmospheric attenuation. A median filter is used instead of a running average because it is much less sensitive to perturbation by extreme values, such as cloud reflections. In the ABL, aerosol inhomogeneities, which have spatial scales of the order of the boundary layer depth typically have the largest backscatter fluctuation [*Kunkel et al.*, 1980]. Since the boundary layer depth during the present experiment was approximately 1 km, a filter length of 2 km proved to be a suitable choice.

The filtered lidar profiles making up a volume scan provide a spherical coordinate (range, elevation, azimuth) representation of aerosol inhomogeneities. In the second step of the data analysis the representation is changed to cylindrical coordinates (altitude, range, azimuth). In this new constant altitude plan position indicator (CAPPI) format, individual profiles appear to have been acquired by a lidar located at an altitude, z, and scanning horizontally through the same azimuth angles sampled in the original data. These new profiles are formed by linear interpolation between the nearest two lidar profiles recorded at the same azimuth angle. Figures 1 and 2 show the geometry of this conversion.

Wind velocities are obtained from the CAPPI scans using an algorithm that includes the steps described below.

2.1. *Correction for Wind Distortion*

During the 3 to 4 min required to complete a volume scan, the aerosol structures move along with the wind. The spatial structure is therefore distorted in the resulting lidar images. This effect is illustrated in Figure 2. During one scan the scanning radius, r, completes an arc, C, of length $r(\partial\phi/\partial t)T_s$, where $(\partial\phi/\partial t)$ is the azimuth angular scanning rate, ϕ is the azimuth angle, t is time, and T_s is the time needed to complete a volume scan. At the same time, an aerosol structure moves over a distance $D = V_t T_s$, measured along the scanning direction (V_t is the component of the aerosol velocity perpendicular to the scanning radius).

The shape distortion of the aerosol structures in the CAPPI scans is corrected by a method similar to that described by *Sasano et al.* [1982]. The correction for shape distortion is carried out by moving the individual aerosol backscatter profiles making up a CAPPI scan a distance

$$\mathbf{d} = \mathbf{v} \cdot \delta t, \tag{5}$$

where $\mathbf{v}$ is the average horizontal wind velocity in the scan area and δt is the time difference between the start of a CAPPI scan and the time when this azimuth is sampled. Because profiles making up the CAPPI scan have been computed from a number of profiles in an elevated scan, δt is approximated with the time difference from the start of the volume scan to the start of a range-height indicator (RHI) scan at this azimuth.

Finally, the data in each CAPPI scan were transformed from a cylindrical coordinate system to an image on a Cartesian x, y grid, in which the x axis was taken along the middle azimuth direction of a CAPPI scan. The origin of the x, y grid coincides with the VIL position. The data values on the Cartesian grid points were found through weighted linear interpolation between the grid points in the cylindrical coordinate system. The resolution of the Cartesian grid, typically approximately 45 m, was chosen to appropriately match the spatially averaged resolution of the cylindrical coordinate system.

2.2. *Temporal High Pass Median Filtering*

The lidar images may contain structures that do not move with the wind. Such structures typically represent residual effects of attenuation, small nonlinearities in the lidar system response, or atmospheric features, which are anchored to the underlying terrain. To remove these features, a temporal median image, $f^m(\mathbf{x}, t_i)$, is constructed at each level, over a time interval centered about each image

$$f^m(\mathbf{x}, t_i) = \text{median}\ \{f(\mathbf{x}, t_j)\} \tag{6}$$

$$i - 1 \le j \le i + 1,$$

where $f(\mathbf{x}, t_i)$ is the instantaneous aerosol backscattering distribution in an image at time t_i and at grid location $\mathbf{x} = (x, y)$, and $2l$ is the width of the temporal median. The median image is thereafter subtracted from each image to obtain the temporal high pass median filtered image, $f^f(\mathbf{x}, t_i)$:

$$f^f(\mathbf{x}, t_i) = f(\mathbf{x}, t_i) - f^m(\mathbf{x}, t_i). \tag{7}$$

Ideally, the median image is computed over a time period that is short compared to the rate at which the stationary background image changes, yet long enough that many wind driven aerosol structures pass over each image point. In practice, filter durations between 30 and 60 min are typically

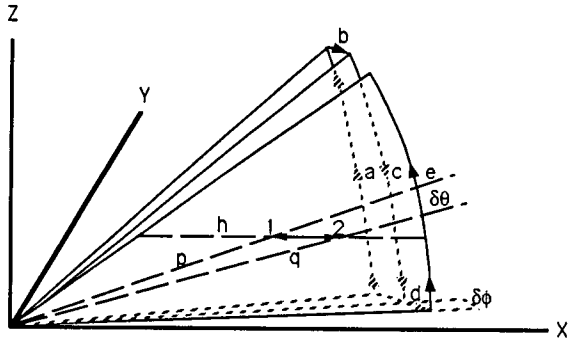

Fig. 1. Three of the 60 range-height indicator (RHI) scans, forming a complete volume scan, are shown. The scanning pattern follows the lines a-b-c-d-e. Successive RHI scans are separated by $\delta\phi$ in azimuth. Synthetic constant altitude lidar profiles are then formed at selected altitudes, for example, along the dashed line h. Aerosol backscatter values on a constant-altitude line, between 1 and 2, on a constant-altitude line, are found through linear interpolation between nearest data points in the lidar profiles p and q.

employed. This process removes the stationary features without affecting the motion of the inhomogeneities.

2.3. *Histogram Equalization*

The instantaneous aerosol backscattering distribution, $f^f(\mathbf{x}, t)$, in an image can be represented as a distribution of pixel brightness values. Here $\mathbf{x}$ is the pixel position in x, y coordinates. Anomalously bright targets may dominate and thus bias the measured average velocity to the velocity of the brightest targets. To reduce this effect, the pixel brightness distribution is made uniform by changing pixel brightness values according to the transformation

$$f_u(\mathbf{x}, t) = P[f^f(x, t)], \tag{8}$$

where $f_u(\mathbf{x}, t)$ corresponds to the new pixel brightness distribution and P stands for the cumulative probability distribution of the initial pixel brightness distribution. This transformation is illustrated in Figure 3. Pixel brightness values that lie in the tails of the distribution are compressed, whereas the pixel brightness values in the central region are expanded. This operation is referred to as histogram equalization.

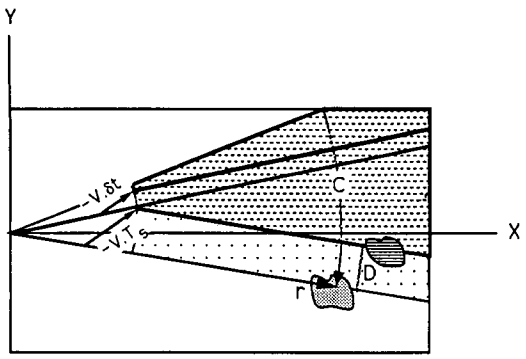

Fig. 2. A CAPPI scan is corrected for wind distortion by displacing each of its radial aerosol backscatter profiles over a distance $-V\delta t$, where δt is the time elapsed since the start of a CAPPI scan.

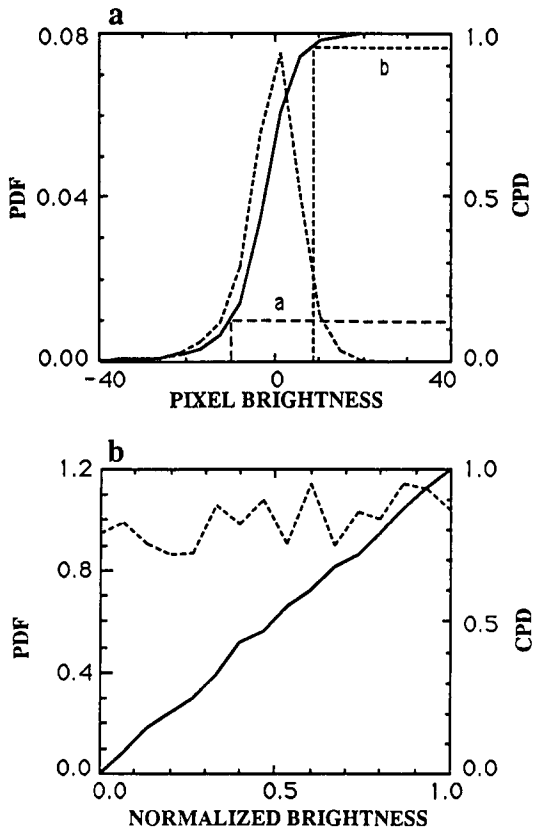

Fig. 3. (*a*) The probability density distribution (PDF), shown by the short-dashed curve, and the cumulative probability distribution (CPD), shown by the solid curve, of pixel brightness values for an image on July 1, 1987, at 1356:49 CDT at a height 400 m above the lidar site. (*b*) Same as in Figure 3*a*, except after the histogram equalization, using 256 levels of pixel brightness. The transformation for two pixel brightness values is illustrated in Figure 3*a* with the dashed curves labeled a and b.

2.4. *Spatial Cross Correlation Function*

To find an objective estimate of the aerosol motion averaged over the area of an image, the location of the maximum value of the two-dimensional spatial cross correlation function (CCF) is used. The CCF between the patterns $f_u(\mathbf{x}, t_1)$ and $f_u(\mathbf{x}, t_2)$, observed at the times t_1 and t_2, respectively, is defined as

$$C(\delta\mathbf{x}, t_1, t_2 - t_1) = \int_S f_u(\mathbf{x}, t_1) f_u(\mathbf{x} + \delta\mathbf{x}, t_2)\, dS, \tag{9}$$

where $\delta\mathbf{x} = (\delta x, \delta y)$ is a lag vector and the integral is taken over an area S.

The CCF is computed between successive images using the computationally efficient fast Fourier transform (FFT) technique [*Otnes and Enochson*, 1972]. Before the FFT is applied, each image is linearly detrended to take the spectral power out at zero wave number and to minimize leakage from low wave numbers into the higher wave numbers. The discrete FFT of an image on a regular x, y grid with dimensions L_x and L_y is written as

$$F_u(\mathbf{k}, t) = \sum_{m=1}^{M} \sum_{n=1}^{N} f_u(\mathbf{x}, t) \exp^{-(j2\pi \mathbf{k} \cdot \mathbf{x})}, \quad (10)$$

where

$\mathbf{k} = (k_x, k_y)$, the wave vector;
$k_x = (i_x M_x)/(ML_x)$, the wave number in the x direction;
i_x = lag index in the x direction ($-M/2 \le i_x \le M/2$);
M_x = number of data points in the x direction;
M = number of data points in the x direction, extended with zeroes to obtain a power of 2;
$k_y = (i_y N_y)/(NL_y)$, the wave number in the y direction;
i_y = lag index in the y direction ($-N/2 \le i_y \le N/2$);
N_y = number of data points in the y direction;
N = number of data points in the y direction, extended with zeroes to obtain a power of 2;
$j = \sqrt{-1}$;
$\mathbf{X} = (x, y)$, the coordinate of a data point on a x, y grid or $(mL_x/M_x, nL_y/N_y)$;
L_x/M_x = grid resolution in the x direction;
L_y/N_y = grid resolution in the y direction.

The basic method uses the FFTs of two successive images to compute the cross spectrum, $G(\mathbf{k}, t_1, t_2 - t_1)$, where

$$G(\mathbf{k}, t_1, t_2 - t_1) = 4 \frac{L_x}{M_x^2} \frac{L_y}{N_y^2} F_u^*(\mathbf{k}, t_1) F_u(\mathbf{k}, t_2) \quad (11)$$

and an asterisk denotes a complex conjugate. The cross spectrum is then high-pass filtered in wave number space to eliminate large spatial scale coherence, which may be caused by residuals introduced by the temporal high pass filtering process. Care must be taken here that the spatial high pass filtering process does not remove the large-scale coherent aerosol structure between successive images. For a typical ABL, where convective structures scale on the boundary layer depth, ≈1 km, a filter that removes scales larger than 2 km by 2 km is a good choice. The inverse FFT of the cross spectrum results in the cross-covariance function,

$$\mathrm{Cov}\,(\delta \mathbf{x}, t_1, t_2 - t_1) = \frac{1}{4} \frac{M_x}{M} \frac{N_y}{N} \cdot \sum_{i=1}^{M} \sum_{l=1}^{N} G(\mathbf{k}, t_1, t_2 - t_1) \exp\,(j2\pi \mathbf{k} \cdot \delta \mathbf{x}). \quad (12)$$

The covariance function is the numerator for the definition of the CCF,

$$C(\delta \mathbf{x}, t_1, t_2 - t_1) = \frac{\mathrm{Cov}\,(\delta \mathbf{x}, t_1, t_2 - t_1)}{\sqrt{\sigma_1 \sigma_2}}, \quad (13)$$

where σ_1 and σ_2 are the standard deviations of the successive images. The square of the standard deviation of an image is defined as

$$\sigma^2 = \frac{1}{(M_x N_y - 1)} \sum_{m=1}^{M_x} \sum_{n=1}^{N_y} [f_u(\mathbf{x}, t) - f_{u,\mathrm{ave}}(\mathbf{x}, t)]^2, \quad (14)$$

where

$$f_{u,ave}(\mathbf{x}, t) = \frac{1}{M_x N_y} \sum_{m=1}^{M_x} \sum_{n=1}^{N_y} f_u(\mathbf{x}, t). \quad (15)$$

To reduce statistical error, an average correlation function, $C_{\mathrm{ave}}(\delta \mathbf{x}, t_j, t_j - t_i)$, is then computed over successive images

$$C_{\mathrm{ave}}(\delta \mathbf{x}, t_j, t_j - t_i) = \frac{1}{j - i} \sum_{l=i}^{j-1} C(\delta \mathbf{x}, t_l, t_{l+1} - t_l) \quad (16)$$

where the indices i and j refer to the times between which the averaging is carried out.

2.5. *Location of the Correlation Maximum*

To estimate the wind speed, it is necessary to locate the maximum of the average correlation function, $C_{\mathrm{ave}}(\delta \mathbf{x}, t_j, t_j - t_i)$. Interpolation is required because this function is only available at discrete points, $\delta \mathbf{x} = (mL_x/M_x, nL_y/N_y)$. In addition, the correlation function is also often quite flat near its peak, so small noise fluctuations can move the apparent peak to one of several points adjacent to the maximum. An approximate location for the maximum, $\delta \mathbf{x}_{\max}$, is first obtained by searching for the peak in the two-dimensional array $C_{\mathrm{ave}}(\delta \mathbf{x}, t_j, t_j - t_i)$, which is smoothed by using a moving area average over 3 by 3 points. A bicubic natural nonsmoothing spline interpolation is applied to the unsmoothed average correlation function around the array location $\delta \mathbf{x}_{\max}$. The position of the maximum of the spline function determines the horizontal displacement of the aerosol inhomogeneities. Dividing this displacement by the time separation between two successive images gives the wind velocity. A bicubic natural nonsmoothing spline function is used for the interpolation around $\delta \mathbf{x}_{\max}$, since that function is smooth and preserves the shape of $C_{\mathrm{ave}}(\delta \mathbf{x}, t_j, t_j - t_i)$. Use of the bicubic natural nonsmoothing spline interpolation improves the accuracy of the determination of the position of the maximum of the average correlation function to within a fraction of the grid resolution.

A first estimate of the horizontal wind velocity is obtained using this algorithm without the correction step for wind distortion. The first estimate of the wind velocity is then used to repeat the algorithm in its full extent to get a better value of the wind velocity. The algorithm converges rapidly, requiring only one or two iterations.

3. RESULTS

3.1. *Site and Instrumentation*

Measurements were obtained between June 25 and July 15, 1987, on the Konza Prairie long-term ecological research (LTER) site near Manhattan, Kansas, as part of the First International Satellite Land Surface Climatology Project (ISLSCP) Field Experiment (FIFE). *Sellers et al.* [1988] give a brief description of the experiment. The primary 15-km by 15-km field site is a mostly treeless, rolling prairie with altitude variations of roughly 100 m. The UW VIL system was located near to the center of the site (96°32'30"W,

Fig. 4*a*. Perspective three-dimensional view of convective cells in the atmospheric boundary layer (ABL) displayed over a high-resolution SPOT picture of surface topography on July 1, 1987, at 1121 CDT under almost windless convective conditions. This display is prepared by selecting a contour layer to construct a solid surface through the volume of normalized aerosol backscatter data. The lidar is located at the origin of the coordinate system provided in the picture. All dimensions are given in kilometers. A fork-shaped creek bed area is clearly visible on the surface, with one leg at 8 km and the other one between 5 and 8 km.

TABLE 1. University of Wisconsin Lidar System Parameters (1987)

Instrument	Parameter Specification
Laser transmitter	
wavelength	1064 nm
beam pointing resolution	0.2 mrad
average output energy per shot	0.6 J
pulse repetition rate	30 Hz
pulse duration	≈7 ns
Receiver telescope	
diameter	0.5 m
field of view	adjustable, 1.5–7 mrad
detector	Silcon Avalanche Photodiode **(RCA 30955E)
quantum efficiency	40% at 1064 nm
spectral band pass	1.0 nm, interference filter
Data logging	
logarithmic amplifier	100-μV to 6-V input range (=90dB)
A/D resolution	10-bit resolution
sampling rate	20 MHz max, 10 MHz this study
range resolution	7.5 m, 15 m this study
maximum range	15 km, this study
preprocessing	VAX 11/750, LSI 11/73, and CSPI array processor
output	2.6 GByte write once optical disk, real-time display

A/D is analog to digital.

39°03′51″N) at 448 m above mean sea level (msl). The average elevation of the FIFE site is approximately 408 msl. A summary of the UW three-dimensional VIL system parameters is presented in Table 1. A Doppler lidar system, operated by NOAA, was located next to the UW VIL. Sixteen portable automated mesonet II (PAM II) stations operated by NCAR were located within 10 km of the UW VIL. Members of Cornell University also operated a radiosonde system. The balloon launch location was at 96°33′47″W, 39°07′02″N, at 340 msl, approximately 6 km north-northwest of the lidars.

3.2. *Description of the Data Acquisition*

The VIL provided a time sequence of three-dimensional maps of aerosol backscattering. Typical lidar volume scans consisted of 60 RHI scans between the horizon and 10° of elevation, with about 60 lidar profiles, each consisting of 1024 range gates, in each RHI. Individual RHI scans were spaced 0.5° apart in azimuth to cover a 30° azimuthal sector. This resulted in a time separation of 165 s, between two successive images, which was short compared to the lifetime of the coherent aerosol structures. It was necessary to compromise between the angular width of the volume scans and the frequency of observation of the scans, as constrained by the laser repetition rate. The angular size and timing of the images limits the maximum wind speed that can

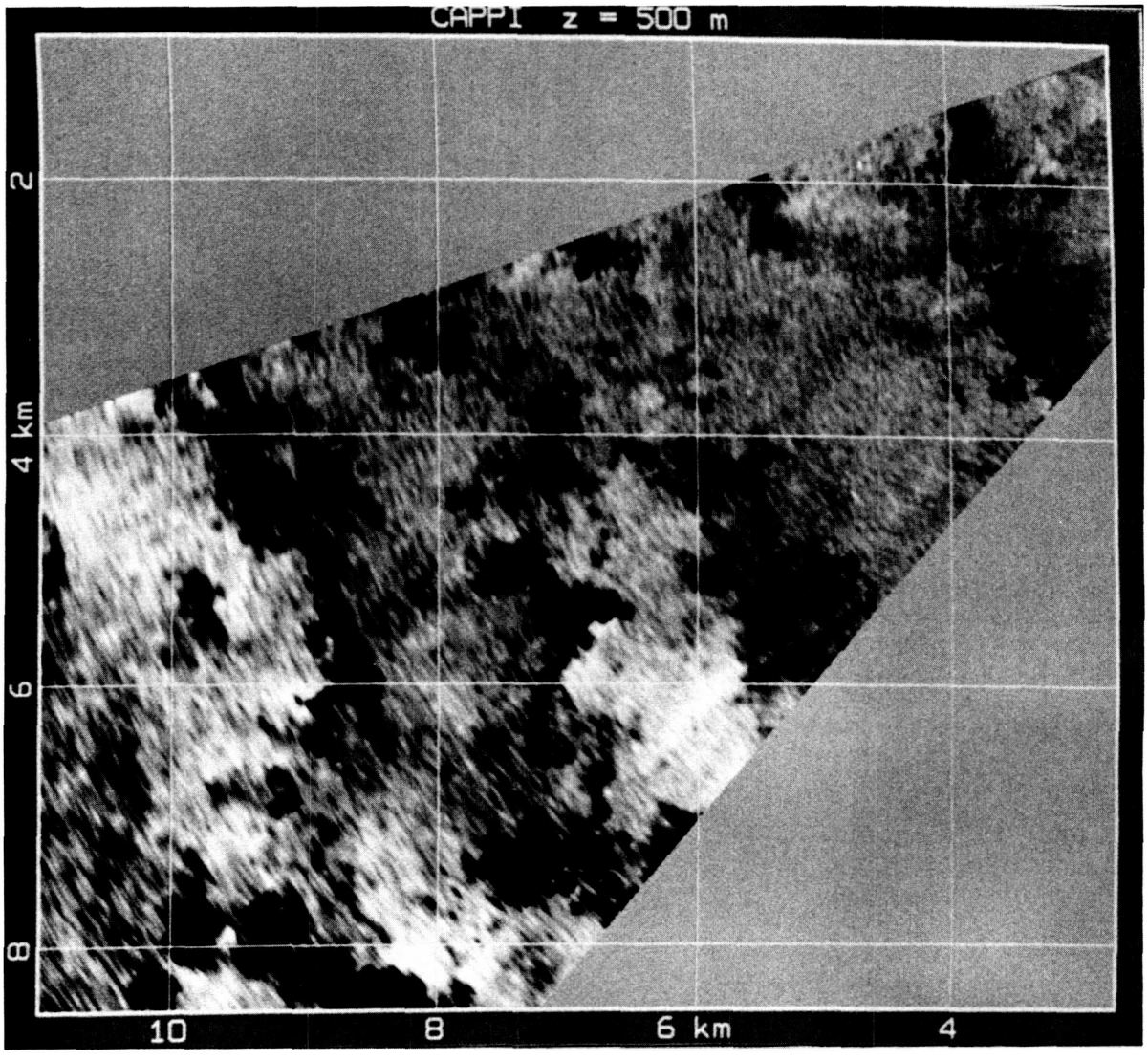

Fig. 4*b*. CAPPI scan constructed 500 m above the lidar site using the data on July 1. The bright areas correspond to aerosol-laden structures that originate from the surface, whereas the dark regions indicate clear air between these structures.

be measured. If the scan time is too long or the angular sector is too small, the aerosol structure observed on one scan may have advected out of the scan area by the start of the next scan.

Two data sets, acquired under very different conditions, were chosen to test the wind-measuring algorithm. The first set was collected between 1321 and 1424 CDT on July 1 (CDT is UT − 5 hours) in a convectively driven boundary layer. The second data set was acquired between 0627 and 0657 CDT on July 7 in a largely shear driven boundary layer. Representative volume and CAPPI scans are shown in Figures 4 and 5. Both data sets show bands of organized aerosol structures. On July 1 these bands were mainly aligned with the wind. The weather was clear, with scattered convective clouds. Surface winds measured by PAM stations were less than 2 m s^{-1}. The depth of the ABL changed from approximately 1100 m above the lidar site at the start of the data set to around 1300 m at the end. Scattered convective clouds appeared on top of the convective plumes. On July 7 the aerosol bands were orientated nearly perpendicular to the wind direction. The sky above the site was clear, and the surface sensible heat flux was small. A thunderstorm was approaching, and the winds were 3 to 10 m s^{-1}. This data set provided an example of shear-driven turbulence, in contrast to the convective conditions of July 1. Boundary layer depth grew from 300 m at the beginning of the period to 500 m at the end. The contrast between the aerosol structures and their background, that is, the image contrast, decreased significantly during this period.

3.3. *Computational Results and Accuracy*

Figures 6*a*–6*d* illustrate the effect of various processing steps applied to the CAPPI scans obtained on July 1. The convective, low wind speed conditions provided a particularly good test case for the performance of the temporal high

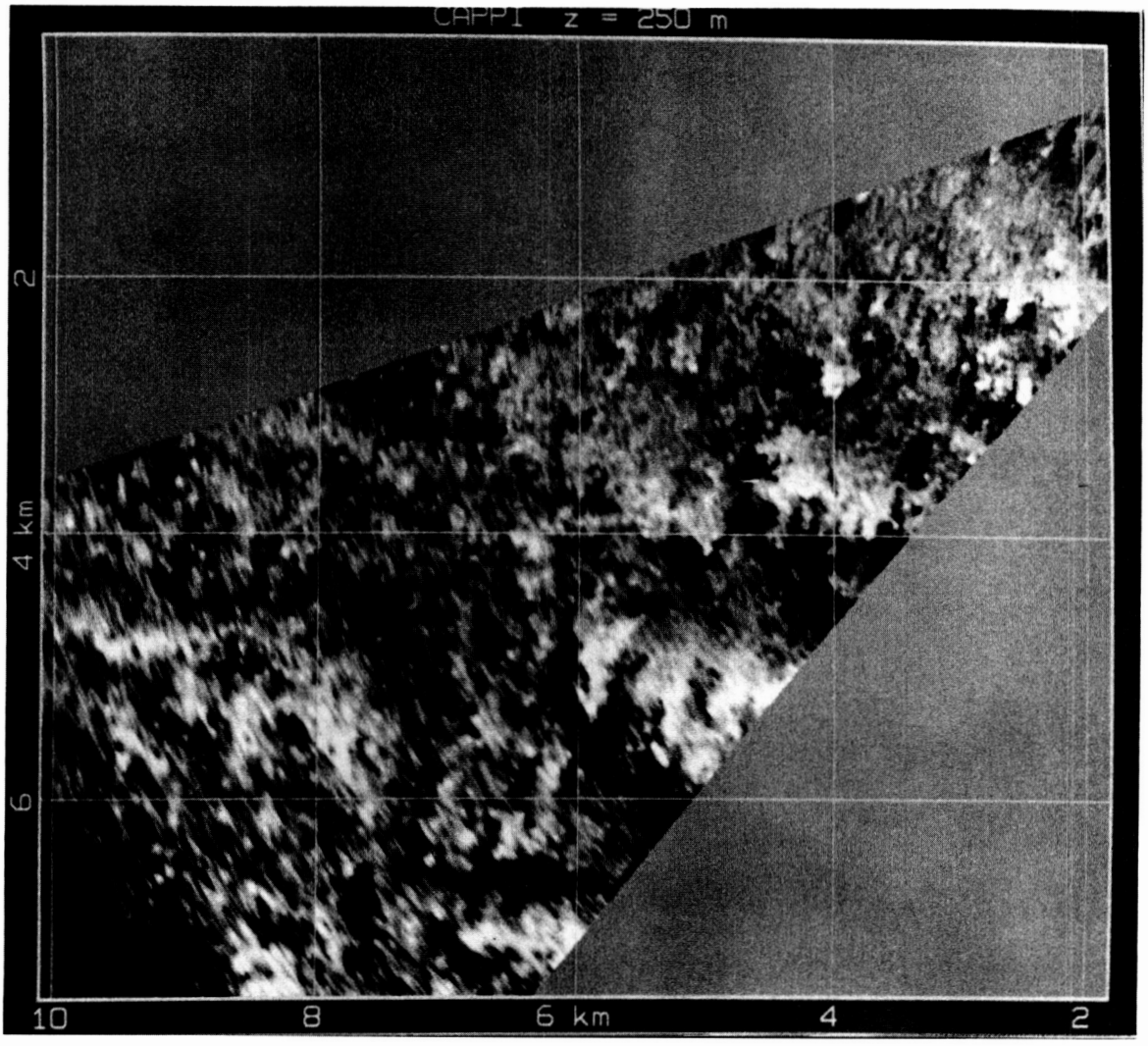

Fig. 5. Same as in Figures 4*a* and 4*b*, except for a shear-driven ABL with low surface heat flux on July 7, 1987, at 0636 CDT. The CAPPI scan is made at 250 m above the lidar site.

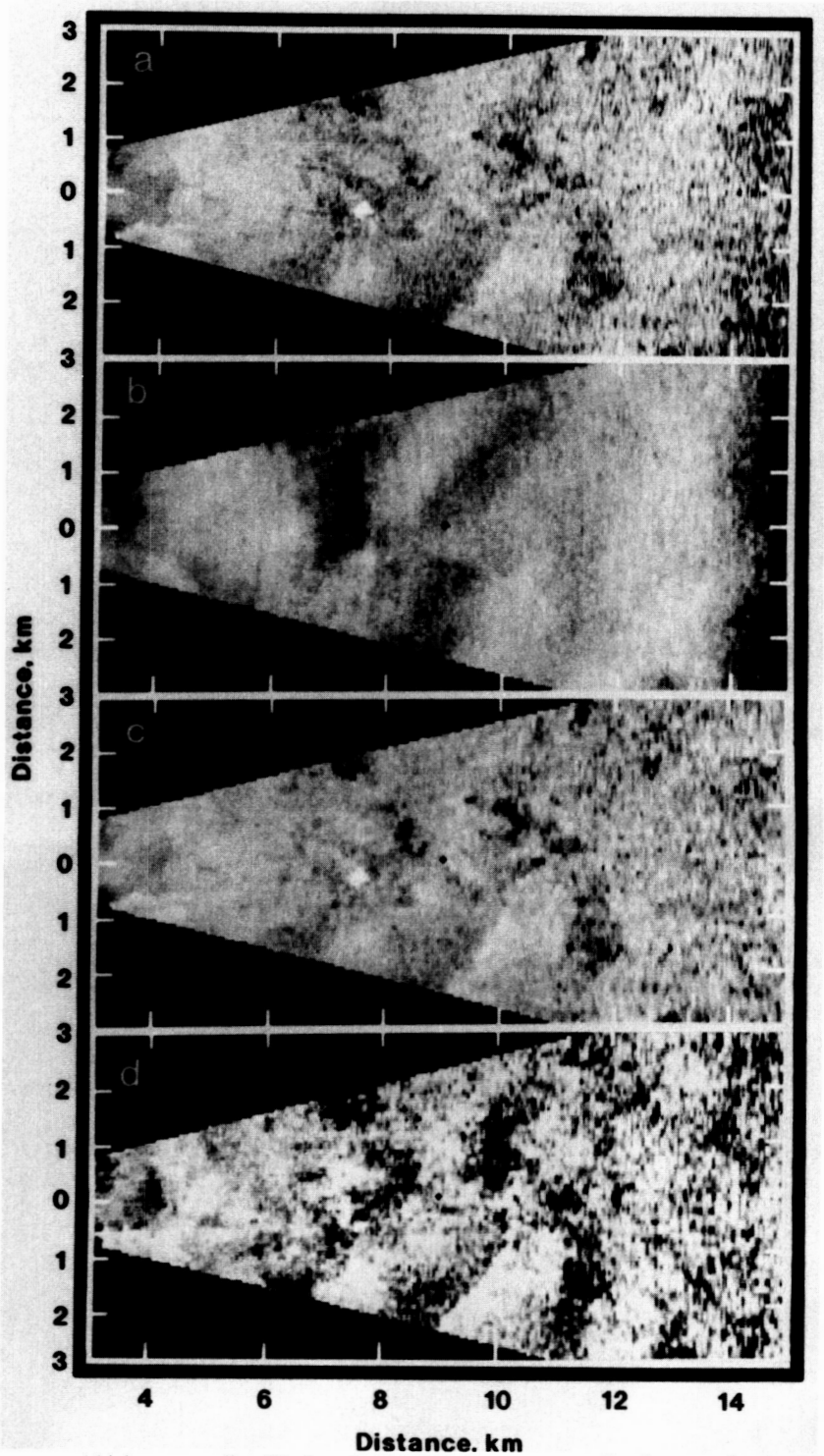

Fig. 6. The temporal high pass median filtering step and the histogram equalization step for the July 1 data set at 1321:09 CDT at 100 m above the lidar. (*a*) CAPPI scan. (*b*) The temporal median, taken over 24 images (66 min), displays the motionless background. The fork-shaped dark area around 8 km reflects the creek beds on the surface. (*c*) The temporal high pass median filtering removes the motionless background. (*d*) The image after histogram equalization.

pass median filtering step. The median image shows a clear picture of the background in which the aerosol structures are embedded. The histogram equalization step, which was applied to make the brightness distribution in the image uniform, enhances the visual contrast in the gray regions.

Figure 7 displays a comparison of VIL-determined winds with conventional measurements. On July 7 all profiles (top panels of Figure 7) show similar vertical shear. The UW VIL profile at 0627:18 CDT and the Doppler lidar profile at 0611 CDT agree very well, except below 300 m height. The UW

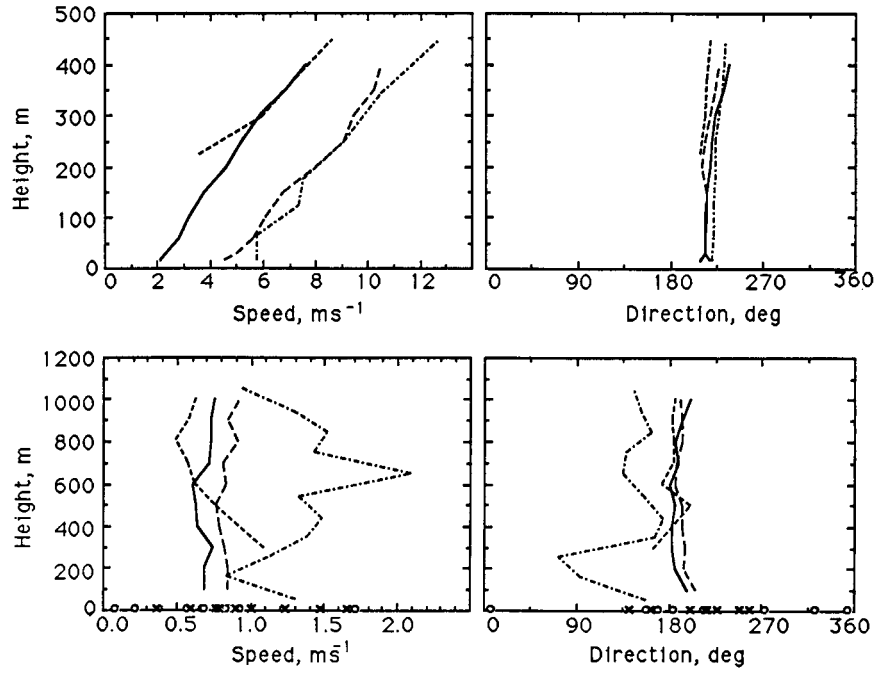

Fig. 7. A comparison of wind profiles measured by the UW VIL, the NOAA Doppler lidar, and the radiosonde. (Top panels) Wind profiles on July 7, 1987, where the solid curve shows the UW VIL wind profile at 0627 CDT; the short-dashed curve shows the Doppler lidar wind profile at 0611 CDT; the long-dashed curve shows UW VIL wind profile at 0654 CDT; and the dotted-dashed curve shows the radiosonde wind profile at 0704 CDT. The UW VIL wind profile is calculated at altitudes of 15, 30, 60, 100 m and then at 50-m intervals above 100 m. The radiosonde profile is averaged over 100-m layers. (Bottom panels) Wind profiles for July 1, 1987, where solid curve shows the 660-s average UW VIL wind profile at 1326 CDT; the short-dashed curve shows the Doppler lidar wind profile at 1327 CDT; the long-dashed curve shows the 660 s average UW VIL wind profile at 1337 CDT; and the dotted-dashed curve shows the radiosonde wind profile at 1339 CDT. The UW VIL wind measurements were calculated at 100-m vertical intervals. Thirty-minute averaged 10-m altitude winds measured by portable automated mesonet (PAM) stations are also shown. Two separate 30-min averages are shown for each PAM station; the first average (circles) begins at 1300 CDT. The second average period (crosses) begins at 1330 CDT.

VIL profile at 0654:44 CDT and the vertically averaged radiosonde profile at 0704 CDT, match closely. The UW VIL profile looks smoother, as a result of the averaging over a 32-km^2 horizontal area. In the early afternoon of July 1 (bottom panels of Figure 7) the conditions were convective, with almost no average wind. These conditions, together with the organized roll convection (see Figure 4), caused large updrafts and downdrafts in the ABL. As a result, bright and dark bands appeared in the images. To obtain a stable estimate of the horizontal wind velocity, it is therefore necessary to average over an area of 12 km by 6 km. This allowed averaging over many convective cells to obtain a consistent estimate of the mean wind velocity. The fluctuations in a UW lidar profile between adjacent points are of the order of 0.1 m s^{-1} in speed and 10° in direction. As expected, under almost windless conditions with strong clear air convection, little vertical shear is evident. The Doppler lidar showed a wind speed that decreases with altitude. The difference between the UW VIL derived winds and the Doppler lidar determined winds are most likely caused by sampling effects, caused by the much smaller averaging volume represented by the Doppler velocity azimuth display (VAD) scan. The Doppler VAD wind measurement technique provided wind measurements during a 2-min sweep for a volume consisting of a vertically oriented cone. The VIL was located at the vertex of the cone. Wind measurements at each altitude sample a ring around the lidar with a diameter that increases with altitude. The wind profile measured by the radiosonde balloon represents a point measurement of the wind velocity at each level. The wind profile measured by the radiosonde drift shows large variations that are caused by the turbulent motions on the balloon path. In this convective light wind case, the turbulent velocities scale with the convective scaling velocity w_*, which was approximately 1.5 m s^{-1}. The 30-min average 10-m winds measured by PAM stations are also shown. Two successive averages are shown for each PAM station. Large differences exist between stations and between successive measurements. The scatter in the points on each profile, the differences between the profiles, and the variations in the PAM measurements are equal to or less than w_*.

Each of the individual steps of the wind measurement algorithm was found necessary to obtain smooth and accurate profiles. Figure 8 shows 165-s average wind profiles, averaged over an 8-km by 4-km area. They were acquired during the morning of July 7, between 0627:18 and 0630:03 CDT, when the image contrast was the highest (top panels of Figure 8), and at the end of this data set, between 0654:44 and 0657:29 CDT, when the image contrast was the lowest (bottom panels of Figure 8). The calculations were done using all steps and deleting one step each of the algorithm. The data set contained 12 images, and the time separation

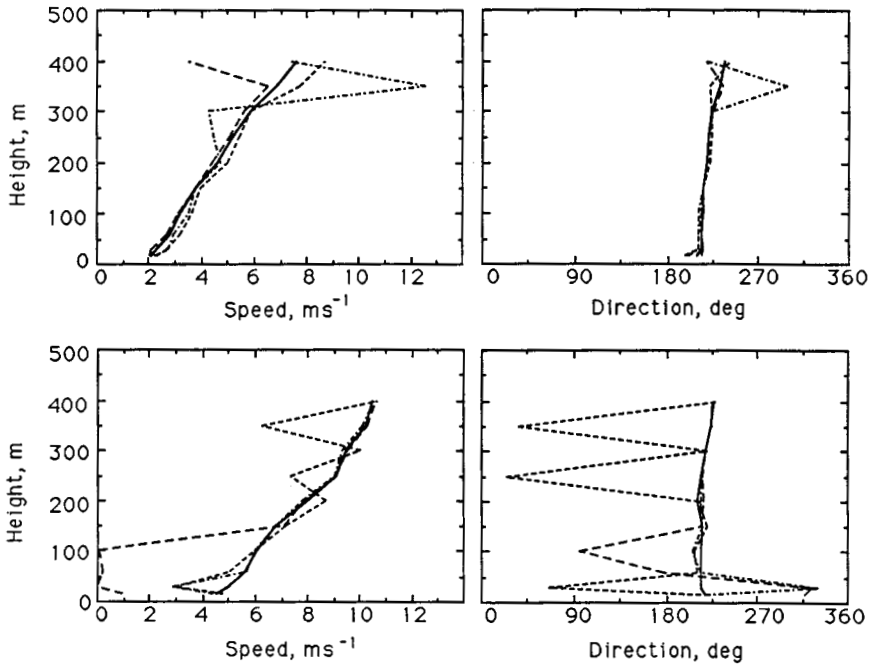

Fig. 8. (Top) July 7, 1987, 165-s average wind profiles at 0627 CDT and (bottom) at 0654 CDT measured using all the steps in the algorithm (solid curve). The short-dashed curves contain no correction for wind distortion. The long-dashed curves have no temporal high pass median filtering; and the dotted-dashed curves have no histogram equalization.

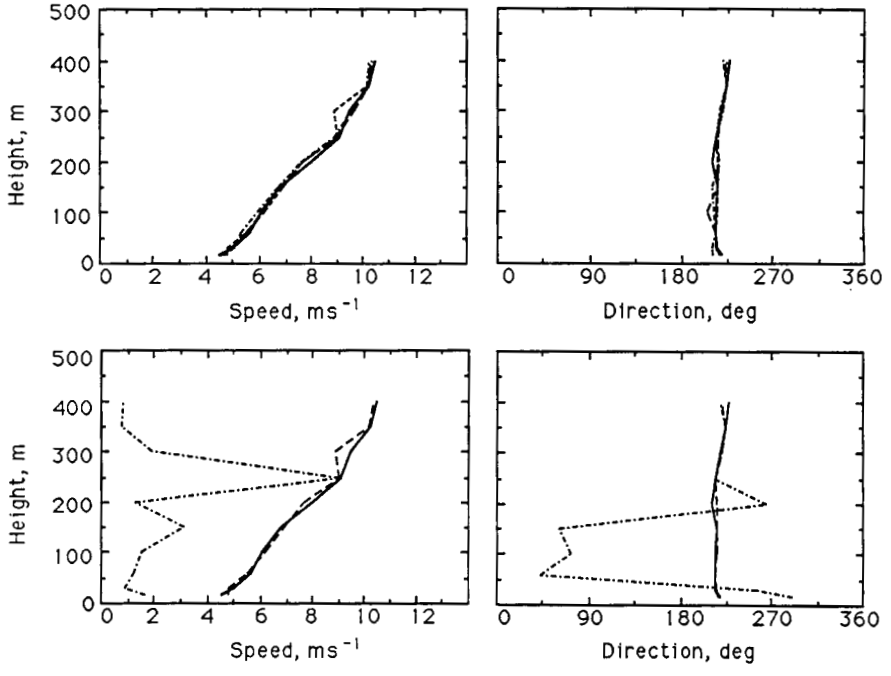

Fig. 9. University of Wisconsin VIL wind profiles obtained on July 7 at 0654 CDT: (Top panels) the solid curve shows median length of 330 s and a temporal average of 165 s; the dotted curve shows a median length of 990 s and a temporal average of 165 s; the dashed curve shows a median length of 330 s and a temporal average of 330 s; and the dotted-dashed curve shows a median length of 990 s and a temporal average of 330 s. (Bottom panels) The 165-s averages calculated with and without spatial high pass filtering (see section 2.4) that eliminates scales larger than 2.5 km in both horizontal dimensions, where the solid curve shows the median length of 330 s with filtering and the dashed curve median length of 990 s with filtering; and the dotted-dashed curve shows the median length of 990 s and no spatial high pass filtering.

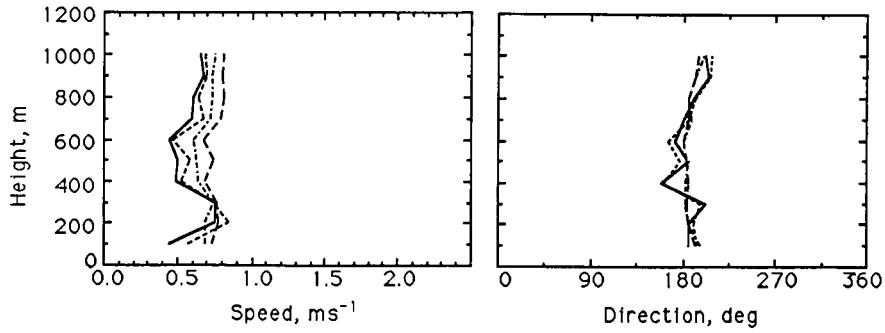

Fig. 10. Profiles measured in the afternoon of July 1, 1987, at 1326 CDT using two different lengths, namely, 2640 and 3795 s, of the temporal high pass median filter and temporal averaging over 165 and 660 s. The short-dashed curve shows a median length of 2640 s and a temporal average of 165 s; the solid curve shows the median length of 3795 s and temporal average of 165 s; the long-dashed curve shows the median length of 2640 s and temporal average of 660 s; and the dotted-dashed curve shows the median length of 3795 s and temporal average of 660 s.

between two successive images was 165 s. The correction for wind distortion has a larger effect in the upper part of the boundary layer, where the wind speed is higher. Wind direction is almost uniform throughout the boundary layer depth. Deleting the step at 0627:18 CDT leads to an overestimation of the horizontal wind speed throughout the boundary layer, because the direction of the wind component transverse to the scanning radius coincides with the clockwise scanning direction. At 0654:44 CDT, when there is little contrast between the aerosol structures and their background, omission of the correction for wind distortion does not always lead to an overestimation of the horizontal wind speed. In spite of the histogram equalization step, a few local bright spots in a low contrast image may still dominate the CCF computations. The area-averaged wind velocity is then biased toward the apparent motion of these individual spots. Because the median background in which the aerosol structures were embedded was changing rapidly, the length of the temporal high pass median filter was selected to be 330 s, twice the time separation between two successive images. The temporal high pass median filter most strongly affects the regions near the surface and at the top of the boundary layer. This is because topographic features are most prominent near the surface, while nonlinearities in the lidar system response or residual effects of attenuation are more likely near the top. When this step is not used, the wind speeds are biased to low values by stationary features.

The computations showed little sensitivity to the length of the temporal high-pass median filter. Figure 9 shows the results, for the early July 7 data, after the image contrast had decreased substantially at the end of this data set. Different choices of the length of the temporal high pass median filter, namely, two and six time separations between two successive images, resulted in differences smaller than 0.3 m s^{-1} in wind speed and 10° in wind direction for a 165-s average profile (see top panels of Figure 9). These differences were reduced when more CCFs were averaged together. For a 330-s average the differences between the profiles calculated for different temporal median lengths become smaller than 0.1 m s^{-1} in speed and less than 10° in direction. However, when the spatial high pass filtering of the cross spectrum (see section 2.4), which eliminates scales larger than 2.5 km, is omitted, the profile for a median length of six time separations exhibits large errors (bottom panels of Figure 9). The high-pass spatial filter apparently reduces sensitivity to the length of the temporal median. Figure 10 shows the results of a calculation for different lengths of the temporal median, namely, 2640 and 3795 s, on July 1. For 660-s averages the difference between the profiles is smaller than 0.1 m s^{-1} in speed and 10° in direction. In addition, the profiles for the longer 24-image median look smoother, which indicates that this is a better choice for the median length for this convective, low wind speed case.

In Figure 11, CCFs are presented for both July 1 and July 7 data sets. The CCFs are shown as three-dimensional surfaces to enhance their visualization. The height of the peak with respect to the background is clearly depicted.

4. Discussion and Conclusions

Horizontal wind speeds and directions within the ABL were estimated by measuring the drift of aerosol backscattering patterns inside successive lidar images, using a two-dimensional spatial cross correlation technique.

The wind-measurement algorithm, described in section 2, has been validated during FIFE, under two very different conditions, namely, a convective light wind case and a shear-driven case with moderate to high wind speeds. The derived wind profiles were shown to be nearly insensitive to the choice of the length of the temporal high pass median filter, provided an additional spatial high pass filtering is used. The area averaging allowed accurate mean horizontal wind measurements in the presence of turbulence, which degrades conventional observations.

A comparison of the lidar wind measurements with winds measured by Doppler lidar and balloon-borne radiosondes displayed differences of the order expected from the variations produced by the different spatial and temporal averaging inherent in each technique. For example, on July 1, internal consistency between winds independently calculated for adjacent altitudes or times suggest that spatial averaging reduced sampling errors well below the level of turbulent fluctuations. The variation between adjacent levels, of 5- to 10-min average lidar wind measurements, is smaller than 0.1 m s^{-1} in speed and 10° in direction.

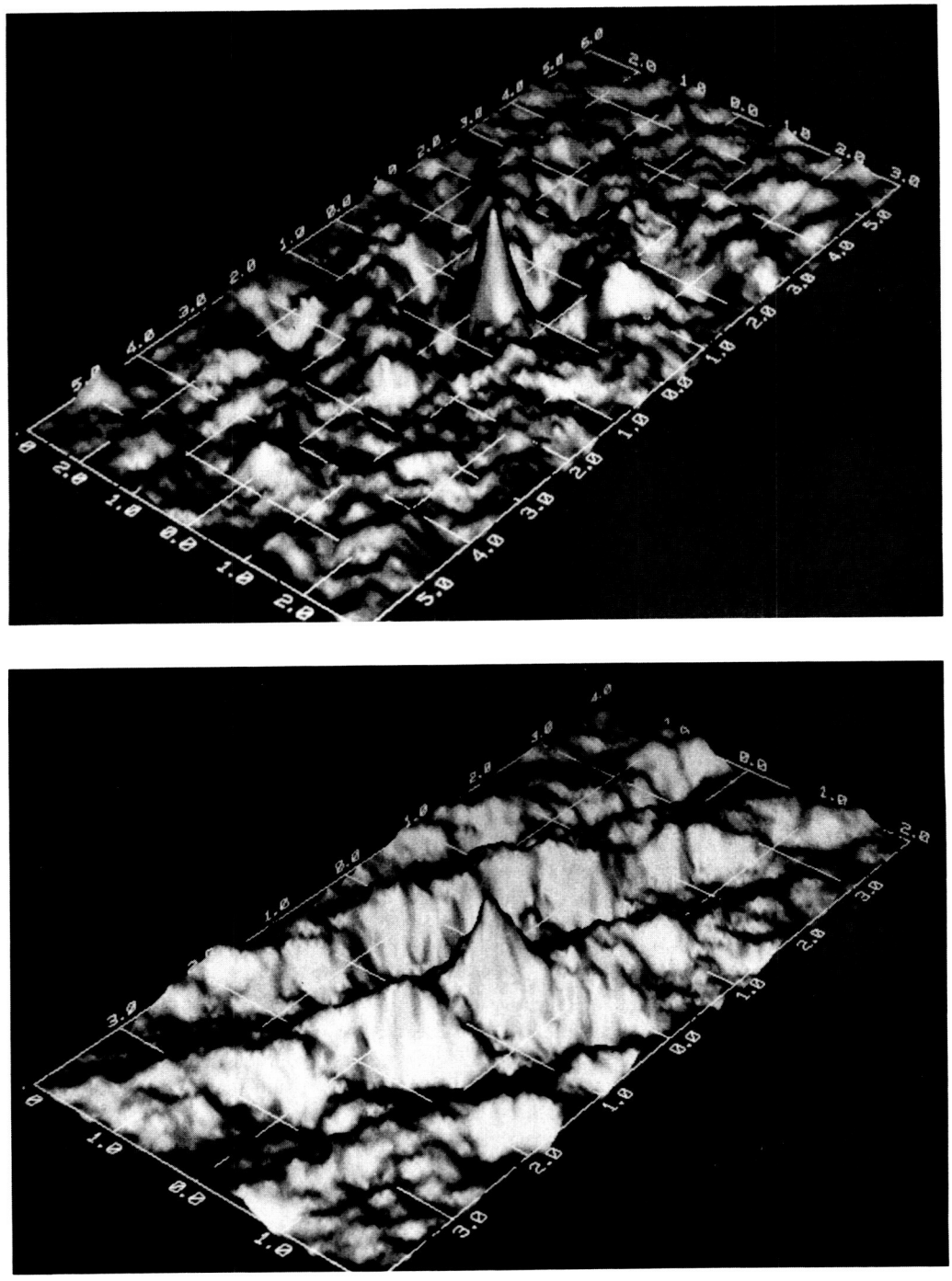

Fig. 11. Cross-correlation functions (CCFs) displayed as three-dimensional surfaces for the July 1 and July 7 data sets. The axes are annotated in kilometers. (Top) July 1, 1321:09 to 1323:54 CDT at 100 m height above the lidar site. (Bottom) July 7, 0627:18 to 0630:03 CDT at 30 m height above the lidar site.

Acknowledgments. The authors thank Dan Forrest for designing software for the data-acquisition system, data processing, and for image display. We also appreciate the helpful discussions with our colleagues. The data on balloon soundings of the ABL were collected and analyzed by W. Brutsaert and his colleagues of Cornell University. The Doppler lidar observations were acquired by W. Eberhard and colleagues of NOAA Environmental Research Laboratories Wave Propagation Laboratory. Their cooperation is greatly acknowledged. This work was supported by ARO grant DAA-G29-80-K-0079, NASA grant NAG 5-902, and DAAL03-86-K-0024.

REFERENCES

Collis, R. T. H., and P. B. Russell, Lidar measurement of particles and gases by elastic backscattering and differential absorption, in *Topics in Applied Physics: Laser Monitoring of the Atmosphere*, edited by E. D. Hinkley, vol *14*, pp. 71–151, Springer, New York, 1976.

Eloranta, E. W., Lidar observations of the atmospheric boundary layer, in *Proceedings of the Sixth Symposium on Meteorological Observations and Instrumentation*, American Meteorological Society, Boston, Mass., 1987.

Eloranta, E. W., A lidar system designed for three-dimensional time resolved mapping of atmospheric structure, paper presented at the 14th International Laser Radar Conference, pp. 150–152, San Candido, Italy, 1988.

Eloranta, E. W., J. King, and J. M. Weinman, The determination of wind speeds in the boundary layer by monostatic lidar, *J. Appl. Meteorol.*, *14*, 1485–1489, 1975.

Ferrare, R. A., J. L. Schols, E. W. Eloranta, and R. Coulter, Lidar observations of banded convection during BLX83, *J. Appl. Meteorol.*, *30*, 312–326, 1991.

Hooper, W. P., and E. W. Eloranta, Lidar measurements of wind in the planetary boundary layer: The method, accuracy and results from joint measurements with radisonde and kytoon, *J. Appl. Meteorol.*, *21*, 990–1001, 1986.

Kaimal, J. C., J. C. Wyngaard, D. A. Haugen, O. R. Cote, Y. Izumi, S. J. Caughey, and C. J. Readings, Turbulence structure in the convective boundary layer, *J. Atmos. Sci.*, *33*, 2152–2169, 1976.

Kolev, I., O. Parvanov, and B. Kaprielov, Lidar determination of winds by aerosol inhomogeneities: Motion velocity in the planetary boundary layer, *Appl. Opt.*, *27*, 2524–2531, 1988.

Kunkel, K. E., E. W. Eloranta, and J. M. Weinman, Remote determination of winds, turbulence spectra, and energy dissipation rates in the boundary layer from lidar measurements, *J. Atmos. Sci.*, *37*, 978–985, 1980.

Leese, J. A., and E. S. Epstein, Application of two-dimensional spectral analysis to the quantification of satellite cloud photographs, *J. Appl. Meteorol.*, *2*, 629–644, 1963.

Otnes, R. K., and L. Enochson, *Digital Time Series Analysis*, 467 pp., John Wiley, New York, 1972.

Sasano, Y., H. Hirohara, T. Yamasaki, H. Shimizu, N. Takeuchi, and T. Kawamura, Horizontal wind vector determination from the displacement of aerosol distribution patterns observed by a scanning lidar, *J. Appl. Meteorol.*, *21*, 1516–1523, 1982.

Sellers, P. J., F. G. Hall, G. Asrar, D. E. Strebel, and R. E. Murphy, The First ISLSCP Field Experiment (FIFE), *Bull. Am. Meteorol. Soc.*, *69*, 22–27, 1988.

Sroga, J. T., E. W. Eloranta, and T. Barber, Lidar measurement of wind velocity profiles in the boundary layer, *J. Appl. Meteorol.*, *19*, 598–605, 1980.

E. W. Eloranta, Department of Meteorology, University of Wisconsin, Madison, WI 53706.

J. L. Schols, General Sciences Corporation, 6100 Chevy Chase Drive, Laurel, MD 20707.

(Received April 1, 1991;
revised April 27, 1992;
accepted April 29, 1992.)

JOURNAL OF GEOPHYSICAL RESEARCH, VOL. 97, NO. D17, PAGES 18,383–18,393, NOVEMBER 30, 1992

Volume-Imaging Lidar Observations of the Convective Structure Surrounding the Flight Path of a Flux-Measuring Aircraft

EDWIN W. ELORANTA AND DANIEL K. FORREST

Department of Meteorology, University of Wisconsin, Madison

The University of Wisconsin volume imaging lidar has been used to portray images of the three-dimensional structure of clear air convective plumes in the atmosphere surrounding the flight path of the instrumented Twin Otter aircraft operated by the National Aeronautical Establishment (NAE) of Canada. Lidar images provide a context for interpretation of the aircraft measurements. The position of data points within a convective element can be determined and the temporal development of the plume can be observed to time the observation with respect to the life cycle of the plume. Plots of the vertical flux of water vapor, $q'w'$, superimposed on lidar images clearly demonstrate the well-known sampling difficulties encountered when attempting to measure fluxes near the top of the convective layer. When Loran was used to determine average aircraft velocity, flight-leg-averaged horizontal winds measured by the aircraft and area-averaged winds measured by lidar agree to within 0.2 m s^{-1} in speed and 1° in direction.

BACKGROUND

Much of our knowledge of the planetary boundary layer has been acquired from aircraft-borne instrumentation. These observations have produced a rather complete description of the mean properties of the mature, midafternoon convective boundary layer over homogeneous surfaces. Mean profiles of state variables as well as flux profiles for heat, momentum, and water vapor have been measured during many experiments and have allowed the development of a system of convective layer scaling that integrates this information into a usable form [*Stull*, 1988].

While aircraft instruments are well suited for observations of established boundary layers over homogeneous terrain, difficulties arise when the layer undergoes rapid temporal changes or the surface properties change rapidly in time or space. Convective layer scaling shows that the depth of the layer is a fundamental length scale and should be measured simultaneously with flux measurements inside the boundary layer. Interpolation errors are encountered when a single aircraft sequentially measures mixed layer depth and variables inside the layer. To obtain statistically reliable estimates of boundary layer variables, aircraft measurements must be averaged over many turbulent eddies; this is particularly true outside the atmospheric surface layer, where eddies have scales determined by boundary layer depth and flight legs with lengths equal to or exceeding tens of kilometers are often required [*Lenschow and Stankov*, 1986]. It clearly becomes difficult to separate effects of spatial variability from statistical sampling variability.

Even greater difficulties are encountered when aircraft data are used in attempting to describe the typical structure of individual turbulent eddies. Although precise in situ measurements can be obtained along the flight path, it is difficult to determine the aircraft position with respect to the eddy structure. Many efforts to explain eddy structure have relied on conditional sampling techniques, where an indicator function constructed from one or more of the measured variables is used to control the sampling of other variables in a phase-coherent manner to generate a composite picture of a typical eddy [*Greenhut and Khalsa*, 1987; *Khalsa and Greenhut*, 1987]. The picture of the eddy that results depends critically on the choice of the indicator function [*Marht and Frank*, 1988]. The measurement signature depends on how and when the aircraft penetrated the eddy. The measurement path may have penetrated through the center of the eddy or just grazed the edge. In addition, the timing of the observation with respect to the growth and decay of the eddy is unknown. It is very difficult to determine whether a particular observation represents an eddy that is actively extracting energy from the large-scale shear/buoyancy field or whether it is the inertial remains of a dissipating eddy.

Remote sensors such as radar and lidar allow imaging of large volumes of the atmosphere in a short period of time, thus permitting visualization of atmospheric eddy structure [*Hardy and Otterster*, 1969; *Kunkel et al.*, 1977]. However, the images produced often lack the quantitative detail provided by in situ sensing. Measurements normally consist of one or two variables. For example, radar or lidar reflectivity may be provided; if the system has Doppler capability, radial velocities may also be included. Studies of eddy dynamics and vertical fluxes also require measurements of local velocities, along with passive and active scalars such as water vapor, temperature, and carbon dioxide. Although future remote sensors and certain current, but experimental, systems may provide some of these measurements, it is clear that in situ observations remain necessary for most investigations.

Combinations of remote and in situ measurements promise to provide considerably more information than the sum of the parts. Many examples of combined observations are available in the literature, including *Konrad and Robison* [1973], *Melfi et al.* [1985], and *Crum et al.*, [1987].

This paper describes an experiment where the University of Wisconsin volume imaging lidar is used to portray the convective structure surrounding the flight path of the Canadian National Aeronautical Establishment (NAE) Twin Otter aircraft. A unique feature of this study consists of precisely locating the aircraft measurements in the three-dimensional volume observed by the lidar. This allows point

Paper number 92JD00878.
0148-0227/92/92JD-00878$05.00

TABLE 1. University of Wisconsin Volume Imaging Lidar Specifications

Instructor	Specification	Value
Transmitter		
	laser	Nd: YAG
	average power	20 W
	repetition rate	30 Hz
	wavelength	106.4 nm
	pulse duration	6 ns
Receiver		
	diameter	0.5 m
	angular scanning rate	25° s^{-1}
	APD quantum efficiency	35%
	range resolution	7.5 m
	optical bandwidth	1 nm
	average data rate	~0.5 Gb h^{-1}

Data Processing/Storage	Function
DEC VAX 11/750	system control and data storage
DEC LSI 11	data transfer and formating
CSPI array processor	real-time data processing
Stardent GS-1000	real-time graphics
2.6-Gb write-once optical disk	data storage

by point comparisons between the aircraft measurements and the lidar-observed structure.

INSTRUMENTATION

The Volume-Imaging Lidar

The volume-imaging lidar (VIL) is an elastic backscatter lidar designed to image the four-dimensional structure of the atmosphere. This system couples an energetic, high pulse repetition rate laser with a sensitive receiver and a fast computer controlled angular scanning system. High-bandwidth data acquisition is sustained during extended experiments by using a 2.6-Gb write-once optical disk for data storage. A Stardent GS-1000 graphics computer provides 1280 × 1024 pixel resolution lidar images with 16-bit pseudocolor for real-time control of data acquisition and data analysis. System specifications and a block diagram are provided in Table 1 and Figure 1.

The high sensitivity of the VIL allows observations of inhomogeneities in natural aerosol backscatter that reveal clear air convective structure. Convective plumes carry surface aerosols aloft into cleaner air. Since many of the aerosol particles are hygroscopic, the particles also increase in size as the relative humidity increases. Adiabatic cooling of expanding air in a rising parcel increases the relative humidity and thus increases the aerosol scattering cross section. As a result the lidar easily delineates the boundary between mixed layer air and the free atmosphere above. Parcels of dryer, relatively clean air entrained into the boundary layer at the base of the inversion are also easily detected as they are mixed downward into the convective layer.

AIRCRAFT INSTRUMENTATION

The Twin Otter contains a Rosemount 8585 five-hole probe to provide three orthogonal components of atmospheric motion over a frequency range of 0 to 5 Hz. Aircraft motions were determined with three separate systems: (1) three-axis Decca Doppler radar coupled with a NAE-assembled package of accelerometers and rate gyros, (2) Litton-90 inertial reference system, and (3) an ARNAV model R-40-AVA-100 Loran-C navigation system. Temperature was measured with a Rosemount fast response 102DJ1CG heated probe mounted on the port side of the aircraft nose and by a second, identical probe mounted on the nose boom fairing. Fast-response humidity and carbon dioxide measurements used the ESRI infrared gas analyzer developed by Agriculture Canada. These measurements were made in a high flow rate (~300 L^{-1}) duct passing through the aircraft cabin. Slow-response carbon dioxide measurements were made with a LI-COR LI-6251 carbon dioxide analyzer and slow-response water vapor measurements were obtained using an EG & G model 137 Cambridge dew point sensor.

A more complete description of the aircraft instrumentation is given by *MacPherson* [1990].

DATA ACQUISITION

The data described in this paper were acquired on August 3, 1989, as part of the NASA First International Satellite Land Surface Climatology Project (ISLSCP) Field Experiment (FIFE). The lidar was operated south of Manhattan, Kansas, near the intersection of Route 177 and Interstate Highway 70 at FIFE site 123 (3639-L1W).

For the observations reported in this paper, the lidar was programed to repeatedly scan an atmospheric volume con-

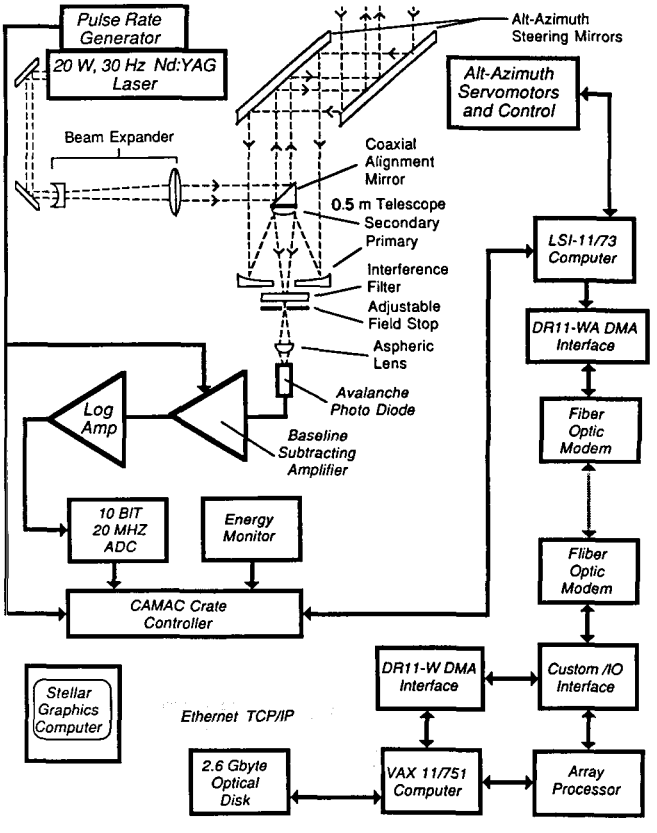

Fig. 1. Schematic diagram of the volume-imaging lidar.

sisting of the elevation angles between 0.3° and 10° and between azimuth angles of 215° and 255°. The scan pattern consisted of a sequence of 80 elevation scans separated by 0.5° in azimuth; lidar profiles were acquired at elevation angle increments of approximately 0.25°. It took 187 s to scan the volume completely. Each scan included approximately 5600 lidar profiles, each of which consisted of 1024 data points obtained at 15-m intervals.

The Twin Otter acquired data along constant pressure altitude flight legs, which began directly over the lidar and extended approximately 20 km from the lidar. Real-time lidar displays of the convective boundary layer were used to measure boundary layer depth as the aircraft approached the lidar. These measurements were used by the lidar operators to select the flight altitude of the aircraft for the data segment. The altitude was normally selected at a fixed fraction of the mixed layer depth. The flight heading was chosen along the center of the lidar scan, unless lidar imagery suggested a reason for an alternate heading. The flight altitude was converted to geometric altitude above mean sea level and the altitude and heading were radioed to the aircraft in time for the pilot to stabilize altitude, heading, and airspeed before beginning the data segment. This procedure increased the efficiency of data collection by positioning the aircraft at the proper altitude even in the presence of changes in boundary layer depth. During one observation period, convective "streeting" was observed in the lidar images. In this case, the lidar operators were able to select a flight heading perpendicular to the "streets" to clearly delineate the roll pattern in the aircraft data record.

Data Analysis and Navigation

Superposition of aircraft measurements on the lidar imagery requires careful attention to aircraft navigation and to the advection of atmospheric structure by the wind. The size of clear air convective plumes is comparable to the depth of the convective boundary layer; thus to maintain a 10% positioning error, the aircraft location must be known to an accuracy of 100 m or better in a typical afternoon boundary layer with a 1-km depth.

At the start of each flight leg the aircraft crew triggered an event flag in the data record at the instant they judged that the airplane was directly over the lidar. This event flag was used to check the accuracy of the aircraft Loran position by comparing the recorded positions with the known position of the lidar. Since the lowest flight was flown at an altitude of ~100 m and ground observations indicated that the pilot was successful in flying directly over the lidar, the event flags are believed to have been triggered when the aircraft was within 100 m of the lidar position. On the lowest-level flight the Loran showed the aircraft to be 565 m east and 796 m north of the lidar when the event marker was triggered. Because the experiment was located far from existing Loran transmitter chains, inside the "midcontinent gap," the rather large position offset is not surprising. This displacement was assumed to result from a systematic error in the Loran position; thus this displacement was therefore subtracted from all Loran positions to form a corrected position. To gain a rough check on this correction, it was compared with positions recorded at the time of the event flag on other overflights. Corrected positions at the time of the event flags for flights at altitudes of ~400 and ~800 m were 158 m east, 92 m south and 187 m north, and 37 m east, respectively.

The 400-m flight began 15 min before the low-level flight and the 800-m flight began 14 min later. The position deviations at the time of the event flags on the higher flights seem consistent with an expectation for errors ~100 m, considering the difficulty of piloting the airplane over the lidar and determining when the plane was directly above the lidar at the higher flight altitudes.

The lidar position was determined from a U.S. Geological Survey topographical map, using measured distances between the lidar van and the buildings pictured on the map. The error in this position is expected to be less than 10 m: this error does not influence the intercomparisons because the aircraft positions were determined relative to the lidar. The alignment of the lidar's azimuth with geographical coordinates was initially performed using a magnetic compass. Lidar returns from the top of a radio tower at a range of 12.9 km were later used, along with a map, to provide an exact value for the conversion from lidar azimuths to geographical directions.

Knowing the aircraft position with respect to the lidar solves only a portion of the navigation problem. The wind moves the atmospheric structure during the time it takes the aircraft to fly through the lidar-observed volume and during the time it takes the lidar to complete a volume scan. At ~45 m s^{-1} it required ~300 s for the Twin Otter to fly from the lidar van to the end of the 15-km range observed by the lidar. Similarly, the lidar required ~200 s to scan a complete volume. Since the wind speed was ~10 m s^{-1} when these data were acquired, the atmosphere moved ~3.3 km during the flight leg and ~2.2 km during the time it took for one lidar scan. At least once during each flight leg the lidar scanned directly past the aircraft; at this point and only at this point could the aircraft data and lidar image be compared directly without compensation for wind displacements. At all other points along the aircraft flight leg the air parcel sampled by the aircraft appears at some other location in the lidar image because of the wind. Both the lidar images and the apparent flight path of the aircraft were transformed to correct for wind displacements.

Lidar Image Computations

Individual lidar returns were first normalized for laser energy fluctuations between laser firings and corrected for the inverse range squared dependence contained in the lidar equation. A correction was also applied for optical attenuation, using the approximation that the attenuation cross section was independent of position in the volume. These corrections are more fully explained by *Schols and Eloranta* [this issue]. All images displayed in this paper have been corrected for the distortion produced by the mean wind during the time required for the lidar to scan the volume. In the discussion that follows, all times are measured from zero at the time the aircraft flew over the lidar.

Constant altitude plan position indicator (CAPPI) images were generated as follows:

1. A synthetic lidar profile was generated for each of the 80 range height indicator (RHI) scans making up a volume image. This profile reproduced the corrected lidar return, which would be observed by a horizontal pointing lidar fired at the azimuth of the individual RHI scan if it were located at the altitude of the CAPPI display. At each range, data points in the horizontal pointing synthetic profile were created from

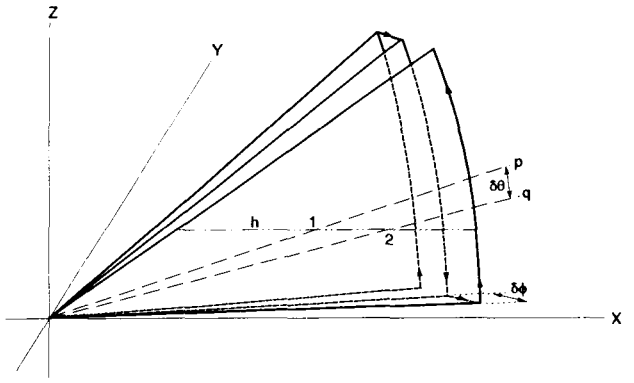

Fig. 2. Preparation of constant altitude plan position indicator (CAPPI) lidar images from volume scans. Profiles corresponding to a horizontal pointing lidar at the altitude of the CAPPI are generated from each range height indicator (RHI) scan. The data points between ranges 1 and 2 in the horizontal profile at altitude, h, are generated by linear interpolation between successive lidar profiles obtained along directions p and q. This process is repeated for all other pairs of adjacent profiles in the RHI scan to complete the horizontal profile. Horizontal profiles from all RHI scans in the volume scan are then used to compute the CAPPI image.

the corrected data points in the original RHI scan, as shown in Figure 2. The synthetic data points are computed from a linear interpolation between the data points in the nearest two lidar profiles.

2. Assuming a constant wind velocity, the individual profiles are translated to the position the air occupied at the instant when the aircraft passed over the lidar van. This process corrects for the distortion introduced by the wind in the ~200 s required to complete a volume scan. Notice that since the profiles that make up the CAPPI are synthesized from many individual profiles in the original RHI scan, this procedure assumes that the CAPPI profile was acquired instantaneously and neglects the 1- to 2-s time delay between the first and last shot in the RHI.

3. Finally, the missing pixels between the synthetic profiles are filled in by linear interpolation. This produces a complete CAPPI image depicting the atmospheric structure at the CAPPI altitude at the instant the aircraft passed over the lidar.

To superimpose the aircraft-observed data points on the wind-corrected CAPPI image, the position of each aircraft data point must be translated back to the position occupied by the air parcel at the instant when the aircraft passed over the lidar. The vector displacement for each point is the negative of the mean wind vector, multiplied by the time between the measurement and the time the aircraft passed over the lidar. With this displacement the aircraft data can be plotted directly on the CAPPI image. This procedure corrects for the geometric distortion introduced by the mean wind field; however, it does not account for temporal evolution in the structure. The comparison between aircraft observations and lidar imagery can be expected to degrade as the time separation between the lidar and the aircraft observations of a particular air parcel increases. Superposition of aircraft data on lidar RHI images is slightly more difficult. Individual RHI images are acquired rapidly (1–2 s) so that there is little wind induced distortion in an image; however, because the aircraft requires ~300 s to complete the flight leg, a composite RHI image must be formed that portrays the air parcels actually penetrated by the aircraft. In the following discussion, times are measured from the time at which the aircraft passed directly over the lidar van.

The composite RHI images were formed as follows:

1. The flight track of the aircraft over the ground was plotted and determined to be very close to a straight line.

2. A straight line was fitted to the ground path of the aircraft and the average speed of the aircraft along the path was calculated.

3. Each aircraft position on the best fit line was displaced upwind by the vector wind multiplied by the time. This new wind corrected straight line of positions indicated where the aircraft-sampled air parcels were at the time where the aircraft passed over the lidar.

4. For each RHI scan a pair of radial lines 0.25° in azimuth above and below the RHI scan were constructed. These lines were also displaced upwind a vector distance equal to the vector wind multiplied by time.

5. The points at which these lines intersected with the wind-corrected aircraft position line were then computed. These intersection points indicated the upper and lower range limit in the RHI image where this RHI azimuth provided the best match in space and time to the air parcel sampled by the aircraft.

6. Image points from the RHI scan between these range limits were then mapped onto the composite image.

7. All RHI scans from this volume scan were checked for intersecting segments and a composite image was formed.

8. The aircraft data were superimposed onto the composite RHI image, with each data point plotted on the straight-line fit to the aircraft path at the position nearest to the aircraft position at the time the data point was acquired.

Three-dimensional contour surfaces of lidar backscatter were generated as follows:

1. The position of each profile in the lidar scan was displaced upwind by a distance equal to the wind speed multiplied by the time.

2. Inside the transformed data volume a contour algorithm computed elemental polygons separating data points whose lidar backscatter exceeded a selected contour value from all other points.

3. Perspective transforms and a Gouraud shading algorithm were used to display the contour surface as a solid body image.

4. A system probatoire pour l'observation de la terre (SPOT) panchromatic satellite image of the terrain under the lidar-scanned volume was displayed in perspective to show the local topography.

5. Each point in the aircraft flight path was displaced upwind by a distance equal to the wind speed multiplied by the time. This corrected flight path was then displayed as a line penetrating the lidar image.

Data Presentation

This paper presents data measured on August 3, 1989. The sky was partly covered with fair weather cumulus clouds; cloud coverage is shown in Plate 1. At the time of the measurement the mean boundary layer depth was ~850 m, with the tops of the highest cumulus observed at ~1300 m. Cloud base altitude was ~910 m. All heights are expressed as the distances above the lidar.

Wind profiles measured with the lidar and averaged over

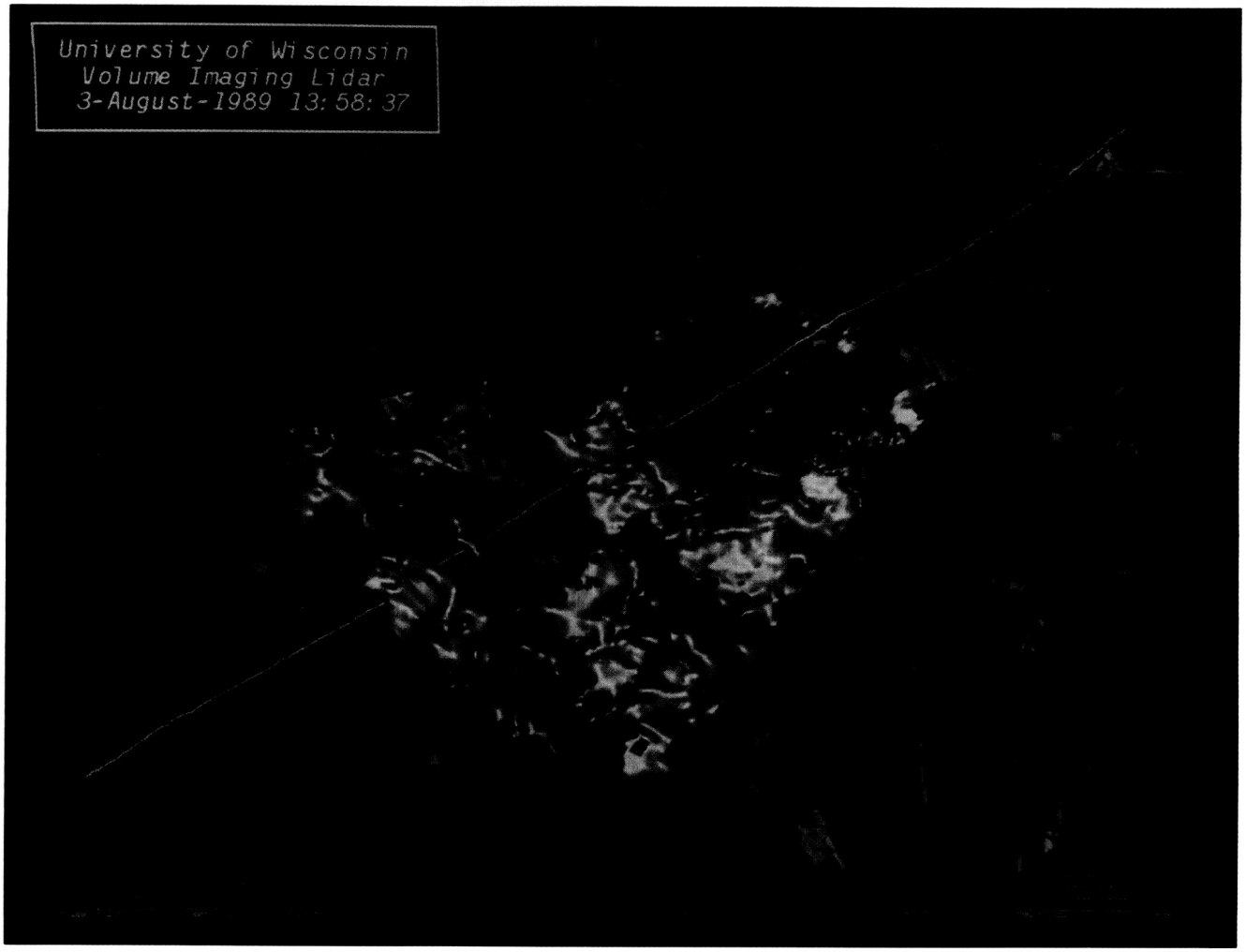

Plate 1. Three-dimensional solid contour image of clouds and the aircraft flight path derived from the lidar scan obtained between 1855:43 and 1858:36 UT. This image has been corrected to represent the position of the clouds when the aircraft passed over the lidar. Wind corrections used the lidar-measured wind of speed of 10.2 m s^{-1} and direction of 215.2°. Since the lidar penetrates only a short distance into these clouds, the image shows the cloud base and unobscured portions of the cloud facing the lidar. The terrain image was computed from a panchromatic SPOT satellite image provided by the SPOT Image Corporation. (Copyright CNES 1987.)

the ~70 km squared area of the scan were nearly independent of height between 200 m and 900 m, with a speed of ~10 m s^{-1} and a direction of ~213°. Lidar wind profiles are presented in Figures 3 and 4. This data set was chosen for analysis because the strong winds provide a stringent test of wind corrections and navigation. However, because of mechanical turbulence that mixes the aerosol structure, these rather windy conditions are not ideal for acquiring lidar images with good definition in the lower part of the boundary layer.

Figure 5 presents variables measured by the Twin Otter on a flight leg flown at an altitude of 800 m above the lidar and beginning at 1854:53 UT (1354:53 CDT) and ending at 1901:33 UT. Instantaneous fluxes are also plotted in Figure 5. Primed quantities have been computed by subtracting the mean value over the flight leg; no other detrending or filtering has been applied. Distances along the flight path were taken from the Loran position, using the Loran offset measured on the lowest-altitude flight. Aircraft ground speed calculated from the Loran position was 46.0 m s^{-1} averaged over the duration of the data record. Aircraft altitude was computed from a combination of radar altimeter and pressure altitude data. The radar altimeter has a maximum range of 779 m and thus could not be used to directly measure the altitude of this flight leg. The radio altimeter was used to measure altitudes of 436, 436, and 102 m above the lidar on three flight legs which began at 1817, 1826, and 1841 UT, respectively. The difference in pressure altitudes between these overpasses and the pressure altitude of the flight beginning at 1855 was corrected for the difference in temperature of the standard atmosphere and virtual temperature measured by the aircraft to generate true altitude. These three computations produced nearly identical results of 803, 802, and 803 m above the lidar for the 1855 leg.

Wind measurements were acquired both from aircraft instruments and from lidar observations. Lidar winds were computed by observing the drift of naturally occurring inhomogeneities in the atmospheric aerosol content using the algorithm described by *Schols and Eloranta* [this issue]. The measurements represent an average over the area of the lidar scan (~70 km^2) and the time interval between the scans (187 s). Two lidar wind profiles were measured during the

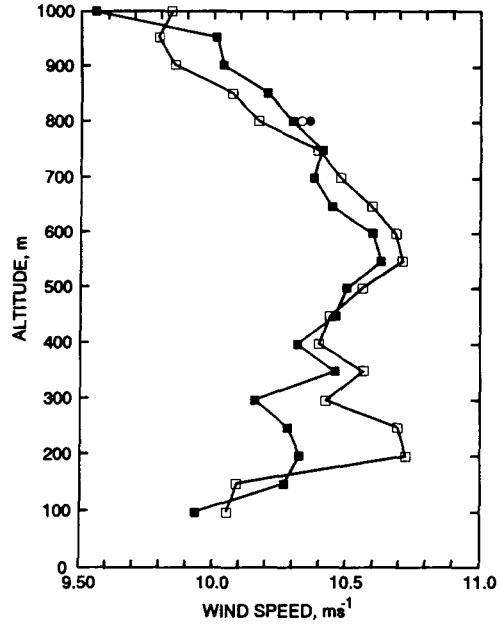

Fig. 3. Lidar-measured wind speed profiles for the periods 1855:43 to 1858:36 UT (solid squares) and 1858:50 to 1901:42 UT (open squares). Leg-averaged wind speeds computed from the aircraft data are also presented. Aircraft wind computations are shown using both the Litton-90 INS (solid circle) and the Loran (open circle) to determine aircraft motion.

aircraft flight leg (Figures 3 and 4). Aircraft winds represent the wind averaged over a 15-km data segment flown through the lidar scan. Computation of winds from the aircraft observations required knowledge of the aircraft velocity averaged over the time of the flight leg. This information was

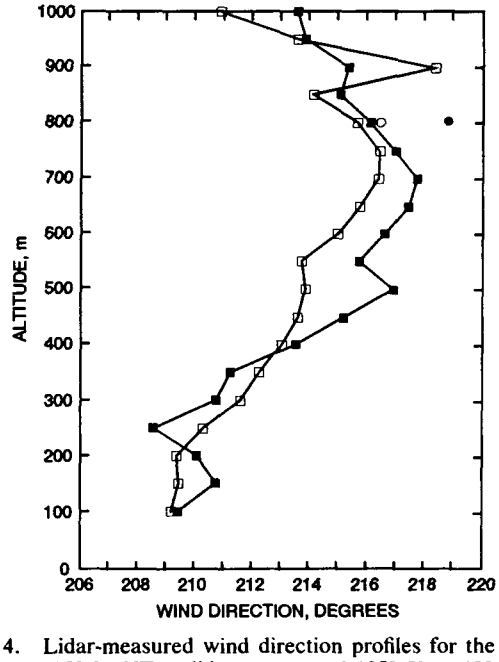

Fig. 4. Lidar-measured wind direction profiles for the periods 1855:43 to 1858:36 UT (solid squares) and 1858:50 to 1901:42 UT (open squares). Leg-averaged wind speeds computed from the aircraft data are also presented. Aircraft wind computations are shown using both the Litton-90 INS (solid circle) and the Loran (open circle) to determine aircraft motion.

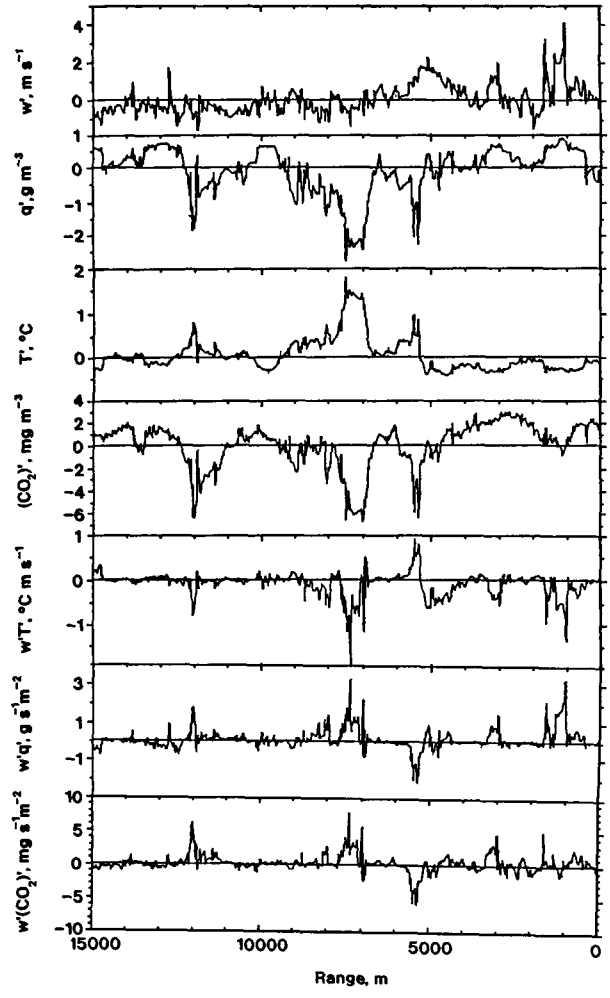

Fig. 5. Airborne measurements showing fluctuations about the flight leg mean value for vertical wind, temperature, humidity, and carbon dioxide concentration fluctuations as a function of range from the lidar. Data were acquired at a mean altitude of 803 m above the lidar in the time interval between 1854:53 and 1901:33 UT. No filtering or detrending has been applied to these records. Flux quantities are simple products of the displayed vertical velocity and scalar fluctuation quantities.

derived from the Loran positions at the ends of the data segment and the duration of the flight. A comparison of the Loran positions with the Litton inertial navigation system (INS) showed a 0.485 m s^{-1} drift of the INS at 304° with respect to the Loran positions over the duration of the data segment.

The wind measured by the lidar at an altitude of 800 m was 10.2 m s^{-1} at 216.3°; this was obtained by averaging the two lidar measurements obtained during the aircraft data run. A sequence of seven lidar wind measurements obtained between 1824 UT and 1901 UT, at an altitude of 800 m, shows speeds between 10.1 m s^{-1} and 10.9 m s^{-1}, with directions between 213° and 217°. Aircraft wind measurements show speeds of 10.32 m s^{-1} at 216.2°, using the Loran, and 10.35 m s^{-1} at 218.9°, when using the Litton-90 INS to determine aircraft velocity. A comparison of the lidar winds computed at the time of the aircraft flight leg and the aircraft winds are provided in Figures 3 and 4. Note the excellent agreement between measurements; at the airplane flight altitude the successive lidar measured speeds agree to within 0.1 m s^{-1}

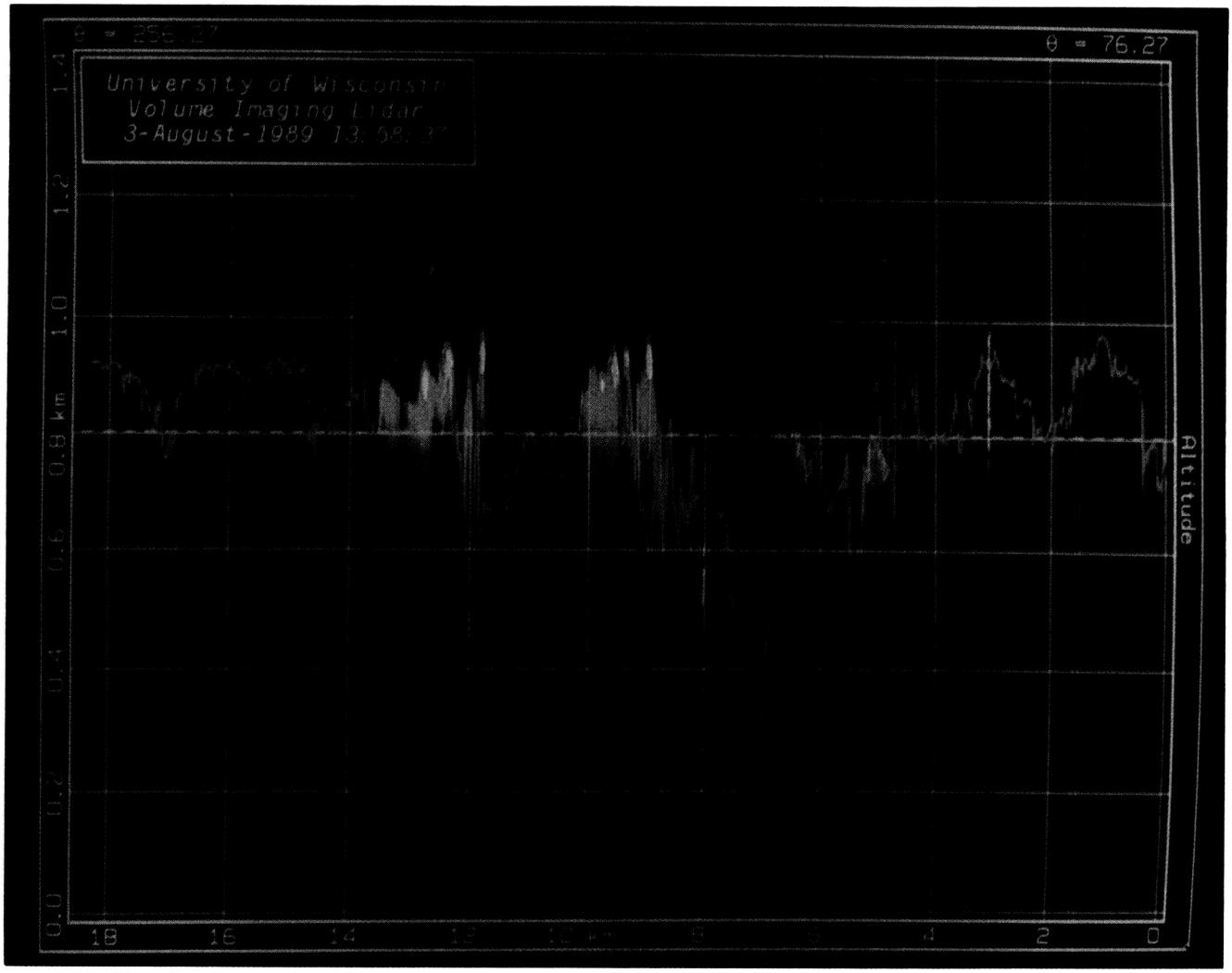

Plate 2. A composite RHI scan where aerosol structure in the volume scan is displaced to correct for motion caused by the mean wind between the time the aircraft sampled an air parcel and the time the lidar scanned the same parcel. The time when the volume scan was completed is displayed on the composite image. Water vapor mixing ratio variations for the flight beginning at 1854:53 UT on August 3, 1989, are superimposed on the lidar image. The distance of the aircraft from the lidar is shown on horizontal axis. An airplane symbol marks the location where aircraft and lidar measurements are coincident.

and direction agrees to within 2°. All lidar and aircraft speed measurements agree within 0.2 m s^{-1} and directions agree within 4°.

The ability of navigation and wind corrections to properly place aircraft measurements on the lidar images of air parcels can be judged by superimposing aircraft water vapor measurements on lidar images. Water vapor is selected because relative humidity strongly influences the optical scattering cross section of naturally occurring aerosols. Many of the aerosols are composed of hygroscopic materials [*Fitzgerald and Hoppel*, 1984; *Salemink et al.*, 1984], which grow by the accretion of water when the relative humidity exceeds the deliquescent point of the aerosol. This flight leg was just beneath the bases of small fair weather cumulus clouds, the relative humidity was large in the convective plumes and relatively low in the parcels entrained from above the mixed layer. These conditions produce a sharply defined lidar image to compare with the humidity measurements.

A composite RHI lidar scan, with a plot of the water vapor mixing ratio superimposed, is displayed in Plate 2. Wind corrections to the lidar image and the aircraft flight path were derived using the winds measured with the lidar (10.2 m s^{-1} at 215.2°).

Aerosol structure in the composite RHI is highly correlated with the aircraft-based water vapor measurements: regions of enhanced backscatter correspond to high values of humidity. In particular, note the tongue of dry air at a range of ~7 km. A close correspondence between the brightness of small-scale aerosol structure and the humidity trace is seen at all ranges between 5 and 9 km. The lidar scanned near the aircraft at a range of ~6.8 km, providing coincident measurements at this range. Thus temporal evolution of the structure does little to degrade the aircraft lidar comparison at the left-hand side of Plate 2. Plate 3 shows the RHI composite generated from the lidar volume scan obtained 187 s after Plate 2. In Plate 3 the aircraft and lidar data are nearly coincident at the extreme range of the lidar image. When Plate 2 is compared to Plate 3, temporal evolution of the structure is clearly evident. In Plate 3 the comparison

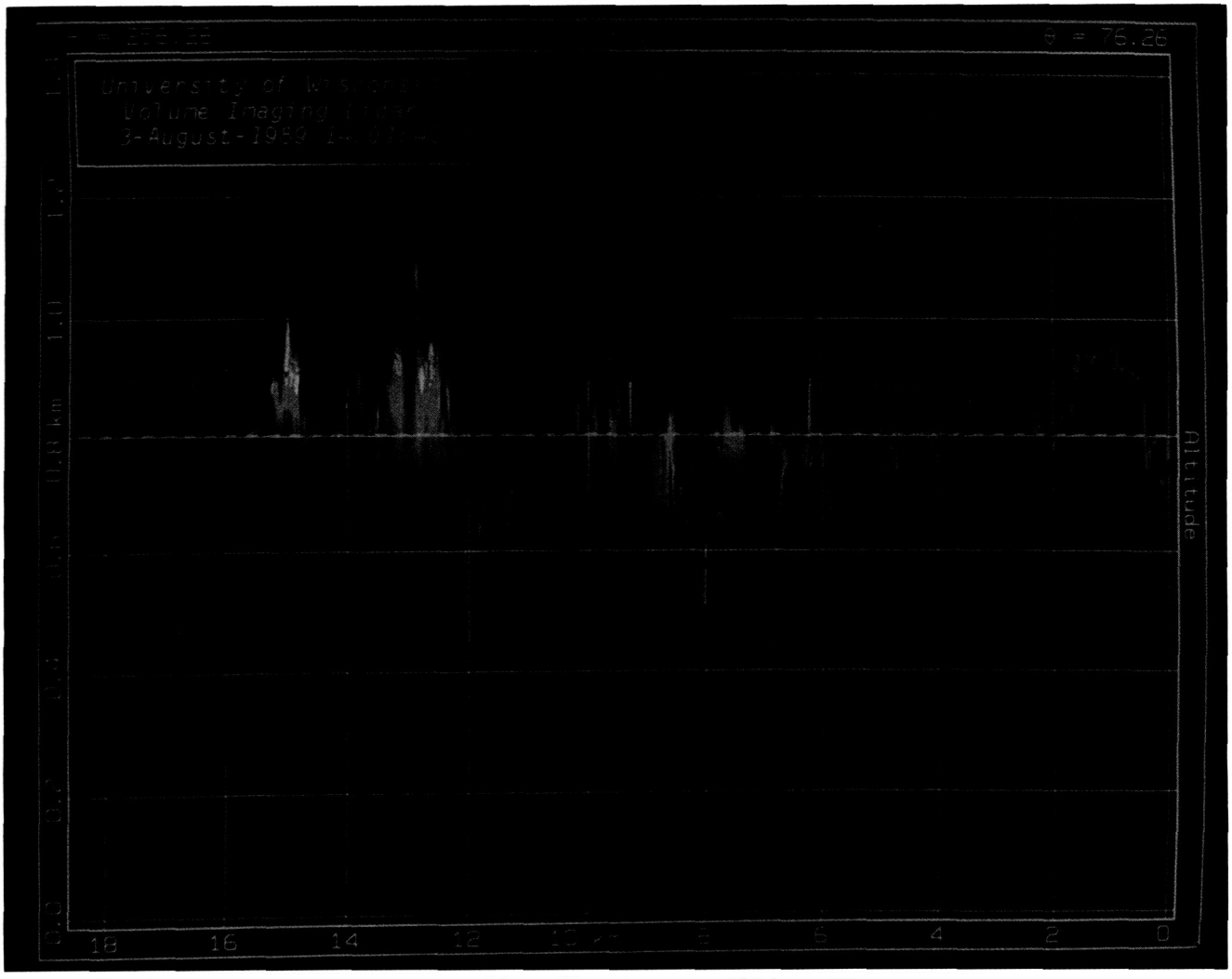

Plate 3. The composite RHI scan computed from a lidar volume scan which began 187 s after the scan used to produce Plate 2. In other respects this figure is identical to Plate 2.

between lidar and aircraft observations are best beyond 10 km. Note that the tongue of dry air shown near 7 km in Plate 2 has disappeared in Plate 3. The entire region between 10 km and 12.5 km has also become darker in Plate 3. This is consistent with the downdraft region apparent in the vertical velocity record (Figure 5).

The close correspondence between aerosol structure and humidity is further illustrated in Plate 4 where humidity is plotted on a wind-corrected CAPPI. In the region of the picture near the aircraft the comparison is good; for example, the small plume under the aircraft path 4.5 km south of the lidar appears as a sharp peak in the humidity trace. Up to a point 6 km south of the lidar, even very small features in the image match with the details of the humidity trace. Beyond 6 km south, small discrepancies appear. The dry region just beyond 6 km appears to correspond to a dark spot just north of the aircraft track, and a dry region just beyond 8 km south appears to correspond to a dark spot south of the aircraft track. This is caused by the time difference between the aircraft observations and the lidar image. Temporal evolution has modified the structure so as to reduce the correlation. The extent of the evolution in structure can be judged by comparing the CAPPI displayed in Plate 4 with the CAPPI observed 187 s later (Plate 5). In this image the large dry incursion of air that appears under the aircraft path 5 km south of the lidar is partly filled in by new plumes: one of these was just visible on the previous image (4.5 km south, 6.3 km west). In Plate 5 the image correlates well with the humidity trace at the southwest end of the picture but not as well in the northeast. For example, note the dry region just beyond 8 km south of the lidar; this now corresponds nicely to a dark spot in the image.

Figure 5 illustrates the well-known difficulty of measuring fluxes near the top of the mixed layer [*Lenschow and Stankov*, 1986]. In the course of the 15-km flight, only about five significant "flux events" are evident. Clearly, the statistical reliability of an estimate made from such a low number of events is poor. An examination of the vertical velocity trace shows the largest vertical velocity events near the lidar. Fluxes computed using this record will be very sensitive to the detail of any detrending or low-pass filtering of the vertical velocity trace.

The "top hat" humidity plume measured by the aircraft 10 km from the aircraft (Figure 5) marks the plume directly under a fair weather cumulus cloud shown at ~7 km south, 10 km west in Plate 1. Reference to the vertical velocity

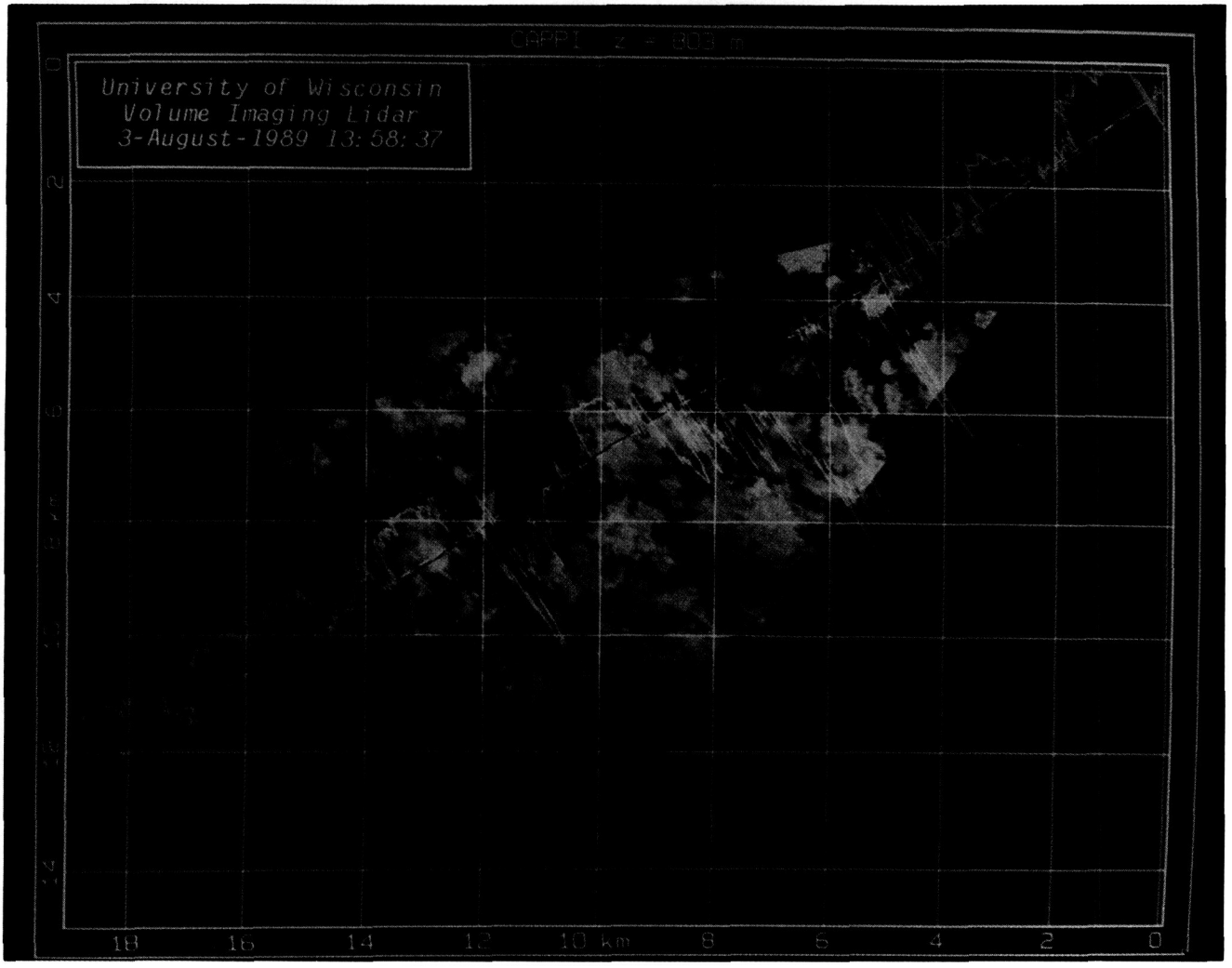

Plate 4. Wind-corrected CAPPI at the altitude of the aircraft flight measurements derived from the lidar volume scan obtained between 1855:43 UT and 1858:36 UT. Also plotted along the aircraft flight path is the variation of water vapor mixing ratio from its flight leg mean value. The image represents the position of aerosol features when the airplane passed over the lidar. Wind corrections were made using a mean wind speed of 10.2 m s^{-1} and direction of 215.2°.

inside the top hat shown in Figure 5 indicates that this plume is no longer supported by rising air. A second cloud at 9 km south and 13 km west in Plate 1 corresponds to the humidity top hat between 12.5 and 13.5 km in Figure 5. This cloud also shows little support from vertical velocity under the cloud. According to the classification of *Stull* [1985] both of these clouds are passive. It appears likely that if the aircraft had sampled fluxes under these clouds during their active phase, much larger fluxes would have been measured. Although the cloud shown between 12.5 and 13.5 km in Figure 5 exhibits little vertical velocity under the cloud, a flux contribution is provided by the downdraft directly to leeward of the cloud. The downdraft is clearly evident as a small dark spot in Plate 4.

Examination of the instantaneous fluxes of water, temperature, and carbon dioxide show the strongest single contribution from the downdraft located at ~7 km from the lidar (see Figure 5). This downdraft exhibits large fluctuations in the scaler quantities but only rather a small downward velocity (~0.25 m s^{-1}). It seems reasonable that the vertical velocity is small, since the negatively buoyant plume has already penetrated significantly into the mixed layer. The next CAPPI (Plate 5) shows elements of mixed layer air rising into much of the region occupied by the downdraft in first image; evidently, this parcel was nearing the end of its downward motion when sampled by the aircraft. Thus even though this downdraft represents the largest single flux event observed along the flight leg, it is likely that the local fluxes in the parcel were significantly larger prior to the aircraft observation. At an earlier time, before the negative buoyancy of the plume had time to slow the downward motion, we would expect stronger downdraft velocities.

Three of the prominent features in this record appear to have been sampled at times other than the time of maximum flux contribution. This indication that strong flux contributions by an individual thermal are transient adds to the difficulty of obtaining reliable flux measurements in the upper part of the mixed layer. Regions of strong vertical motion are sampled infrequently. Regions contributing large fluxes as a result of a combination of both large vertical velocities and large excursions in scaler quantities are therefore even more infrequent.

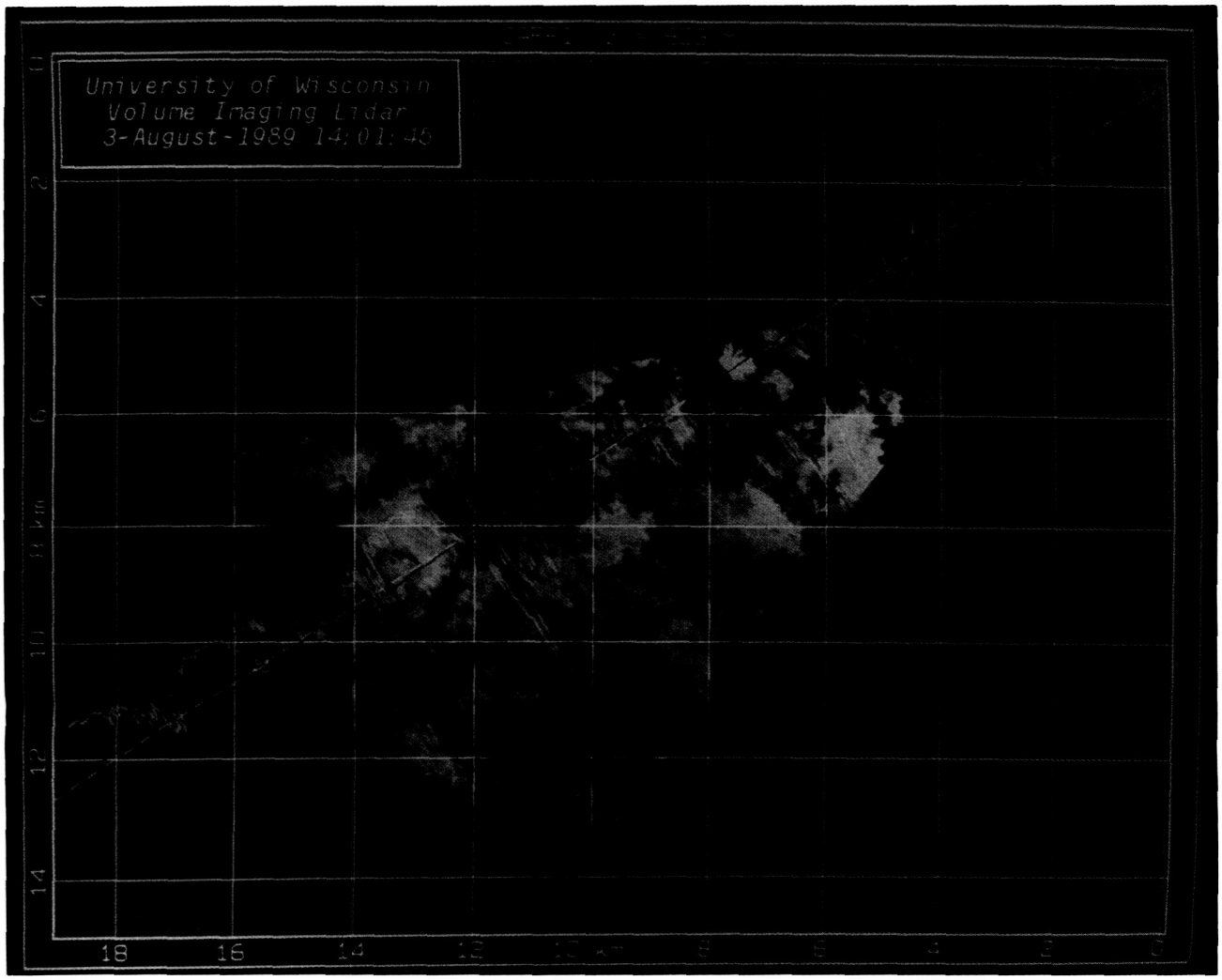

Plate 5. Wind-corrected CAPPI derived from the lidar volume scan obtained between 1858:50 and 1901:42 UT. This image is derived from the volume scan data acquired 187 s after Plate 4; otherwise, this figure is identical to Plate 4.

CONCLUSIONS

Volume-imaging lidar observations can be used to portray the atmospheric structure around the flight path of an instrumented aircraft. Because the current lidar technology requires approximately 3 min to map the three-dimensional structure, images must be corrected for distortion created by the wind. This paper shows that aircraft and lidar measurements can be successfully combined, even in the presence of 10 m s^{-1} winds. Loran provided aircraft navigation information; however, it was necessary to subtract a constant displacement vector from the Loran positions. Because a low-level flight over the lidar van was available to provide this offset, aircraft data matched lidar imagery without any additional navigation corrections. In future experiments, aircraft location information is expected to improve greatly with the introduction of global positioning system navigation. Evolution of the convective structures can be judged from successive lidar images; however, the rate of turbulent change is rapid, and higher lidar scan rates would be desirable.

A sample flight leg illustrates the well-known difficulties of measuring fluxes in the upper part of the mixed layer. It is clear that flight legs much longer than the 15-km legs used in this experiment are required to provide stable estimates.

Winds measured by lidar and aircraft show excellent agreement. When Loran was used to determine average aircraft velocity, flight-leg-averaged horizontal winds measured by the aircraft and area-averaged winds measured by lidar agree to within 0.2 m s^{-1} in speed and 1° in direction.

Acknowledgments. The authors wish to express their thanks to I. MacPherson of the NRC/NAE Flight Laboratory, R. Desjardins of Agriculture Canada Land Resource Research Center, and P. Schuepp of McGill University for providing the aircraft data used in this paper. Assistance in data acquisition was provided by J. Schols and D. Sharkey. Research funding for the acquisition and analysis of the lidar data was provided by NASA grant NAG 5-902 and Army Research Office grant DAA03-86-K-0024. Funding for design and construction of the lidar has been provided by a series of grants from the Army Research Office and the Office of Naval Research.

REFERENCES

Crum, D. T., R. S. Stull, and E. W. Eloranta, Coincident lidar and aircraft observations of entrainment into thermals and mixed layers, *J. Clim. Appl. Meteorol.*, *26*, 774–788, 1987.

Eilts, M. D., A. Sundara-Rajan, and R. J. Doviak, The structure of the convective atmospheric boundary layer as revealed by lidar and Doppler radars, *Boundary Layer Meteorol.*, *31*, 109–125, 1985.

Fitzgerald, J. W., and W. A. Hoppel, Equilibrium size of atmospheric aerosol particles as a function of relative humidity: Calculations based on measured aerosol properties, *Hygroscopic Aerosols*, edited by L. H. Ruhnke, pp. 21–34, A. Deepak, Hampton, Va., 1984.

Greenhut, G. K., and S. J. S. Khalsa, Convective elements in the marine atmospheric boundary layer, I, Conditional sampling statistics, *J. Clim. Appl. Meteorol.*, *26*, 813–822, 1987.

Hardy, K. R., and H. Otterster, Radar investigations of convective patterns in the atmosphere, *J. Atmos. Sci.*, *26*, 666–672, 1969.

Khalsa, S. J. S., and G. K. Greenhut, Convective elements in the marine atmospheric boundary layer, II, Entrainment at the capping inversion, *J. Clim. Appl. Meteorol.*, *26*, 824–336, 1987.

Konrad, T. G., and F. L. Robison, Development and characteristics of free convection in the free air as seen by radar and aircraft, *J. Appl. Meteorol.*, *12*, 1284–1294, 1973.

Kunkel, K. E., E. W. Eloranta, and S. T. Shipley, Lidar observations of the convective boundary layer, *J. Appl. Meteorol.*, *16*, 1306–1311, 1977.

Lenschow, D. H., and B. B. Stankov, Length scales in the convective boundary layer, *J. Atmos. Sci.*, *43*, 1198–1209, 1986.

MacPherson, J. I., NAE Twin Otter operations in FIFE 1989, *Inst. for Aerosp. Res. Lab. Tech. Rep. LTR-FR-113*, Nat. Res. Counc. Can., Ottawa, 1990.

Marht, L., and H. Frank, Eigenstructure of eddy microfronts, *Tellus*, *40*(A), 107–119, 1988.

Melfi, S. H., J. D. Spinhirne, S-H. Chou, and S. P. Palm, Lidar observations of vertically organized convection in the planetary boundary layer over the ocean, *J. Clim. Appl. Meteorol.*, *24*, 806–821, 1985.

Salemink, H. W. M., J. B. Bergwerff, and P. Schotanus, Quantitative lidar at 532 NM for vertical extinction profiles and the effect of relative humidity, *Appl. Phys. B*, *34*, 2774–2776, 1984.

Schols, J. L., and E. W. Eloranta, Calculation of area-averaged vertical profiles of the horizontal wind velocity from volume-imaging lidar data, *J. Geophys. Res.*, this issue.

Stull, R. B., A fair-weather cumulus cloud classification scheme for mixed-layer studies, *J. Clim. Appl. Meteorol.*, *24*, 49–56, 1985.

Stull, R. B., *An Introduction to Boundary Layer Meteorology*, Kluwer Academic, Boston, Mass., 1988.

E. W. Eloranta and D. K. Forrest, Department of Meteorology, University of Wisconsin, 1225 W. Dayton Street, Madison, WI 53706.

(Received February 6, 1991;
revised April 6, 1992;
accepted April 9, 1992.)

Submitted

Convective boundary layer mean depths, cloud base altitudes, cloud top altitudes, cloud coverages, and cloud shadows obtained from Volume Imaging Lidar data

Antti K. Piironen and Edwin W. Eloranta

University of Wisconsin–Madison

Department of Atmospheric and Oceanic Sciences

1225 West Dayton Street

Madison, WI 53706

Abstract

This paper presents automatic methods for obtaining convective boundary layer mean depths, cloud base altitudes, cloud top altitudes, cloud coverages, and cloud shadows using the University of Wisconsin Volume Imaging Lidar (VIL). These methods provide mesoscale observations representing the 70 km^2 scanning area of the VIL. All data obtained with the VIL during the 1989 FIFE field experiment are analyzed and the results are summarized. The reliability of these methods is verified by comparing the results with radiosonde profiles, satellite images, and visual estimates from Range Height Indicator scans of the VIL.

1. Introduction

Convective boundary layer (CBL) mean depths, cloud coverages, cloud base altitudes, and cloud top altitudes are traditionally measured with satellites, radiosondes, and weather stations. Most applications try to describe the atmospheric conditions in large areas prompting a need for area averaged measurements. Representative area averaged observations are generally achieved by applying time-averaging to ground-based point measurements. However, a long averaging time interval does not necessarily guarantee a representative area average, since the point measurements can be biased by local variations. The accuracy of short averages is limited by convection scale inhomogeneities. This paper introduces methods for obtaining area averaged measurements of CBL mean depths, cloud coverages, cloud base altitudes, and cloud top altitudes with the University of Wisconsin Volume Imaging Lidar (VIL). These measurements provide stable averages over $\sim$70 km^2 area with a 3-minute time resolution.

The VIL [*Eloranta and Forrest*, 1992] is a scanning lidar capable of mapping elastic backscatter from aerosols in a large volume. The current VIL system configuration is summarized in Table 1. The VIL has a 10 MHz analog-to-digital conversion rate and 1 kilobyte data buffer length that allow a 15 km detection range with a 15 m range resolution. The data acquisition system normalizes the backscatter profiles for laser output energy fluctuations, corrects the range square dependence, and forms a natural logarithm of the signal before saving it in compressed form on optical disks. Scanning is performed with a beam steering unit mounted on the optical axis of the system. Figure 1 illustrates a VIL volume scan. For the convective boundary layer studies, the VIL typically scans 15° high and 40° wide sectors with 0.33° and 0.5° angular step sizes, respectively. The VIL devotes about 3 minutes to scan this $\sim$100 km^3 volume.

The VIL was operated in the First ISLSCP (International Satellite Land Surface Climatology Project) Field Experiment (FIFE) site [*Sellers et al.*, 1992] from July 26 to August 11, 1989. It recorded $\sim$ 2000 boundary layer volume scans consisting of $\sim$ 20 gigabytes of raw data. In earlier studies [*Boers and Eloranta*, 1986; *Crum et al.*, 1987; *Nelson et al.*, 1989], the convective boundary layer mean depth and entrainment zone thickness were measured by a visual inspection of Range Height Indicator (RHI) scans. Due to the enormous amount of raw data from the 1989 FIFE program, the visual inspection was impractical. Therefore, automatic analysis methods for measuring CBL mean depths, cloud base altitudes, cloud top altitudes, cloud coverages, and cloud shadows were essential in order to analyze all data from the experiment.

2. Methods

2.1. Convective Boundary Layer Mean Depth in Clear Air

The fair-weather convective boundary layer is characterized by rising thermals of aerosol rich air and sinking streams of air from the free atmosphere. These vertical motions cause irregularities in the boundary layer top which can be observed from the RHI scans of the VIL (see Figure 2). Because of insufficient sampling of the undulating CBL top, traditional point measurements of the CBL depth are not representative.

The CBL top is typically marked with a sudden lidar backscatter intensity change due to different aerosol concentrations in and above the boundary layer. When visually inspecting RHI scans, we have adopted the definition by Deardorff et al. (1980) for the CBL mean depth: the altitude which has equal areas of free air below and boundary layer aerosols above. In automatic estimation, we determine the CBL mean depth from the horizontal signal variance [*Hooper and Eloranta*, 1986].

The horizontal aerosol variations are intense at the altitude of the CBL mean depth because of undulations at the top of the CBL. To calculate the vertical profile of horizontal signal variations, each shot in a volume scan is first high pass filtered with an 1 km long median filter. This eliminates atmospheric extinction and scattering from uniformly distributed aerosols. Using a 20 m vertical spacing, backscatter signals from each altitude range are mapped on horizontal planes. Then, the variance of the aerosol signal on each horizontal plane is calculated. The lowest altitude local maximum peak of the variance profile marks the convective boundary layer mean depth.

The bottom-up approach eliminates errors due to strong aerosol variability caused by aerosol layers above the CBL. Local maximas induced by dust clouds are rejected by requiring that the peak is stronger than the average of the signal variance profile. Random variance fluctuations due to signal noise can disturb detection of maximum variance when the difference in backscatter from boundary layer aerosols and free air is small. To prevent selection of a random local maximum we check not only that the points either sides of the maximum point are smaller than the maximum, but also that these adjacent points are larger than the next closest points, i.e. $\sigma(z_{max} - 2\Delta z) < \sigma(z_{max} - \Delta z) < \sigma(z_{max}) > \sigma(z_{max} + \Delta z) > \sigma(z_{max} + 2\Delta z)$.

The automatic method provides a convective boundary layer mean depth estimate representing an average over ~ 70 km^2. Figure 2 shows an RHI scan, the VIL signal variance profile, and the estimated CBL mean depth. The automatic method is tested by comparing the results with manually inspected estimates. The manual estimation is performed by determining the altitude which has equal areas of boundary layer aerosols above and sinking air below. Figure 3 compares manually and automatically determined convective boundary layer mean depths and estimates from radiosonde-based potential temperature profiles on July 28, 1989, from 8:00 to 10:00 CDT. Because of the large number of RHI scans during the session, the manual inspection is performed for three RHI scans in the same volume scan every fifth volume scan. The variability of manual estimates increase in time due to growing undulations at the top of the CBL. The automatic estimates are consistent and show a smooth CBL growth over time. The fluctuation in the automatic results at 9:50 CDT is due to a missing data block in the volume scan; the transmitter laser beam was turned off when an aircraft flew into the field of view.

The plot of potential temperature profiles used for estimating the CBL mean depths in the previous case is plotted in Figure 4. Traditionally, the CBL top is located from a jump in the potential temperature profile. Since the radiosonde is a point measurement

system, the potential temperature soundings are sensitive to the spatial distribution of the thermal plumes. The potential temperature profile can be measured through a rising plume or through a downward stream of free air penetrating deep in the CBL. This can lead to uncertainties which are in the order of the CBL mean depth. The potential temperature profile at 8:01 CDT shows a 100-150 m CBL mean depth, which is consistent with the VIL measurements. The CBL depth is very difficult to determine from the profile at 9:36 CDT. The first potential temperature jump is at $\sim$ 300 m, which is $\sim$ 200 m lower than the VIL estimates. The profile also shows an instability at $\sim$ 700 m, which was probably due to the radiosonde rising through a thermal. Thus, the CBL top is most probably at $\sim$ 730 m, where the potential temperature starts to rise again. However, the radiosonde profile was most probably measured through a high plume top.

2.2. Convective Boundary Layer Mean Depth with Clouds

When cloudiness increases, echoes from clouds can bias the CBL depth estimate by dominating the variance. In such cases, the maximum variance represents the altitude of the maximum cloud echo variability instead of the convective boundary layer mean depth. The method for determining CBL mean depths in the presence of a few low altitude clouds is similar to the clear air case described in the previous section, except the shadowed regions behind clouds are removed before computing the horizontal variance.

Figure 5 presents a comparison between manually and automatically determined CBL mean depths from the 1989 FIFE program. The manual and automatic estimates correlate well. Only data with the cloud coverage less than 10% is plotted, since in presence of more clouds, both automatic and manual method can give biased results due to cloud shadows. When the CBL mean depth is below 200 m, both methods may give statistically poor estimates, since the lidar images often shows only the tops of the plumes. Therefore,

there may not be enough information to determine the CBL mean depth. Otherwise, the deviations are mostly due to under-sampling of undulating CBL top in the manual method, which causes typically 100–200 m variations in estimates. In order to understand better the scatter in this plot, some of the most extreme discrepancies are reanalyzed. Boxes **a** and **c** mark CBL top estimates which were difficult to determine with the manual method due to low contrast between boundary layer aerosols and free air. Box **b** marks points, where a haze layer just above the CBL was manually misinterpreted as the CBL top. After reinterpretation, the manual estimates in marked boxes are within 100 m of the automatic measurements.

In the presence of a significant convective clouds coverage, the definition of a boundary layer mean depth is unclear and the previously presented convective boundary layer mean depth determination is invalid. For example, near a thunderstorm cloud with a cloud top at 10 km, the local boundary layer would be 5 km by the definition we have adopted. In the presence of low clouds, the cloud base and cloud top altitudes are presented. In these cases, the values of the mean depth must be interpreted with a great caution. Figure 6 presents an RHI scan along with a signal variance profile and the CBL mean depth estimate. Cloud echoes cause a strong variance. The automatically determined CBL mean depth is slightly higher than the manual estimate.

2.3. Cloud Base Altitude

The lidar backscatter echo from a cloud is detected as a strong positive signal gradient (see Figure 7). The first signal gradient equal to the maximum slew rate of the detector amplifier is used to define the cloud base. The gradient is calculated from three subsequent data points to prevent misinterpreting noise induced signal gradients as clouds. To obtain representative cloud base estimates, all shots in a volume scan are inspected for cloud

echoes and the lowest cloud echo defines the cloud base altitude. This method provides the lowest cloud base altitude in the $\sim$ 70 km^2 VIL scanning area. Sometimes the VIL backscatter signal includes echoes from ground objects and dust clouds, which are similar to cloud echoes. Therefore, every cloud echo below 200 m is omitted in the cloud calculations.

Figure 8 presents an RHI scan with a histogram of the first cloud return altitudes and an estimated cloud base. The cloud base is measured with $\sim$50 m accuracy. Clouds are good scatterers and are clearly visible in an RHI scan. However, when inspecting cloud bases from the RHI scans, the visual difference between thermals and clouds depends on the color enhancement selected for the display terminal. For example, some clouds in Figure 8 seem to extend below the detected cloud base, since the chosen color enhancement shows backscattering from aerosols and clouds with similar grey shades. An accurate visual estimation of the cloud base from the RHI scans requires a well trained eye and careful setting of enhancement levels.

The automatic cloud base altitude estimates correlate well with the manually determined estimates. Figure 9 represents the manual and automatic cloud base estimates for the 1989 FIFE experiment data. Only those cases with cloud coverage greater than 5% are analyzed. To reduce statistical fluctuations from sampling differences, a 15-minute minimum filter is applied to the results. Most manual estimates are greater than or equal to automatic estimates. The manual method samples only $\sim$1 % of the RHI scans and it is unlikely to sample lowest clouds in the volume scan causing systematic over estimation. We expect to have statistical fluctuations of $\sim$50 m, since the vertical resolution is limited by the elevation angle step size used in the volume scan. Boxes **a**–**d** mark regions where manual estimates are substantially higher than the automatic measurements. The visual estimates for these cases have been re-examined to explain the differences. One sample in box **c** is due to a dust cloud rising up to 500 m, which caused the automatic method to fail. The other measurements in box **c** were made when there was a cloud layer above a few

fair-weather cumulus clouds. In this case, the manual method missed the lower clouds due to insufficient sampling. Boxes **e** and **f** mark manual estimates which are more than 200 m lower than the automatic measurements. These are due to choosing an inappropriate color enhancement in visual inspection of the RHI scans showing thermal plumes and aerosol swelling as clouds causing under estimated manual cloud base altitudes. After reinterpretation of the RHI scans, the manual estimates in the marked boxes return within 50 m of the automatic estimates. When values in boxes **a–f** are reanalyzed, the root-mean-square difference between the the automatic and manual results is ~67 m.

2.4. Cloud Top Altitude

Clear lines of sight are required for a reliable cloud top altitude estimate, since the extinction in a cloud often blocks the lidar signal before the cloud top is reached. A lidar pointing directly to zenith can only detect tops of optically thin clouds. However, the three-dimensional scanning capability of the VIL extends the visibility of cloud tops by looking through holes in the cloud deck. This makes the cloud top detection possible for scattered, optically thick clouds.

Assuming that 1) the horizontal scales of clouds are approximately equal to CBL mean depth, 2) the shape of clouds is square, and 3) the clouds are uniformly distributed, we can derive an approximate equation for the maximum detectable cloud height h as a function of the observation angle, fractional cloud coverage C, CBL mean depth z_i, and penetration depth d_p of the lidar signal into a cloud as

$$h \approx \left(\left(\frac{1}{\sqrt{C}} - 1 \right) z_i + d_p \right) \tan\theta \qquad (1)$$

where θ is the maximum observation angle ($< 90°$). The penetration depth of the VIL signal into clouds is generally greater than 200 m. This equation provides rough limits of

the cloud top detection in presence of optically thick clouds. For example, if $z_i = 1$ km, $C = 0.25$, and $\theta = 10°$, then the cloud tops below ~1200 m can be detected, even for optically thick clouds.

The maximum altitude of the last returns from clouds in a volume scan defines the cloud top altitude. The last cloud return is marked by a rapidly falling signal after cloud maximum return (see Figure 7). Because a strong extinction in an optically thick cloud may cause a similar signature, the rest of the backscatter profile is checked for remaining backscatter. The ratio of lidar profiles penetrating through the cloud layer to all cloud top returns indicates the reliability of the cloud top estimate. The cloud top altitude is manually detected from an RHI scan as the highest visible cloud structure. Figure 10 shows an RHI with a histogram of the last returns from clouds and a cloud top estimate. The cloud top estimate is higher than one would estimate from this RHI scan, since the automatic cloud top is calculated using the whole volume scan.

The automatic cloud top altitude estimates correlate with the manual estimates, as shown in Figure 11. A 15-minute maximum filter is applied to the results to reduce statistical fluctuations due to sampling rate differences between the methods. Box **a** marks the point where a dust cloud rising up to 500 m caused the automatic method to fail. Boxes **b** and **e** mark points where a human error caused spurious values in the manual estimates. Boxes **c**, **d**, and **f** mark points where a higher cloud layer was missed by the manual method, since the vertical range of the display was set too small. After reinterpretation of RHI scans, the manual results marked in boxes **b–f** are within 50 m of the automatic estimates. In cases of partly transparent clouds, the manual method sometimes provides higher cloud top estimates, since it can detect faint cloud echoes above the top of the first cloud layer. When clouds are optically thick, both methods have the same visibility problems. The automatic method, however, samples each shot and thus provides more representative estimates due to better sampling coverage.

2.5. Cloud Coverage and Cloud Shadows

Cloud coverage is defined as the percentage of ground surface area with clouds directly above. The cloud echoes and signal echoes are mapped into a horizontal grid according to their horizontal positions. The ratio of grid points with cloud echoes to all grid points with signal echoes defines the cloud coverage percentage. The VIL can map clouds on areas as small as $\sim$ 2000 m^2 within the scanning area. Cloud coverage estimation is also possible using a larger portion of the scanning area up to $\sim$ 70 km^2.

The measurement geometry limits the accuracy of the cloud coverage estimates. The coverage decreases towards the end of the scan range since the lowest cloud elements at close range may block the view of clouds with slightly higher bases. To minimize this error, the cloud coverage is calculated using 5 km long and 5 km wide grids starting from the closest possible range for the cloud base altitude and the maximum elevation angle of the scan. In terms of elevation angles, this means that the coverage of a cloud layer at 1 km is measured using scanning angles between 6.5° and 15° to enable complete cloud base coverage when the lowest cloud elements are less than 100 m below the highest cloud base. Figure 12 shows the cloud echo projections to the ground and the spatial coverage of the backscattering returns. Cloud coverage is about 25% in this case.

To verify the cloud mapping capability of the VIL, cloud coverage estimates are compared with satellite imagery data. Figure 13 compares cloud mapping based on VIL data with the visual wavelength band (0.572–0.698 μm) image of the satellite-based Advanced Very High Resolution Radiometer (AVHRR) instrument on the NOAA-11 satellite platform. The cloud base altitude was 1.4 km; the cloud top altitude was 2.4 km. The view angle of the AVHRR was 21.9° from zenith and 258.5° clockwise from North. Similar

cloud structures can be seen in both images. The main differences are due to the spatial resolution differences; the areal resolution of VIL is about five hundred times better than the 1 km pixel resolution of the AVHRR.

The percentage of ground shadowed by clouds generally differs from the cloud coverage. In most studies requiring cloud shadow information, shadows are estimated using cloud coverage measurements with assumed cloud shape. This works well in large areas, but when large scale cloud shadow estimates are combined with local scale radiometric measurements the result may be biased, since locally the cloud coverage and shadows can differ substantially. Clouds can block the direct sunlight, but the sky may be clear directly above, and vice versa.

The cloud mapping capabilities of the VIL enable the determination of cloud shadows on the ground. Cloud shadows are restored by geometrically projecting the cloud returns onto the ground using an actual sun angle. The cloud shadow estimates can be calculated for areas as small as $\sim$ 2000 m^2. Local cloud shadow and cloud coverage estimates of the VIL can be used to determine the cloud effects on local radiometer measurements. Then, the VIL cloud coverage estimates can be used to estimate the area-averaged radiation.

3. Results and Discussion

Figure 14 summarizes the CBL mean depths, cloud base altitudes, cloud top altitudes, and cloud coverages derived from the VIL boundary layer volume scans recorded during the 1989 FIFE. The results are filtered with 15-minute long filters: the CBL mean depths with a median filter, the cloud bases with a minimum filter, the cloud tops with a maximum filter, and the cloud coverages with an average filter.

When clouds are connected to the CBL, the CBL mean depth estimate should be interpreted as the altitude of maximum cloud echo variation, as for example, on July 30 from 9:00 to 10:00 CDT, when the CBL mean depth estimate varies widely between cloud base and top. In a case of multiple cloud layers, the cloud base altitude represents the base of the lowest cloud layer, while cloud top altitude represents the top of the highest cloud layer. That is the case on August 5 and August 11, when there is occasionally more than 1 km difference between the cloud base and top altitudes. Clouds above ~4 km are not observed from the volume scans, since the maximum elevation angle of the boundary layer scans limits the altitude range. For the same reason, cloud coverage may be underestimated for cloud layers higher than 3.5 km.

If cloud coverage is high, the cloud top altitudes may be too low due to missing lines of clear sight. On overcast days, such as August 1–3, the cloud top estimates are probably too low due to optically thick clouds blocking the backscatter profiles. For example, on August 2 from 10:00 to 12:00 CDT, when the cloud coverage is close to 100%, the cloud heights are limited by the backscatter signal penetration depth in clouds. When the cloud coverage is less than 70%, higher cloud heights were observed indicating that the method works successfully.

4. Conclusions

Automatic methods for obtaining cloud coverages, cloud base altitude, cloud top altitudes, and convective boundary layer mean depths provide measurements which are averaged over 25–70 km^2. All VIL data recorded during the 1989 FIFE program are analyzed, providing information about boundary layer parameters in various atmospheric conditions. The accuracies of CBL mean depths and cloud base altitudes are limited mainly by the vertical resolution of the VIL.

The automatic CBL mean depth estimates correlate with the manually inspected estimates from RHI scans. Both the automatic and manual method for CBL mean depth estimates may have large uncertainties when the CBL is lower than 200 m, since the lidar frequently detects only the plume tops. The definition of the CBL mean depth becomes unclear in the presence of convective clouds. The automatic convective boundary layer mean depth estimate is valid if the coverage of convective clouds is less than ~10%. If more clouds are present, the maximum aerosol backscatter variance represents the altitude of maximum cloud echo variance, which usually is higher than the CBL mean depth.

In this study, the maximum altitude of cloud detection is limited below ~ 3.5 km by the maximum elevation angle of the boundary layer volume scan. The root-mean-square difference between automatic and manual cloud base estimates is ~67 m. The cloud top estimates are usually too low in overcast conditions due to lidar signal extinction in optically thick clouds. When a 15-minute long maximum filter is applied to the cloud top estimates, there usually are enough clear lines of sight through the cloud layer for reliable cloud top determination up to 70% cloud coverage.

Acknowledgments

The authors wish to express their gratitude to D. Forrest for managing the lidar data acquisition. AVHRR satellite images are produced by the FIFE Information System staff, whose work is appreciated. The radiosonde data were measured by a team from Cornell University, directed by Prof. W. Brutsaert. Financial support to Antti Piironen is provided by Finnish Academy, Alfred Kordelin Foundation, Finland, Suomen Kulttuurin Edistämissäätiö Foundation, Finland, and University of Joensuu, Finland. The VIL was supported by NASA Grant NAG-5-902 and Army Research Office Grants DAAL03-86-K-0024 and DAAL03-91-C-0222.

References

Boers, B., and E.W. Eloranta: "Lidar Measurements of the Atmospheric Entrainment Zone and the Potential Temperature Jump Across the Top of the Mixed Layer", *Boundary Layer Meteorology*, **34**, 357–375, 1986.

Crum, T.D., R.B. Stull, and E.W. Eloranta: "Coincident Lidar and Aircraft Observations of Entrainment into Thermals and Mixed Layer", *Cli. Appl. Meteor.*, **26**, No. 7, 774–788, 1987.

Deardorff, J.W., G.E. Willis, and B.H. Stockton: " Laboratory Studies of the Entrainment of a Convective Mixed Layer", *J. Fluid Mech.*, **100**, 41–64, 1980.

Eloranta, E.W. and D.K. Forrest: "Volume Imaging Lidar Observations of the Convective Structure Surrounding the Flight Path of a Flux-Measuring Aircraft", *J. Geophys. Res.*, **97**, No. D17, pp. 18,383–18,393, 1992.

Hooper, W.P. and E.W. Eloranta: "Lidar Measurements of Wind in the Planetary Boundary Layer: The Method, Accuracy and Results from Joint Measurements with Radiosonde and Kytoon", *J. Climate Appl. Meteor.*, **25**, No. 7, 990-1001, 1982

Nelson, E., R. Stull, and E.W. Eloranta: "A Prognostic Relationship for Entrainment Zone Thickness", *J. Appl. Meteor.*, **28**, No. 9, 885–903, 1989.

Sellers, P.J., F.G. Hall, G. Asrar, D.E. Strebel, and R.E. Murphy: "An Overview of the First International Satellite Land Surface Climatology Project (ISLSCP) Field Experiment (FIFE)", *J. Geophys. Res.*, **97**, No. D17, 18,345–18,371, 1992.

Tables:

Table 1.	VIL Specifications
Transmitter	
Wavelength	1064 nm (Nd:YAG)
Average Power	20 W
Repetition Rate	30 Hz
Receiver	
Telescope Diameter	50 cm
Optical Bandwidth	1 nm
APD Quantum Efficiency	~35 %
Range Resolution	15 m
Maximum Angular Scan Rate	$20°s^{-1}$
Data Rate	~ 500 MB/h
Data Acquisition	
Controlling Computer	VAX 11/750
Real-time Graphics	Stellar GS1000
Optical Disk	C.Itoh OPCA-11 (2.6 GB disks)
Data Processing	IBM RS6000 Model 550

Figure Captions:

Fig. 1. The VIL scan pattern employed during the 1989 FIFE. A volume scan consists of an azimuthal sequence of elevation angle scans. The shaded areas illustrate aerosol structures.

Fig. 2. An RHI scan, the variance of the filtered backscatter signal as a function of altitude (white curve), and the convective boundary layer mean depth estimate (black dashed line) on August 9, 1989, at 11:03 CDT. Aerosol structures are shown as brighter areas; cleaner air penetrating from free atmosphere is darker. The CBL top undulations are clearly visible.

Fig. 3. Comparison between manually (solid circles) and automatically (open circles) determined boundary layer mean depths on July 28, 1989. Open squares mark CBL mean depth estimates determined from radiosonde-based potential temperature profiles at 8:01 and 9:36 CDT. All RHI scans from 9:33 to 9:36 CDT were carefully reanalyzed to explain the difference between the VIL measurements and the radiosonde-based measurement. The solid circle at 9:33 CDT shows the average CBL depths obtained from individually inspected RHI scans; the triangle shows the average altitude of the deepest downward streams of clear air; the diamond shows the average altitude of highest plume tops. The vertical bars show minimas and maximas of the estimates. The plume top estimates indicate that the radiosonde profile at 9:36 CDT was measured through a high thermal plume top.

Fig. 4. Potential temperature profiles measured with radiosondes on July 28, 1989, at 8:01 and 9:36 CDT.

Fig. 5. Automatically vs. manually determined convective boundary layer mean depth with low cloud coverage from July 26 to August 11, 1989. Boxes **a** and **c** mark points where the CBL mean depth was hard to determine using the manual method due to low contrast between the boundary layer aerosols and free air; box **b** marks points which were manually misinterpreted. After reinterpretation, the manual estimates in these boxes are within 100 m of the automatic estimates.

Fig. 6. An RHI scan image, a variance of the filtered backscatter signal as a function of altitude (white curve) and the CBL mean depth estimated from the variance profile (dashed black line) on August 2, 1989, at 12:00 CDT. Bright structures on the RHI scan represent cloud echoes. In this case, clouds make estimation of the CBL mean depth uncertain.

Fig. 7. A VIL backscatter profile on July 26, 1989, at 10:48 CDT. Strong signal gradients characterize cloud echoes. The elevation angle of the profile is 15°. The irregularities below the first cloud return are due to boundary layer aerosols. The insert figure shows aerosol fluctuations expanded by a factor of ten.

Fig. 8. An RHI scan, a histogram of the first cloud echoes (white line), and estimated cloud base (black dashed line) on August 2, 1989, at 12:00 CDT. Bright structures represent cloud echoes. Histogram peaks near the ground are caused by echoes from dust clouds and ground objects.

Fig. 9. Cloud base altitude estimates using the manual method vs. automatic method from July 26 to August 11, 1989. Boxes **a–d** mark regions where the manual method missed the lower clouds due to sparse sampling. The highest sample in box **c** is due to an unusually high dust cloud, which caused the automatic method to fail. Box **e** marks a sample where aerosol swelling from a cloud was misinterpreted as a cloud in manual estimation. Box **f** marks a sample where the top of a thermal plume was misinterpreted as a cloud.

Fig. 10. An RHI scan, a histogram of the last cloud returns (white line), and estimated cloud top (black dashed line) on August 2, 1989, at 12:00 CDT.

Fig. 11. Cloud top altitude estimates using the manual method vs. automatic method from July 26 to August 11, 1989. Box **a** marks a point where a dust cloud at 500 m caused the automatic method to fail. Boxes **b and e** mark points where a human error caused spurious values in the manual estimates. Boxes **c**, **d**, and **f** mark points where a higher cloud layer was missed by the manual method, since the vertical range of the display was set too small.

Fig. 12. Horizontal map of VIL cloud echoes on the ground on July 26, 1989, at 11:00 CDT. Grey and white areas indicate coverage by backscatter profiles and cloud echoes, respectively.

Fig. 13. Comparison between a VIL cloud map (rectangle at upper-right corner) and an AVHRR visual band image (background) on July 28, 1989, at 15:00 CDT. The AVHRR image is enhanced to show clouds as white and the ground as black. The arc represents the VIL scanning area.

Fig. 14. Summary of CBL mean depths (lines with open circles), cloud bases (lines with triangles up), cloud tops (lines with triangles down), and cloud coverages (solid line) for the 1989 FIFE.

Figures:

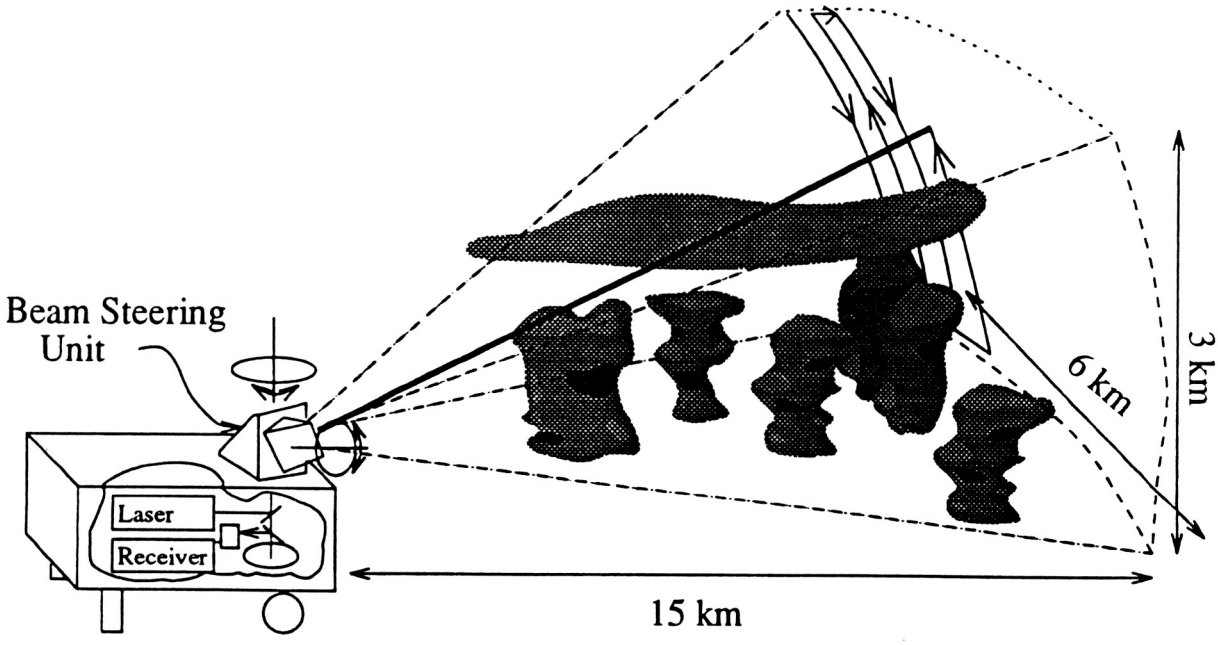

Fig. 1.

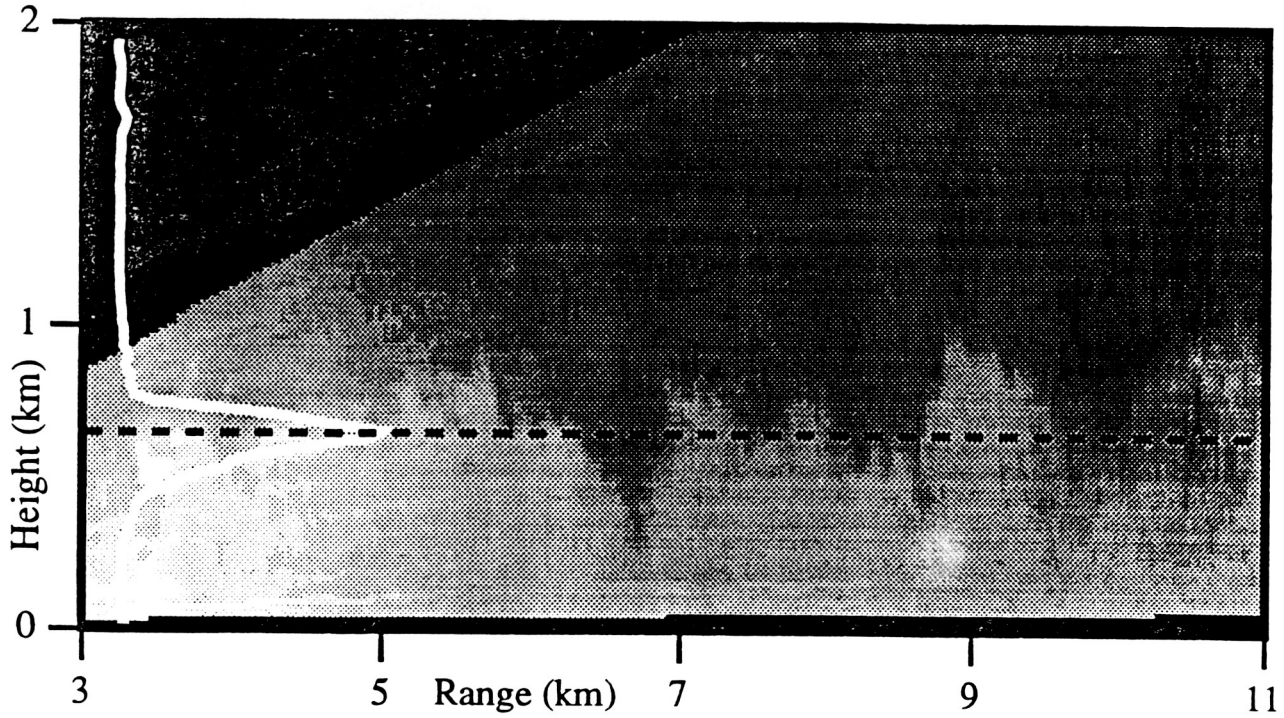

Fig. 2.

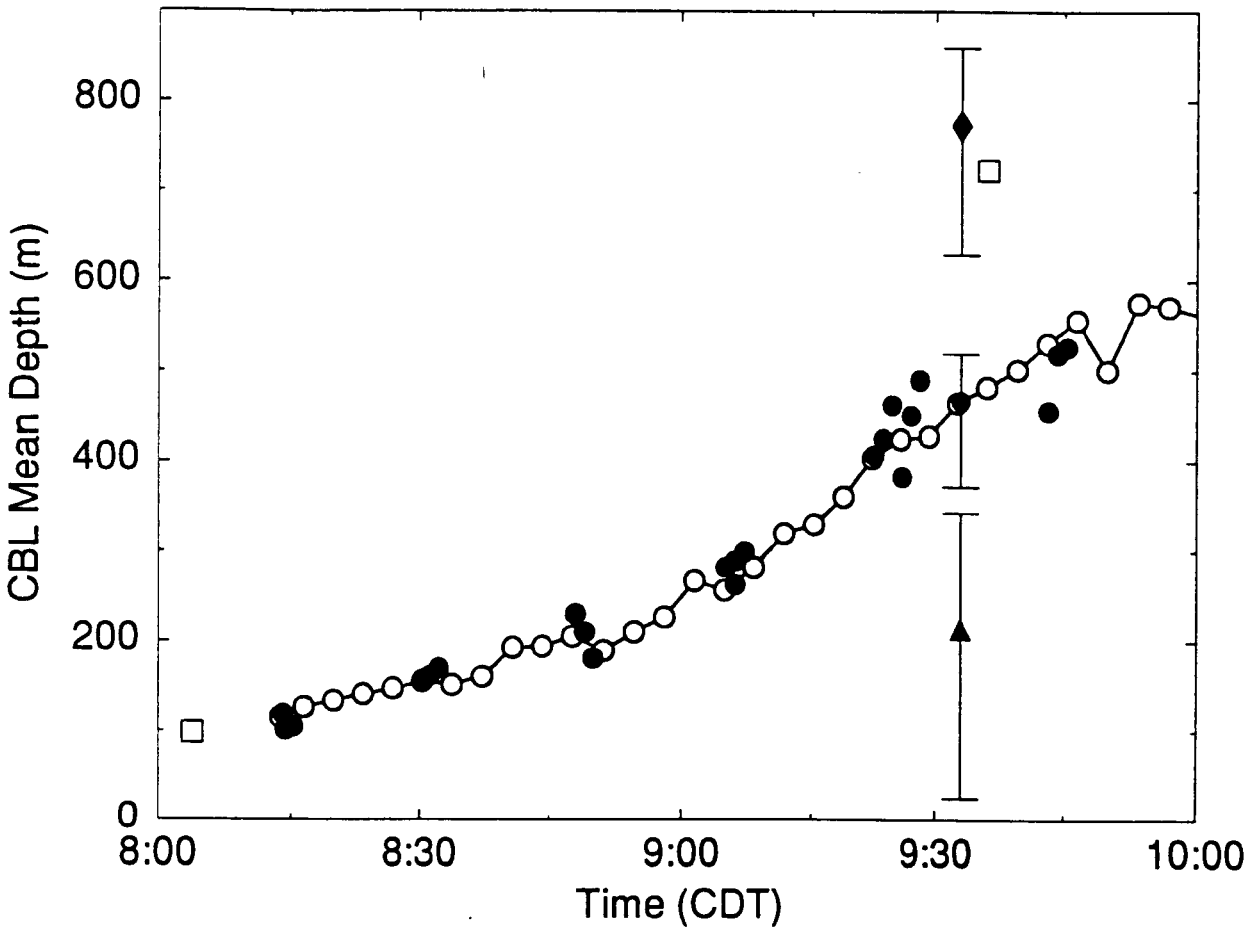

Fig. 3.

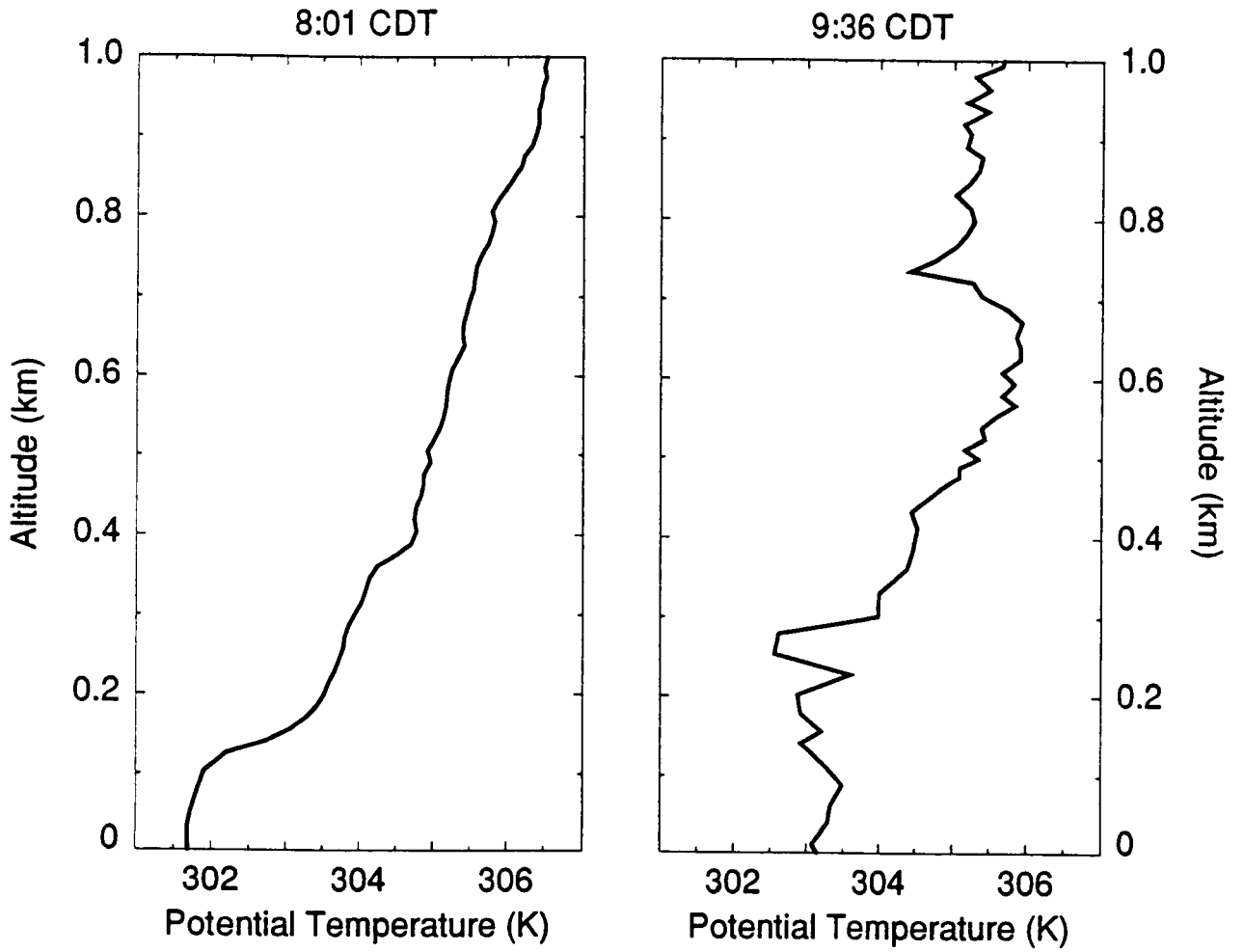
8:01 CDT
9:36 CDT
Altitude (km)
1.0
0.8
0.6
0.4
0.2
0
302
304
306
Potential Temperature (K)

Fig. 4.

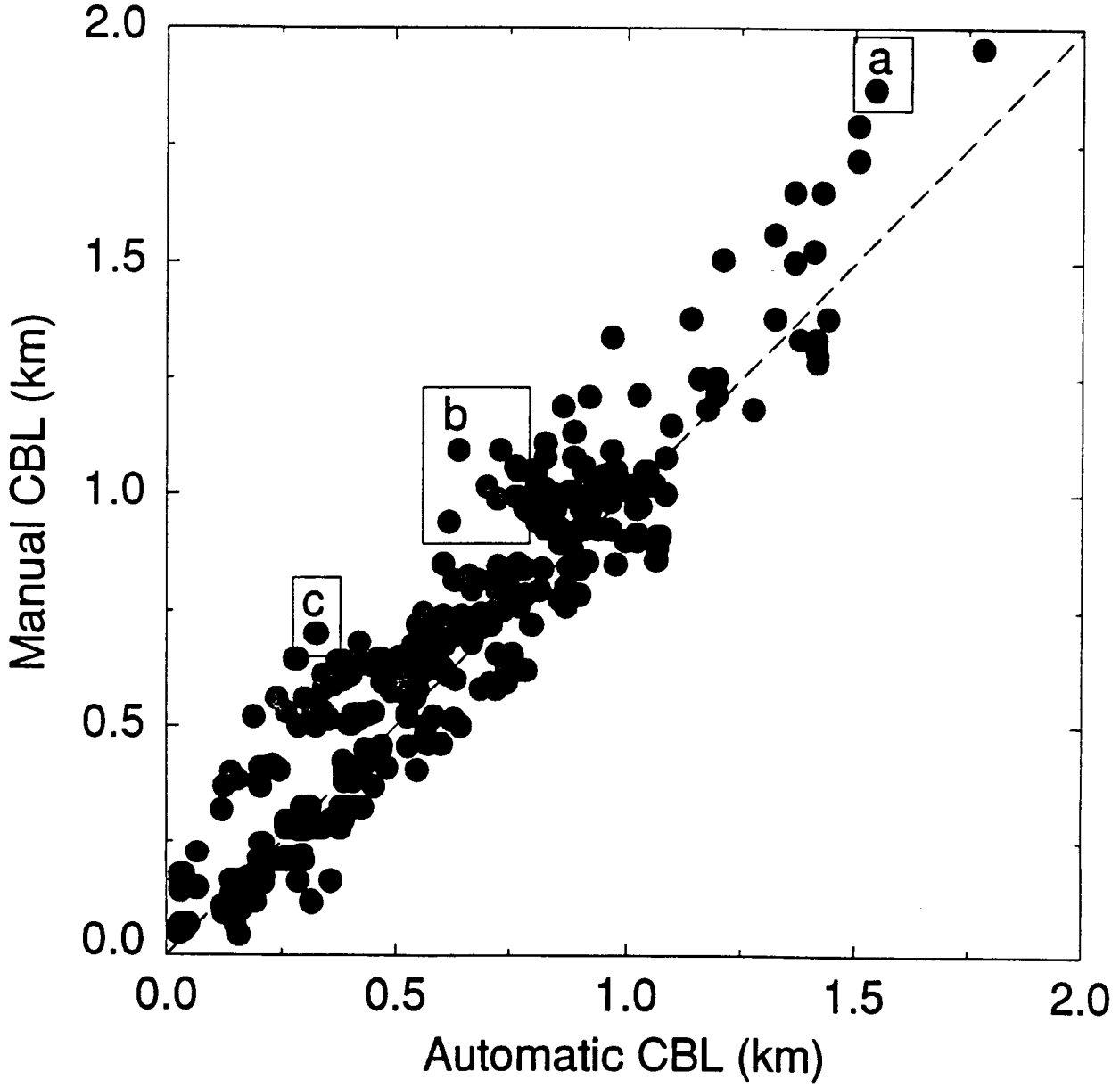

Fig. 5.

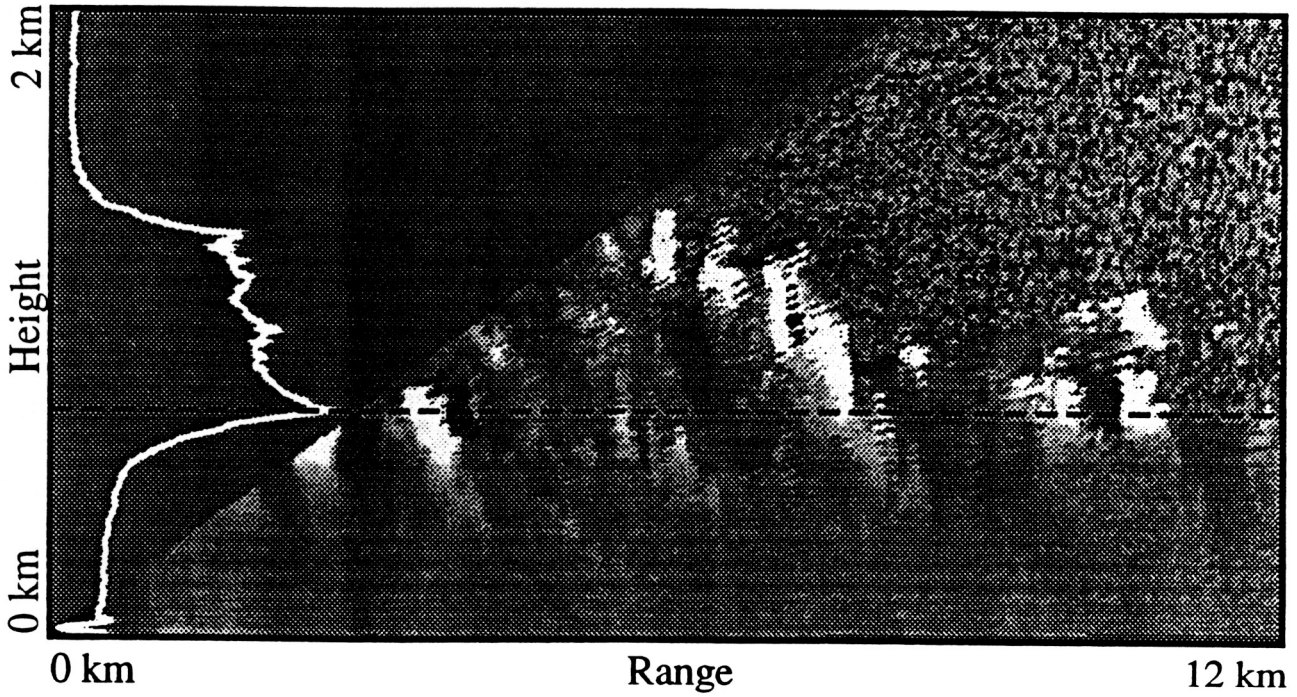

Fig. 6.

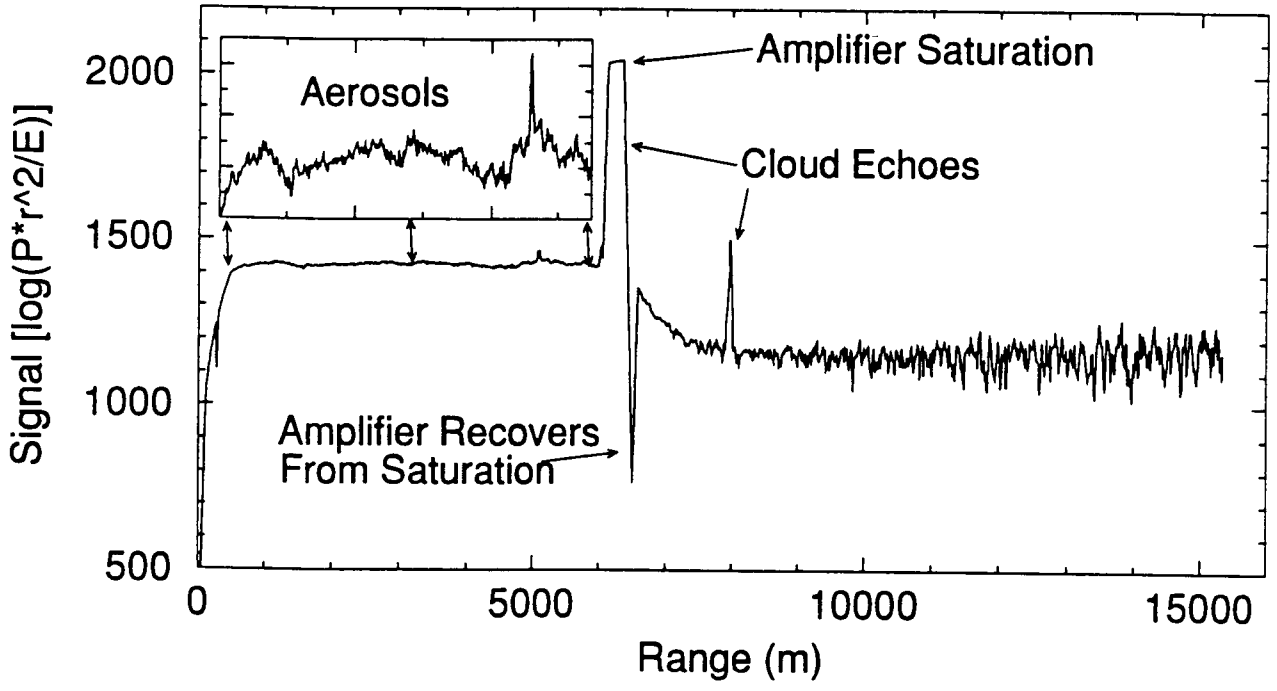
Signal [log(P*r^2/E)]
2000
1500
1000
500
0
5000
10000
15000
Range (m)
Aerosols
Amplifier Saturation
Cloud Echoes
Amplifier Recovers
From Saturation

Fig. 7.

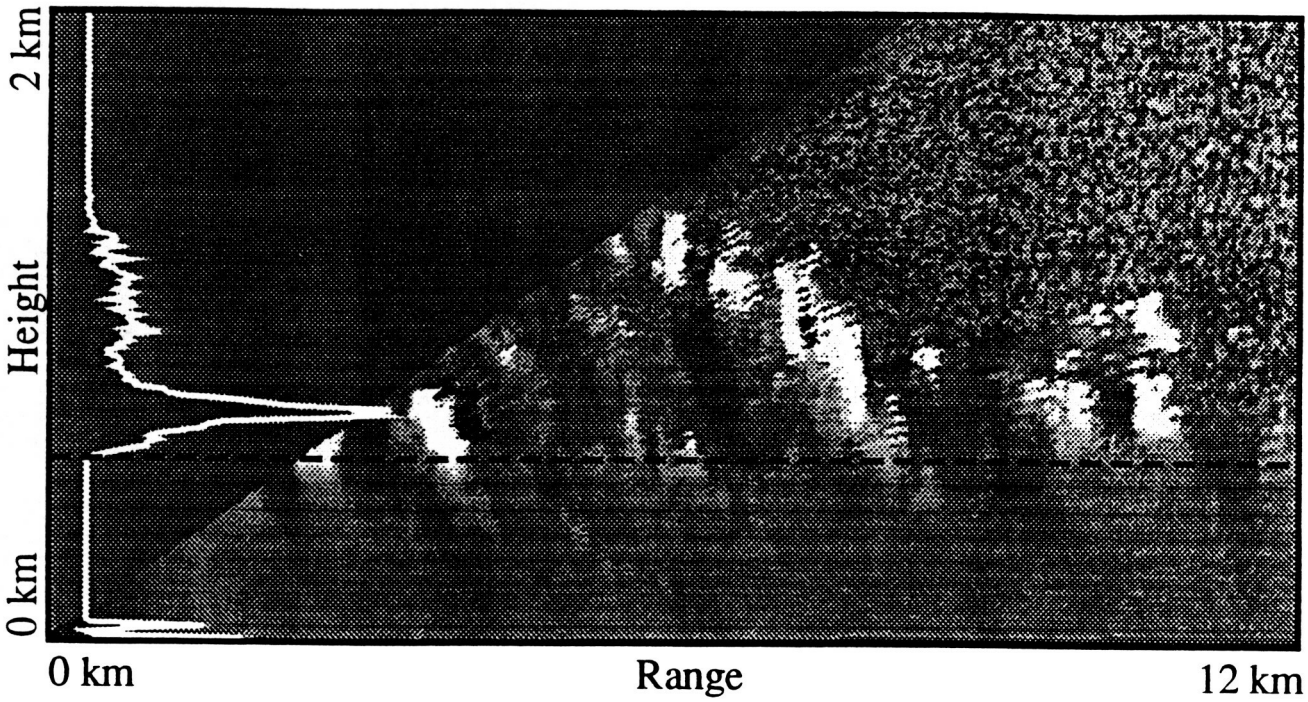

Fig. 8.

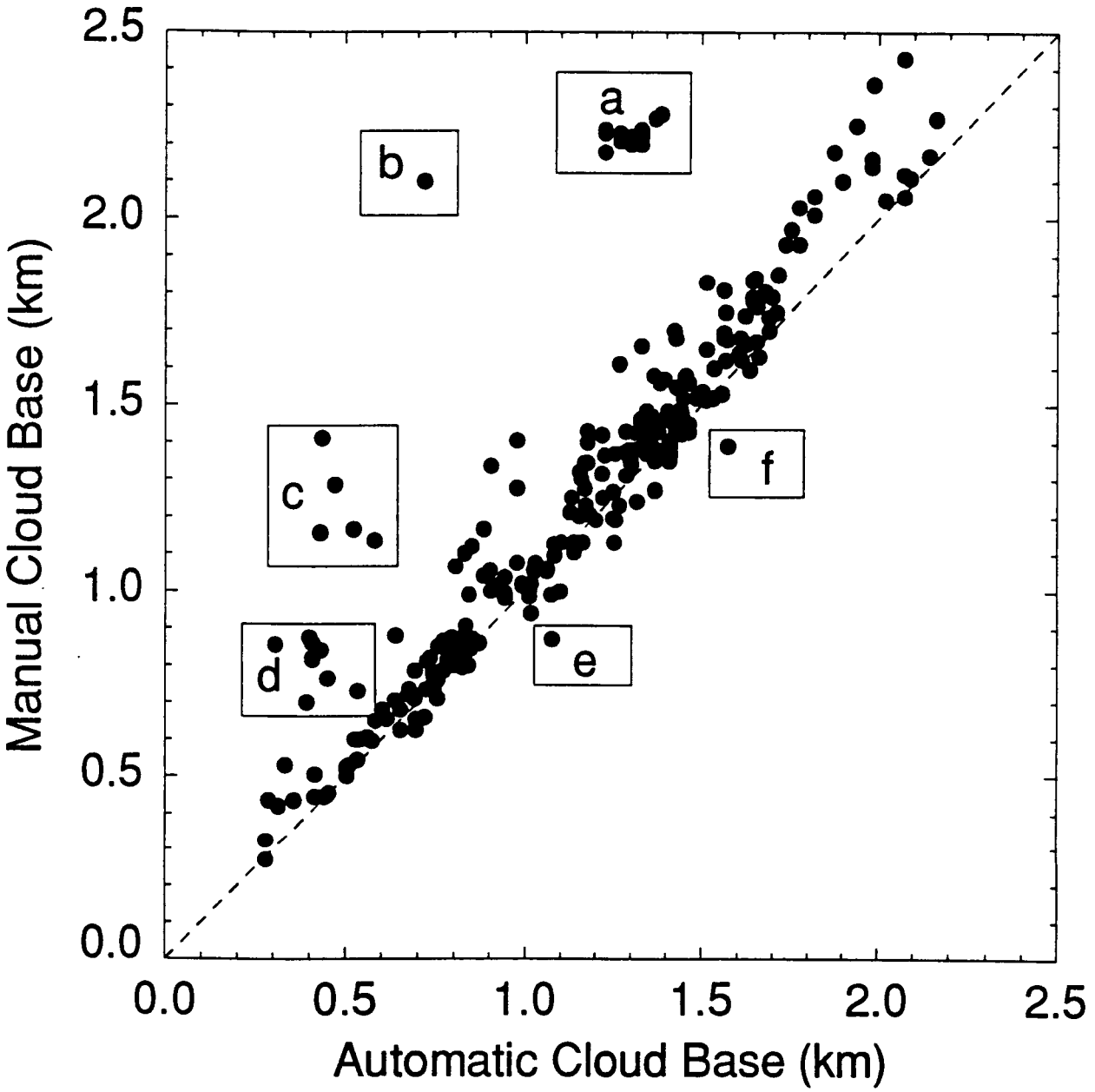
Manual Cloud Base (km)
Automatic Cloud Base (km)
0.0
0.5
1.0
1.5
2.0
2.5
a
b
c
d
e
f

Fig. 9.

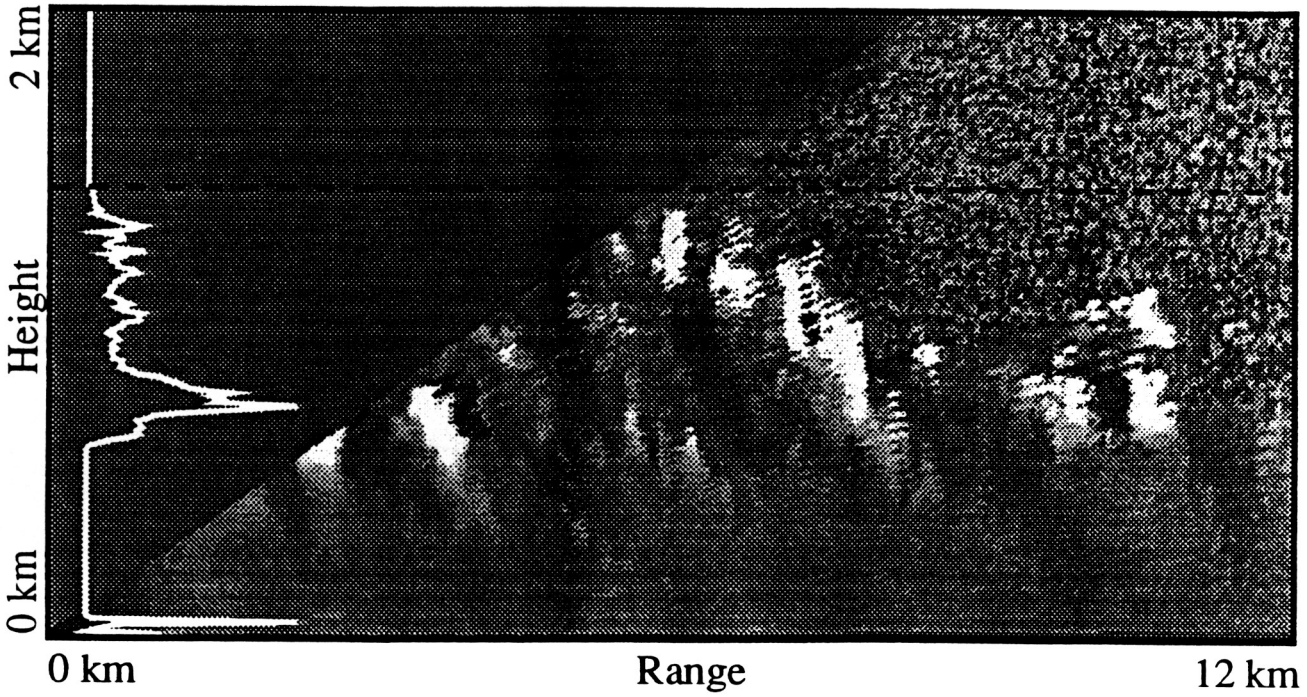

Fig. 10.

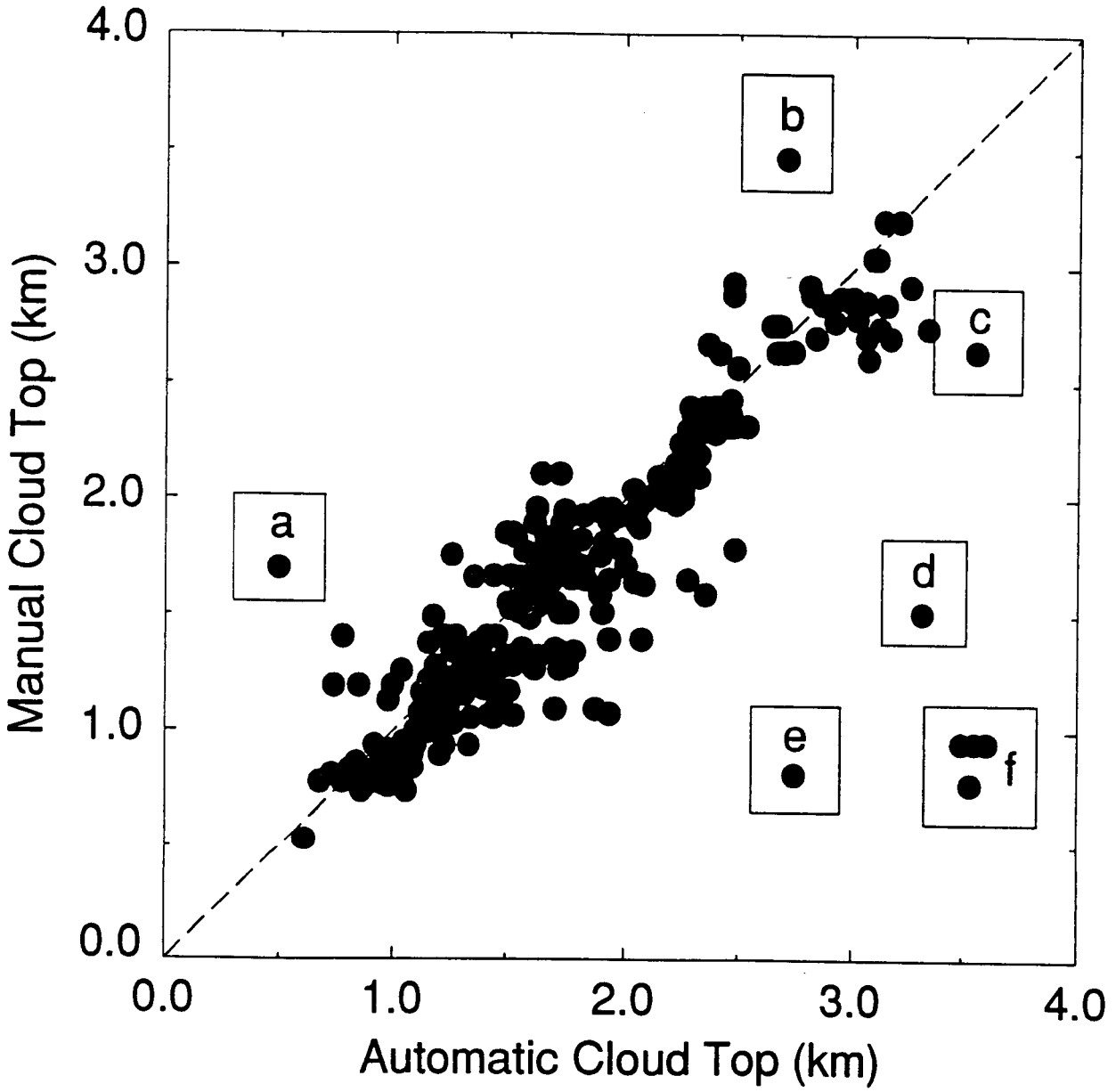
4.0
3.0
2.0
1.0
0.0
Manual Cloud Top (km)
0.0
1.0
2.0
3.0
4.0
Automatic Cloud Top (km)
a
b
c
d
e
f

Fig. 11.

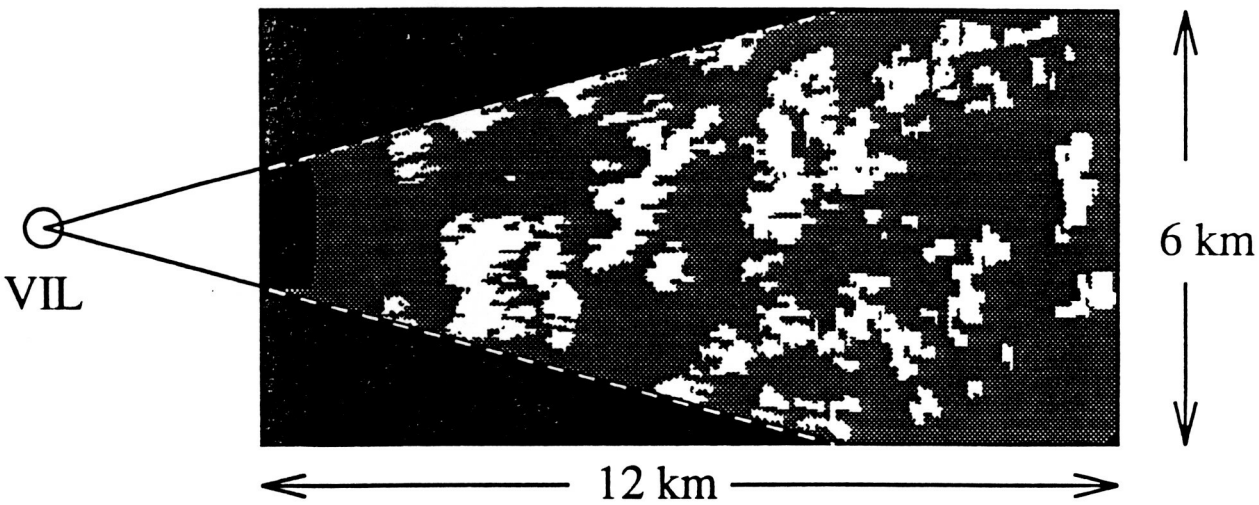

Fig. 12.

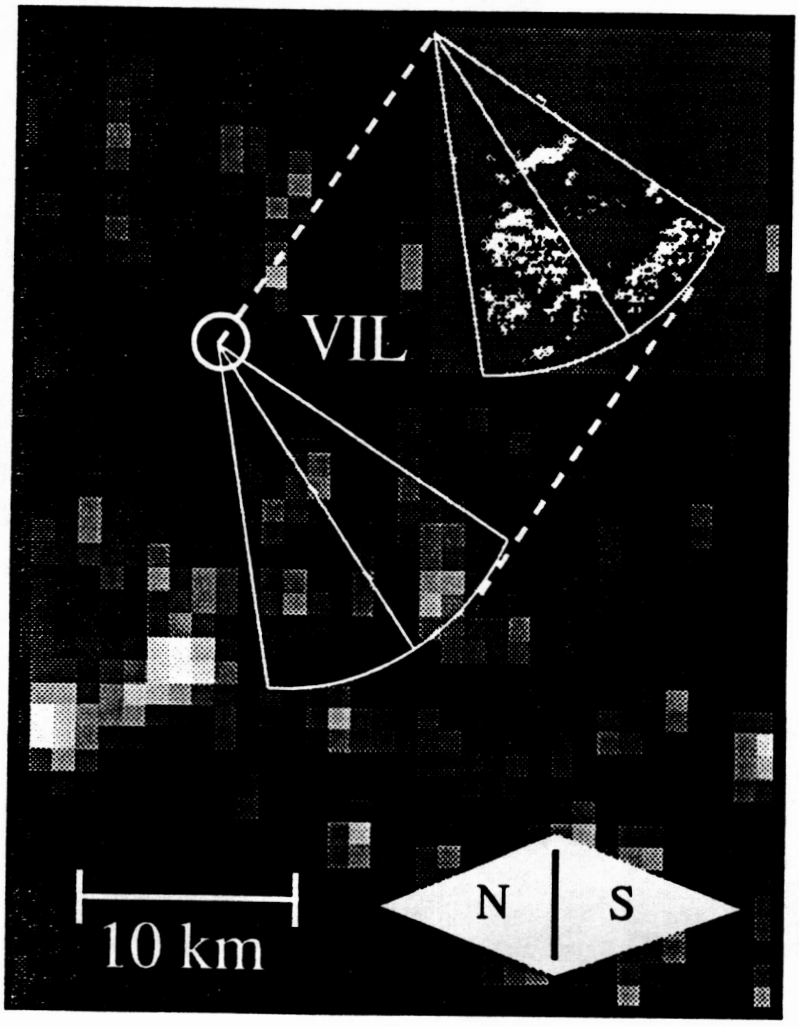

Fig. 13.

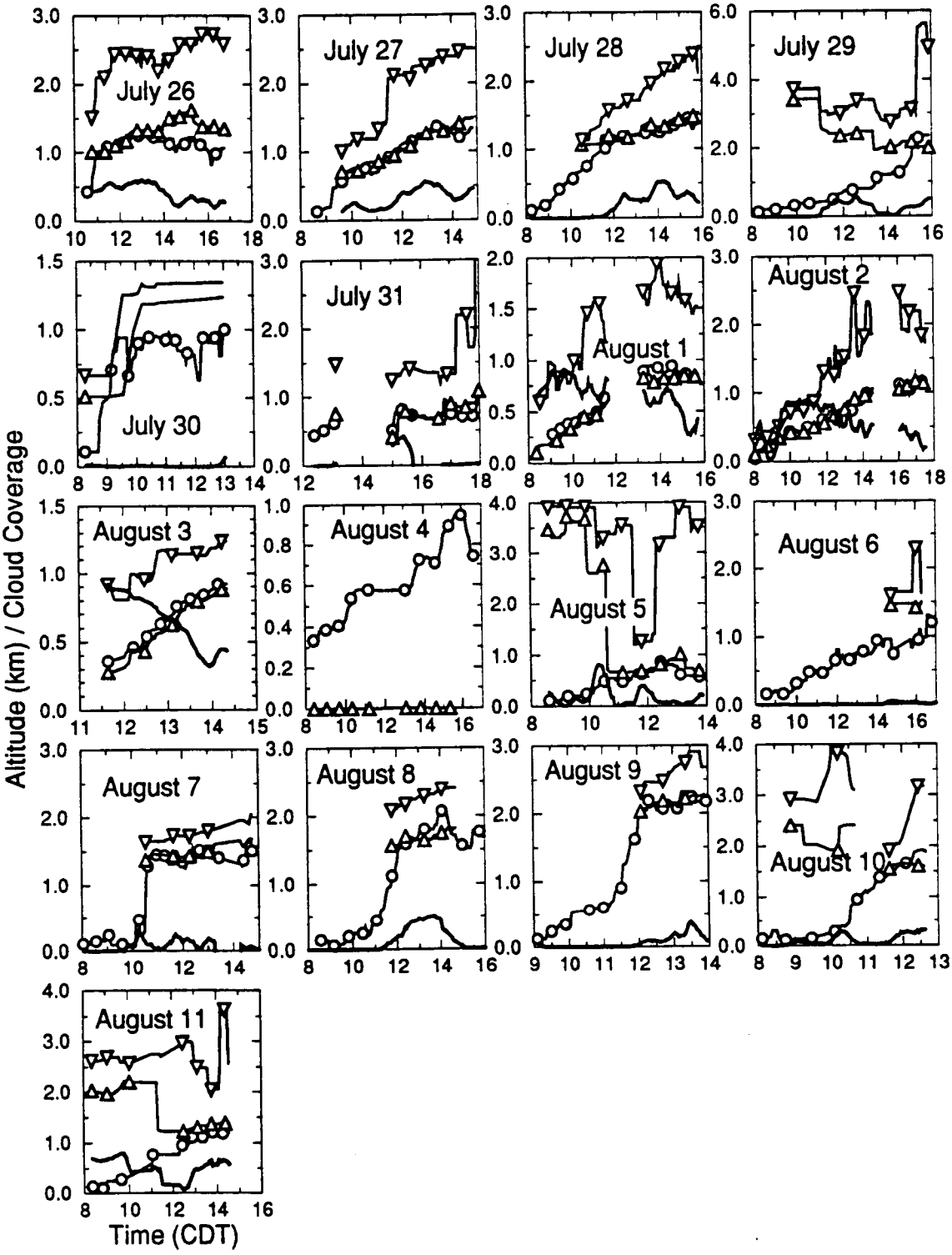
July 26
July 27
July 28
July 29
July 30
July 31
August 1
August 2
August 3
August 4
August 5
August 6
August 7
August 8
August 9
August 10
August 11
Altitude (km) / Cloud Coverage
Time (CDT)

Fig. 14.

An accuracy analysis of the wind profiles calculated from Volume Imaging Lidar data

Antti K. Piironen and Edwin W. Eloranta

University of Wisconsin, Madison

Department of Atmospheric and Oceanic Sciences

1225 West Dayton Street

Madison, WI 53706

email: antti@vil.meteor.wisc.edu eloranta@lidar.meteor.wisc.edu

(Received

Abstract

This paper presents a study of the vertical profiles of horizontal mean winds calculated from data obtained with the University of Wisconsin Volume Imaging Lidar (VIL) during the 1989 FIFE program. Wind profiles are determined from cross correlation functions between subsequent Constant Altitude Plan Position Indicator planes calculated from volume scans of the convective boundary layer. An objective technique to identify unreliable measurements is developed. An error analysis based on determining the errors due to random noise in data is performed. The VIL wind profiles are compared with radiosonde, aircraft-based, and ground-based measurements. Based on internal consistency tests, we estimate that in the convective boundary layer the hourly averaged VIL wind estimates which have passed the reliability analysis, have root-mean-square errors 0.03–0.1 ms^{-1} in speed and 0.4–2.0° in direction.

1. Introduction

Mesoscale wind profiles are needed in a wide variety of meteorological applications. Wind profiles are traditionally measured using methods which provide wind speed and direction at certain points. However, point measurements in the convective boundary layer do not generally provide representative area averaged wind estimates. The point measurements can be biased, for example, by large eddies, roll vortices, and topography. The averaging time cannot be extended to dampen temporal fluctuations without producing errors due to the changing value of the mean wind. Therefore, representative area average measurements are required.

The three-dimensional aerosol detection capability of the University of Wisconsin Volume Imaging Lidar (VIL) [*Eloranta and Forrest*, 1992] along with correlation techniques provide vertical profiles of horizontal area average winds [*Schols and Eloranta*, 1992]. The volume scans of the VIL show the three-dimensional evolution of the aerosol distribution in a 15 km long, 40° wide, and 9–15° high sector consisting of ~5500 lidar backscatter profiles with a 15 meter range resolution. A three-minute scan time ensures that most of the aerosol structures appearing in a volume scan are coherent in the next scan. This paper studies the accuracy of wind profiles calculated from the data obtained with the VIL during the 1989 FIFE (First ISLSCP (International Satellite Land Surface Climatology Project) Field Experiment) program [*Sellers et al.*, 1992] between July 26 and August 11. The original wind profiling algorithm introduced by Schols and Eloranta (1992) is refined.

The wind profiling method is based on determining the movements of aerosol structures from subsequent Constant Altitude Plan Position Indicator (CAPPI) scans of the VIL. The CAPPI scans represent two-dimensional horizontal maps of the convective boundary layer (CBL) aerosols at different altitudes. The aerosol movements are determined by

505-65-3389

calculating spatial two-dimensional cross correlation functions (CCF) between subsequent CAPPI scans at each altitude. The position of the CCF maximum peak indicates the mean wind speed and direction average over $\sim$ 70 km^2 VIL scanning area.

At the top of the convective boundary layer, where the backscatter signals have a good contrast between aerosol structures and clearer air, the wind estimation can be done directly from the two-dimensional cross correlation function between two subsequent CAPPI scans. Above the top of the CBL and near the surface, however, the situation is more complicated. Above the top, lidar signal extinction on clouds causes correlations between shadowed portions of the signal. Near the ground, aerosol plumes anchored to particular locations cause stationary aerosol structures which lead to strong zero space lag correlations. Intense structures appearing only on one CAPPI may cause strong random correlations. These conditions prompt a need for preprocessing the backscatter signal and CAPPI scans before calculating the cross correlation functions.

To eliminate the effects of variable atmospheric attenuation, scan angle dependent background signals, and shot to shot variations in energy normalization, the lidar backscatter profiles are median high pass filtered. Signals above optically thick clouds are not used to prevent correlations between cloud shadows. Since wind moves aerosol structures during scanning, the position of each lidar backscatter profile is shifted upwind to provide aerosol information at the time of the first shot in the volume scan. Previous hourly averaged results are used as a priori information and the wind profiling procedure is iterated if the subsequent results differ substantially.

A temporal median of five subsequent CAPPI scans is subtracted from each CAPPI scan to prevent interference from stationary structures. The CAPPI scans are then histogram equalized [*Hall*, 1974] to prevent any single intense aerosol structure from dominating the cross correlation function. In the earlier study [*Schols and Eloranta*, 1992], the histogram equalization was performed with 64 intensity classes. Because too few classes

will blur aerosol structures and widen cross correlation functions, the number of classes is limited only by the digital levels of the data in this study. Finally, the average intensities are subtracted from the CAPPI scans to reduce zero space lag correlations. Figure 1 represents an example of a filtered CAPPI scan, which is ready for correlation calculations.

A two-dimensional cross correlation function between two subsequent CAPPI scans at the same altitude is calculated using the Fast Fourier Transformation with zero padded data to prevent end effects [*Press et al.*, 1988]. The cross correlation function is divided by the covariance of the corresponding CAPPI scans providing a correctly weighted CCF for the time-average calculations. The wind estimate is determined from the maximum correlation peak in three steps:

1) locating the global maximum correlation peak
2) determining the local maximum of the global maximum peak
3) calculating the wind speed and direction

The global maximum correlation peak was determined from a spatially low pass filtered correlation function in the earlier study [*Schols and Eloranta*, 1992]. The optimal length for this filter, however, depends on the noise level and aerosol structure formations, which both vary on different atmospheric conditions. To reduce time and space dependent parameters in the analysis, this study uses the following approach to locate the maximum correlation peak. First, the global maximum correlation amplitude is found. All regions with amplitude greater than $1/e$ of the global maximum correlation amplitude are located. The mass m of each region is calculated by summing all correlation amplitudes inside the region. The region with greatest mass m_{max} represents the global maximum correlation peak. The masses of the regions are also used in the reliability analysis (see section 2.).

The local maximum of the global maximum correlation peak position is determined by least-squares-fitting a two-dimensional polynomial function to a 5×5 domain around

the highest point of the global maximum correlation peak. The maximum point of the fitted function is used as the maximum peak position gaining sub-pixel resolution. Sub-pixel resolution is achievable since aerosol structure formations along with approximate Gaussian turbulence lead to smooth-peaked cross correlation functions. The fitted function is expressed as

$$f(x,y) = a_0 + a_1 x + a_2 y + a_3 x^2 + a_4 y^2 + a_5 xy \quad , \tag{1}$$

where x and y denote coordinates in correlation plane and a_i's are model parameters. The model parameters $(a_0, a_1, \ldots, a_5)$ are solved from a linear equation group

$$\begin{pmatrix} 1 & x_1 & y_1 & x_1^2 & y_1^2 & x_1 y_1 \\ 1 & x_2 & y_2 & x_2^2 & y_2^2 & x_2 y_2 \\ \vdots & \vdots & \vdots & \vdots & \vdots & \vdots \\ 1 & x_{25} & y_{25} & x_{25}^2 & y_{25}^2 & x_{25} y_{25} \end{pmatrix} \begin{pmatrix} a_0 \\ a_1 \\ a_2 \\ a_3 \\ a_4 \\ a_5 \end{pmatrix} = \begin{pmatrix} ccf(x_1, y_1) \\ ccf(x_2, y_2) \\ \vdots \\ ccf(x_{25}, y_{25}) \end{pmatrix} \quad , \tag{2}$$

where (x_i, y_i) are the coordinates of the fit point i and $ccf(x,y)$ is the cross correlation function amplitude at point (x,y). The 25×6 kernel matrix is marked as $\mathbf{G}$, the model parameter vector as $\mathbf{a}$, and the vector of cross correlation function amplitudes as $\mathbf{d}$. The least-squares solution of the parameter vector $\mathbf{a}$ is [*Menke*, 1984]

$$\mathbf{a}_{est} = \left[\mathbf{G}^T \mathbf{G}\right]^{-1} \mathbf{G}^T \mathbf{d} \quad , \tag{3}$$

where $\mathbf{G}^T$ denotes the transpose of matrix $\mathbf{G}$ and $[\ \ ]^{-1}$ the inverse of a square matrix. After determining the model parameters, the position of the maximum point (x_{max}, y_{max}) of function $f(x,y)$ is determined by solving equations

$$\frac{\partial f(x,y)}{\partial x} = 0 \tag{4}$$

$$\frac{\partial f(x,y)}{\partial y} = 0 \tag{5}$$

leading to

$$x_{max} = \frac{2a_4a_1 - a_5a_2}{a_5^2 - 4a_3a_4} \tag{6}$$

$$y_{max} = \frac{2a_3a_2 - a_5a_1}{a_5^2 - 4a_3a_4} \quad . \tag{7}$$

Figure 2 represents an example of the fit to the maximum CCF peak. The top of the peak is wide and the points near the local maximum have almost the same intensity. The maximum point of the fitted function interpolates between pixels gaining sub-pixel resolution. The polynomial fit is less sensitive to noise than the bicubic spline fit used in the earlier studies [*Schols and Eloranta*, 1992]; the least-squares fit slightly filters the peak, while the bicubic spline may have noise induced oscillations near the maximum peak.

The wind speed and direction are determined from the position of the maximum peak of the fitted polynomial representing mean movements of the aerosol structures between the CAPPI scans. The wind speed u and direction θ are given by

$$u = \frac{\sqrt{x_{max}^2 + y_{max}^2}}{\tau} \tag{8}$$

$$\cos\theta = \frac{-x_{max}}{\sqrt{x_{max}^2 + y_{max}^2}} \tag{9}$$

$$\sin\theta = \frac{-y_{max}}{\sqrt{x_{max}^2 + y_{max}^2}} \quad . \tag{10}$$

where τ is the time separation between subsequent volume scans.

The most effective way to calculate time-averaged wind estimates is to average cross correlation functions together, since random correlations vanish in the averaging process providing a less noisy correlation function to the wind calculation. Even a weak aerosol correlation peak dominates the cross correlation function after an appropriate averaging time. Figure 3 compares the results of two different averaging methods. The first method averages subsequent correlation functions leading to a consistent wind profile. The second method calculates wind estimates from the cross correlation functions and then averages the wind estimates. Some of the estimates of the second method have large fluctuations from adjacent points due to a few uncertain results with large errors which were averaged together with reliable results. All results presented in this study are generated by averaging correlation functions.

The main purpose of this study is to evaluate the accuracy and reliability of the wind measurements calculated from the data obtained with the VIL during the 1989 FIFE program. A method is developed for estimating the root-mean-square (RMS) errors in determining the wind speed and direction. If turbulent mixing changes aerosol structures between CAPPI scans substantially or the signal is dominated by noise, the strength of the aerosol structure correlations may decrease to the level of random noise correlations. This causes uncertain wind estimates with large errors. This study incorporates an objective method to determine the probability that the chosen correlation peak is caused by aerosol movements between two subsequent CAPPI scans instead of random signal fluctuations. This analysis is employed in the accuracy calculations to reject results which are likely to contain large errors. Reliable wind results are then compared with measurements made with an aircraft based instrument, radiosondes, and automatic weather stations. Even if these traditional measurements had no noise, they may not represent well area average winds due to bias by large scale eddies and roll vortices. Therefore, the method for esti-

mating the RMS errors of the wind results is tested comparing the error estimates with the internal consistency of the VIL results. The 1989 FIFE program produced a large number of VIL wind profiles which are entered into the FIFE database [*Strebel et al.*, 1990]. Only examples of them are presented here.

2. Reliability Estimation

The major problem in the wind profiling method is the possibility that the selected maximum correlation peak results from correlations of random noise instead of aerosol structures. Normally, a cross correlation function between two CAPPI scans is dominated by a single peak. Sometimes, however, random noise fluctuations along with weak aerosol structure coherence between subsequent CAPPI scans lead to random correlation peaks, which are stronger than the aerosol correlation peak. This prompts a need to identify the spurious results, which are likely to be calculated from random correlation peaks.

In this study, an objective method is developed to distinguish between reliable and unreliable wind estimates by indicating the probability that the chosen maximum correlation peak represents the mean aerosol movements. Statistical studies indicated the intensity of wind estimate fluctuations from the hourly mean values correlated with the CCF maximum peak strength compared to all substantial peaks in the cross correlation function. Probability P_{max} that the global maximum correlation peak represents the mean wind is given by

$$P_{max} = \frac{m_{max}}{\sum_{i=1}^{I} m_i} \quad , \tag{11}$$

where m_{max} is the mass of the global maximum correlation peak and m_i is the mass of the correlation peak i. The masses are calculated by summing the intensities around

the peak with amplitude higher than $1/e$ of the global maximum correlation amplitude. P_{max} indicates the probability that the strongest correlation function peak is caused by the mean wind. If there is only one correlation peak, then the P_{max} is 1. If there are numerous similar correlation peaks, P_{max} converges to zero.

Figure 4 shows scatter plots for P_{max} vs. wind speed and direction for quarter-hourly averaged results on July 27, 1989. Most of the results have $P_{max} = 1$ and are within the natural wind deviation of that day; the results with lower P_{max} are more widely spread. In general, $P_{max} > 0.5$ provide mostly good results, while $P_{max} < 0.5$ are poor.

The fraction of reliable VIL wind estimates as a function of averaging time interval and P_{max} is shown in figure 5. Averaging the cross correlation functions effectively increases the fraction of reliable results. Even a fifteen-minute averaging more than doubles the ratio of good measurements to all measurements. The recovery ratio of hourly averaged winds in the boundary layer is about 76%. Most of the measurements with P_{max} between 0.9 and 1.0 are still consistent.

3. Error Estimation

The errors of the wind speed and direction are estimated by calculating the change in the maximum correlation peak position (x_{max}, y_{max}) when the CCF has some additional noise. In this section, we determine the error of the fit parameters and use it to estimate error in position of the maximum point of the fitted function. The expected root-mean-square error in wind speed and direction are derived from the error in the position of the maximum correlation peak.

Assuming the noise in the CCF plane is uncorrelated from point to point and the variance of the noise is σ_n^2, the covariance matrix of the estimated model parameters $\mathbf{a}_{est}$ solved from equation (3) is given by

$$[\text{cov } \mathbf{a}_{est}] = \sigma_n^2 \left[\mathbf{G}^T\mathbf{G}\right]^{-1} \equiv \begin{pmatrix} c_{a0a0} & c_{a0a1} & c_{a0a2} & \cdots & c_{a0a5} \\ c_{a1a0} & c_{a1a1} & c_{a1a2} & \cdots & c_{a1a5} \\ \vdots & \vdots & \vdots & \ddots & \vdots \\ c_{a5a0} & c_{a5a1} & c_{a5a2} & \cdots & c_{a5a5} \end{pmatrix} . \qquad (12)$$

Since the histogram equalization is a highly nonlinear operation, we have no information about the spatial distribution of noise. We have assumed that the noise is uncorrelated with a constant variance to make analytical formulation of the noise effects possible; however, we cannot determine the accuracy of this approximation. Although, after histogram equalization, the uniform distribution of the signal and noise superposition suggests that the noise in the CCF is probably also uniformly distributed.

The noise variance σ_n^2 of the CCF is estimated from a noise plane. The noise plane is made from the CCF by reducing the aerosol correlation portion of the CCF using the

following procedure. First, an average of three vertically adjacent CCF planes are subtracted from the CCF. Then, the global maximum correlation peak is masked by rejecting all pixels inside the maximum correlation peaks $1/e$-region. Finally, noise variance σ_n^2 is calculated from the masked CCF.

The mean-squared error in determining the maximum peak position is given by

$$\sigma_x^2 = \sum_{i=1}^{5} \left(\frac{\partial x_{max}}{\partial a_i} \right)^2 \sigma_{a_i}^2 = \frac{4{a_4}^2 \sigma_{a_1}^2}{\left({a_5}^2 - 4a_3a_4\right)^2} + \frac{{a_5}^2 \sigma_{a_2}^2}{\left({a_5}^2 - 4a_3a_4\right)^2} + \left(\frac{8a_1{a_4}^2 - 4a_2a_4a_5}{\left({a_5}^2 - 4a_3a_4\right)^2} \right)^2 \sigma_{a_3}^2 + \left(\frac{2a_1a_5^2 - 4a_2a_3a_5}{\left({a_5}^2 - 4a_3a_4\right)^2} \right)^2 \sigma_{a_4}^2 + \left(\frac{a_2{a_5}^2 - 4a_1a_4a_5 + 4a_2a_3a_4}{\left({a_5}^2 - 4a_3a_4\right)^2} \right)^2 \sigma_{a_5}^2 \tag{13}$$

and

$$\sigma_y^2 = \sum_{i=1}^{5} \left(\frac{\partial y_{max}}{\partial a_i} \right)^2 \sigma_{a_i}^2 = \frac{{a_5}^2 \sigma_{a_1}^2}{\left({a_5}^2 - 4a_3a_4\right)^2} + \frac{4{a_3}^2 \sigma_{a_2}^2}{\left({a_5}^2 - 4a_3a_4\right)^2} + \left(\frac{2a_2a_5^2 - 4a_1a_4a_5}{\left({a_5}^2 - 4a_3a_4\right)^2} \right)^2 \sigma_{a_3}^2 + \left(\frac{8a_2{a_3}^2 - 4a_1a_3a_5}{\left({a_5}^2 - 4a_3a_4\right)^2} \right)^2 \sigma_{a_4}^2 + \left(\frac{a_1{a_5}^2 - 4a_2a_3a_5 + 4a_1a_3a_4}{\left({a_5}^2 - 4a_3a_4\right)^2} \right)^2 \sigma_{a_5}^2 \quad , \tag{14}$$

where $\sigma_{a_i}^2$'s are error variances of model parameters a_i estimated from the model parameter covariance matrix [cov $\mathbf{a}_{est}$] as

$$\sigma_{a_i}^2 = \sum_{j=0}^{5} \left| c_{a_i a_j} \right| \quad . \tag{15}$$

Finally, the root-mean-square errors σ_u and σ_θ for wind speed and direction estimates, respectively, are determined from

$$\sigma_u = \sqrt{\left(\frac{\partial u}{\partial x_{max}}\right)^2 \sigma_x^2 + \left(\frac{\partial u}{\partial y_{max}}\right)^2 \sigma_y^2} = \frac{1}{\tau}\sqrt{\frac{\sigma_x^2 x_{max}^2 + \sigma_y^2 y_{max}^2}{x_{max}^2 + y_{max}^2}} \tag{16}$$

$$\sigma_\theta = \sqrt{\left(\frac{\partial \theta}{\partial x_{max}}\right)^2 \sigma_x^2 + \left(\frac{\partial \theta}{\partial y_{max}}\right)^2 \sigma_y^2} = \sqrt{\frac{\sigma_x^2 y_{max}^2 + \sigma_y^2 x_{max}^2}{\left(x_{max}^2 + y_{max}^2\right)^2}} \quad . \tag{17}$$

The direction error is expressed in radians. These equations represent root-mean-square errors of the mean wind estimate due to position error of the maximum correlation peak from a noisy CCF. The error estimates represent the lower bounds of the error, since the previous error analysis does not take into account possible errors due to systematic deformation of aerosol structures between scans. Furthermore, the error variance may be poorly estimated due to nonlinear effects in the histogram equalization of the CAPPI scans.

4. Results and Discussion

4.1. Reliability analysis

This section summarizes the results of the reliability analysis performed on all VIL wind profiles from the 1989 FIFE program. Figure 6 shows probability P_{max} of quarter-hourly averaged wind measurements as a function of time and altitude on July 26, 1989. The contours show the wind speed increasing from 5 ms^{-1} to 8.5 ms^{-1} over the period. Even using 0.2 ms^{-1} contour spacing, the wind profiles are smooth and small details are visible. The measurements have good internal consistency, except for some small disturbances with a smaller P_{max}. The results are most reliable in the convective boundary layer. Above the convective boundary layer there are sometimes not enough aerosol structures

for correlation analysis, leading to less reliability. Turbulent mixing in the late afternoon sometimes produces uniform aerosol distribution that leads to less reliable wind estimates, which also are present in the Figure 6. In the convective boundary layer, randomly located decreased reliabilities are generally due to the breaks in the data record. This happened on July 26 several times after 14:00 CDT. These breaks are generally due to system adjustments or safety-shutoff of the laser output beam when an aircraft was flying in the field of view.

4.2. Comparisons with flight-leg averaged and point measurements

To verify consistency between the VIL wind profiles and traditional measurements, the VIL results are compared with:

1) data from eight National Center for Atmospheric Studies Portable Automatic Mesonet stations (PAMS) [*Sellers et al.*, 1992] that provide half-hour averaged ground-based measurements
2) radiosonde profiles measured by a team from Cornell University directed by Prof W. Brutsaert [*Sellers et al.*, 1992]
3) aircraft-based Canadian National Aeronautical Establishments Twin Otter [*MacPherson*, 1988] flight-leg averaged measurements

All comparison data is retrieved from the FIFE database [*Strebel et al.*, 1990]. Figure 7 provides an overview of the site locations and flight patterns on July 27, 1989. All measurements are done within 20 km distance from each other. All weather stations are closer than 10 km from the VIL site and an average 20 m lower than the VIL site.

Figure 8 compares hourly averaged VIL wind profiles, radiosonde profiles, aircraft-based measurements, and hourly averaged surface measurements on July 27, 1989, from 11:00 to 12:00 CDT. The cloud base altitude is $\sim$ 900 m; the cloud top altitude is $\sim$ 1500 m;

cloud coverage is $\sim$ 35%. The VIL wind profiles vary smoothly over the mixed layer and the cloud layer. The P_{max} indicates less reliability above the cloud top where the aerosol distribution is weaker, although the method still gives some consistent results. As expected, wind speeds decrease slightly towards the ground showing the effects of friction. The wind shows little directional shear in the convective boundary layer.

The surface measurements show averages of eight weather stations over one hour period. Surface friction causes the averaged ground winds to be slightly slower and backed compared to the low level VIL profiles. For safety reasons, the VIL did not scan at the ground level causing a vertical gap between the VIL and PAMS measurements. The wind measurements vary $\sim$ 1 ms^{-1} and 20° between stations due to topographic differences. Evidently, averaging several ground measurements together still does not achieve the stability of area average wind measurements.

The discrepancy between radiosonde profiles and area-averaged VIL profiles is expected, since the radiosonde is sensitive to local wind variations due to turbulence. The radiosonde profiles suggest fairly strong directional wind shear at the top of the mixed layer and near to ground, while the VIL and aircraft measurements do not. Small averaging time interval of the radiosonde makes it sensitive to local wind variations. The area-averaged VIL wind profiles and flight-leg averaged aircraft wind measurements are more representative in a mesoscale sense than the radiosonde wind profiles.

The aircraft flight-path averaged wind measurements agree with the VIL profiles. The largest deviations between aircraft-based measurements and VIL profiles occur at the mixed layer top and near the ground. This is probably due to horizontal roll vortices, which are detected as trends in aircraft wind calculations. These eddies produce mostly vertical air motions in the middle of the mixed layer, where the VIL and aircraft measurements coincide better.

Figure 9 shows the correlation between VIL results with $P_{max} = 1$ and simultaneous aircraft-based measurements. A least-squares-fitted line through the data points has a slope of 0.98±0.2 and an offset of 0.17±0.12 ms^{-1} for wind speed, and a slope of 1.01±0.01 and an offset of 1.7°±1.9° for direction. The root-mean-square deviations between results are $\sim$ 1.0 ms^{-1} in speed and $\sim$ 12° in direction. The aircraft flights on July 28, August 2, and August 3, were directed through the middle of the VIL scan pattern. Thus, the sampling of the aircraft and lidar were more closely matched. These results show smaller deviations from the mean value in the VIL observations than in adjacent aircraft measurements. This suggests that the VIL results are statistically more stable than the aircraft measurements, as a result of area averaging.

4.3. Accuracy analysis

Natural wind deviations in point and line-averaged measurements dominates the differences between these measurements and the VIL observations. Therefore, the point and line-averaged measurements are not used as the reference for accuracy analysis of the wind profiling method. Calculated error estimates of the VIL wind profiles are compared to the local consistency of the measurements. The local consistency is calculated for each wind measurement by subtracting an average of its vertically adjacent wind measurements. In linear wind shear conditions, the local consistency represents measurement inaccuracy. Data from July 26, 1989, is selected (see Figure 10) for accuracy calculations, since the wind shear is more linear than on any other day in the 1989 FIFE program.

Figure 11 compares the local root-mean-square deviations of the results from the averages of vertically adjacent results and calculated RMS error estimates for hourly averaged wind profiles on July 26, 1989. The calculated error estimates represent RMS errors in wind determination due to noise in the CCF, which is dominating error source after we

have rejected the wind estimates with P_{max} less than 1. Therefore, they are generally smaller than the local deviations, which are due to both the natural wind deviation and method inaccuracy. In the convective boundary layer (below 1400 m) the RMS errors in hourly averaged wind estimates are less than 0.14 ms^{-1} in speed and 2.1° in direction. Part of the local variation is due to real wind fluctuations. Thus, it provides a conservative estimate of the wind fluctuations.

The calculated profiles show minimum RMS errors at 800 m: the contrast between scattering from aerosol structures and mixed air is very good just below the CBL top, since the clear air penetrating down to the CBL is not yet mixed with the boundary layer aerosols. Closer to the ground, more intense mixing smears the aerosol structures decreasing the signal to noise ratio of the CCF. Above the convective boundary layer, clouds block the signal decreasing the signal to noise ratio.

Figure 12 shows RMS-error estimates of wind measurements as functions of the averaging time and the normalized altitude from July 26 to July 31, 1989. Error estimates are linearly interpolated into altitudes normalized by the convective boundary layer mean depths and averaged over time. In the CBL, the error estimates are almost constant with altitude, but above the CBL, they grow almost exponentially. In the convective boundary layer, the RMS errors are in average less than 0.2 ms^{-1} in speed and 3.0° in direction. In the middle of the convective boundary layer, where aerosol structures have good contrast against the background, the RMS-errors are in order of 0.03–0.05 ms^{-1} in speed and 0.3–0.8° in direction. Above the CBL, the RMS-errors vary between 0.1–3.0 ms^{-1} in speed and 1.0–30° in direction, since the correlations get poorer due to aerosol structures diminishing with altitude and clouds blocking the signal. The RMS-errors decrease as the averaging time interval increases, since the averaging of the CCFs reduces random correlations.

5. Conclusions

This study provides enhancements to the original wind profiling algorithm [*Schols and Eloranta*, 1992]. A method is developed to identify correlation peaks, which are likely to be caused by random correlations. The analysis performed for the VIL wind profiles from the 1989 FIFE data indicates that by the most restrictive reliability definition (i.e. P_{max}=1), ~76% of hourly averaged wind estimates in the convective boundary layer are reliable.

The reliable wind profiles correlate well with traditional wind measurements made with an aircraft-based instrument, radiosondes, and weather stations. The comparisons do not indicate any systematic errors in the VIL wind profiles. The VIL wind profiles are more stable than the traditional measurements, since both time and area averaging is performed, while traditional measurements are either time-averaged or line-averaged.

The deviation between VIL wind profiles and traditional measurements is dominated by the natural wind fluctuations in the traditional measurements. Therefore, the errors in the VIL profiles are estimated from internal consistency. This is performed by comparing the wind estimates with the averages of the vertically adjacent estimates. Data from linear wind shear conditions are used to minimize deviations due to natural non-linear wind shear. The local root-mean-square errors of the hourly averaged wind profiles with $P_{max} = 1$ are 0.03–0.1 ms^{-1} in speed and 0.4–2° in direction. Since the local deviations are partly due to real wind fluctuations, they provide conservative error estimates.

The error in the interpolating fit due to noise in the CCF provides the RMS-errors of the wind estimates. These error estimates are slightly under estimated for two main reasons: 1) possible systematic aerosol structure deformation between the scans may shear the

correlation peak, and 2) the noise variance of the correlation function is hard to estimate, since the histogram equalization of the CAPPI scans changes non-linearly the statistical behavior of the noise. However, the error estimates provide lower bounds of the RMS-error.

Acknowledgments

The authors wish to express their gratitude to D. Forrest for managing the lidar data acquisition. The radiosonde data were measured by a team from Cornell University, directed by Prof. W. Brutsaert. Financial support to Antti Piironen is provided by Finnish Academy, Alfred Kordelin Foundation, Finland, Suomen Kulttuurin Edistämissäätiö Foundation, Finland, and University of Joensuu, Finland. The VIL is supported by NASA Grant NAG-5-902 and Army Research Office Grants DAAL03-86-K-0024 and DAAL03-91-C-0222.

References

Eloranta, E.W., and D.K. Forrest, 'Volume Imaging Lidar Observations of the Convective Structure Surrounding the Flight Path of a Flux-Measuring Aircraft', *J. Geophys. Res.*, **97**, D17, 18383–18393, 1992.

Hall, E.L., 'Almost Uniform Distributions for Computer Image Enhancement', *IEEE Trans. Comput.*, **C-23**, 2, 207–208, 1974.

MacPherson, J.I., 'NAE Twin Otter Operations in FIFE', National Aeronautical Establishment of Canada, *Laboratory Technical Report LTR-FR-104*, 1988.

Menke, W., 'Geophysical Data Analysis: Discrete Inverse Theory', *Academic Press*, 1984.

Press, W.H., B.P. Flannery, S.A. Teukolsky, W.T. Vetterling, 'Numerical Recipes in C, The Art of Scientific Computing', *Cambridge University Press*, 1988.

Schols, J.L., and E.W. Eloranta, 'The Calculation of Area-Averaged Vertical Profiles of the Horizontal Wind Velocity from Volume Imaging Lidar Data', *J. Geophys. Res.*, **97**, D17, 1992, 18395–18407.

Sellers, P.J., F.G. Hall, G. Asrar, D.E. Strebel, and R.E. Murphy, 'An Overview of the First International Satellite Land Surface Climatology Project (ISLSCP) Field Experiment (FIFE)', *J. Geophys. Res.*, **97**, D17, 18345–18371, 1992.

Sroga, J.T., and E.W. Eloranta: 'Lidar Measurements of Wind Velocity Profiles in the Boundary Layer', *J. Appl. Meteor.*, **19**, 5, 598–605, 1982.

Strebel, D.E., J.A. Newcomer, J.P. Ormsby, F.G. Hall, and P.J. Sellers, 'The FIFE Information System', *IEEE Trans. Geosci. and Remote Sensing*, **28**, 703–710, 1990.

Figure Captions:

Fig. 1. A filtered, wind corrected CAPPI scan on August 11, 1989, at 13:02 CDT at 1100 m altitude. The solid line represents the first shot angle of the scan; the dashed line represents the last shot angle of the scan. The arrow indicates the wind direction; its length represents the amount of correction for air parcel movements between the first and last shot. The bright areas represent increased backscatter from aerosols. The correction for air parcel movements during scanning shears the scanning area.

Fig. 2. The cross correlation function maximum peak (wire frame) on July 28, 1989, from 12:00 to 12:03 CDT at 500 meters altitude, fit points (diamonds), and the peak determined from the fit (rectangle). The horizontal axes represent the distance from the maximum point in pixels (one pixel equals 47 m). The correlation coefficient values are plotted on the vertical axis.

Fig. 3. Wind profiles after different averaging methods on August 9, 1989, from 10:30 to 10:45 CDT. The solid line of solid circles is a wind profile calculated from the average of five subsequent cross correlation functions. The dashed line with open circles is a wind profile calculated by averaging five individual wind profiles, which are estimated from subsequent cross correlation functions. The vertical dashed line at 500 m marks the convective boundary layer mean depth.

Fig. 4. P_{max} vs. speed (left) and direction (right) for quarter-hourly averaged wind estimates on July 27, 1989, from 8:00 to 15:00 CDT. All measurements with $P_{max} = 1$ are within natural deviation of the wind; the most widely fluctuating wind results have $P_{max} < 0.5$.

Fig. 5. Fraction of reliable results as a function of averaging time interval and P_{max} from July 26 to August 11, 1989. Open circles show fraction of results with $P_{max} = 1$ and altitudes ranging from 50 m to 2000 m; black rectangles show measurements in the convective boundary layer with $P_{max} = 1$; open diamonds show measurements in the convective boundary layer with $P_{max} > 0.9$. Averaging of CCF increases the fraction of reliable results by reducing random correlations.

Fig. 6. Quarter-hourly VIL wind speeds (contours), mean boundary layer (solid line), and cloud base (dash-dotted line) plotted as functions of time and altitude on July 26, 1989. The shaded areas indicate P_{max} is less than 1. In general, the results are reliable from the ground to 500 m above the cloud base. There are gaps in the data record at $\sim$ 14:00, 16:00, and 17:00 CDT causing P_{max} to decrease. Mixing of the boundary layer decreases the aerosol structure contrast in the volume scans causing occasional less reliable estimates in the middle of the mixed layer at 13:00, 14:40, and 15:30 CDT.

Fig. 7. Site locations and aircraft flight paths on July 27, 1989, from 11:00 to 12:00 CDT. The 40° sector outlines the VIL scanning area; the intersection of the rectangle and the sector (bold polygon) represents the area where the VIL wind profiles are calculated. Lines show aircraft flight paths; PAMS locations are marked with +; the radiosonde launch site is marked with *. The air parcels in the VIL scanning volume are measured by the aircraft about half hour later. The radiosonde launch site is about six kilometers north of the VIL site. The air parcels measured by the VIL missed the radiosonde site by about three kilometers.

Fig. 8. Hourly wind profiles of the VIL compared with radiosonde profiles, Twin Otter aircraft-based measurements, and PAMS ground measurements on July 27, 1989, from 11:00 to 12:00 CDT. The VIL results are marked with solid black symbols; error bars represent estimated RMS errors. Square symbols represent the radiosonde profiles which are vertically averaged to match the vertical spacing of the VIL results. The aircraft measurements are separated in East-West (open diamonds) and South-North (solid diamonds) directed flights and connected in temporal order starting from the lowest measurement. Hourly averaged measurements from eight PAMS are averaged together (solid triangle); the error bars indicate the smallest and greatest individual PAMS measurements.

Fig. 9. Comparison between VIL and aircraft-based wind speeds (left) and direction (right) measurements from the 1989 FIFE, from July 26 to August 11.

Fig. 10. Hourly averaged wind profiles on July 26, 1989, between 11:00 and 17:00 CDT. Only results with $P_{max} = 1$ are plotted. The mixed layer mean depth rises rapidly to $\sim$ 1000 m before 11:00 CDT when the clouds start forming. The base of convective clouds varies between 1000 m and 1800 m during the measurement session. The wind speed shear is linear except in the first 200-300 meters and at the top of the CBL. Error bars show estimated root-mean-square errors.

Fig. 11. Local deviations of hourly averaged wind speed and direction (open circles) and calculated RMS error estimates (black circles) on July 26, 1989, between 11:00 and 16:00 CDT. The error bars indicate the minimum and maximum error of hourly averaged wind estimates during 5-hour observation session. The calculated error estimates are probably too small, since only error in the interpolating fit is taken into account. On the other hand, the local deviations provide conservative error estimates, since they include also some real wind fluctuations.

Fig. 12. Root-mean-square error estimate profiles of reliable results as functions of averaging time interval and normalized altitude from July 26 to July 31, 1989. The altitude is normalized with the convective boundary layer mean depth. Note the logarithmic horizontal axes. The profiles show RMS errors of wind measurements with $P_{max} = 1$ averaged over a 5-hour period. Errors of 3-minute (open circles) and hourly average (black circles) profiles are shown. The RMS errors decrease as the averaging time interval increases. The minimum errors are obtained in the middle of the convective boundary layer. Below it, turbulent mixing smears the aerosol structures decreasing the signal to noise ratio of the CCF. Above it, the clouds block part of the data also decreasing the signal to noise ratio.

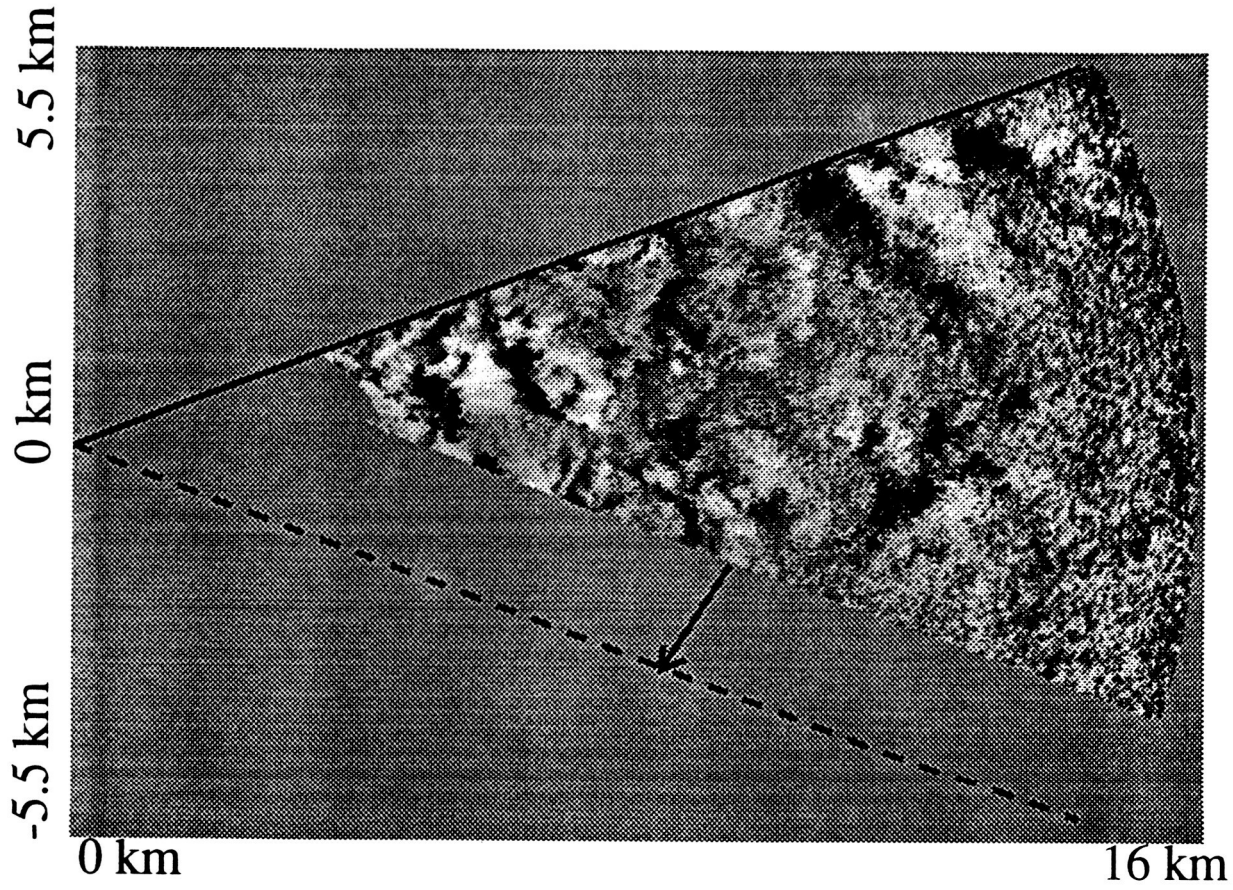

Fig. 1.

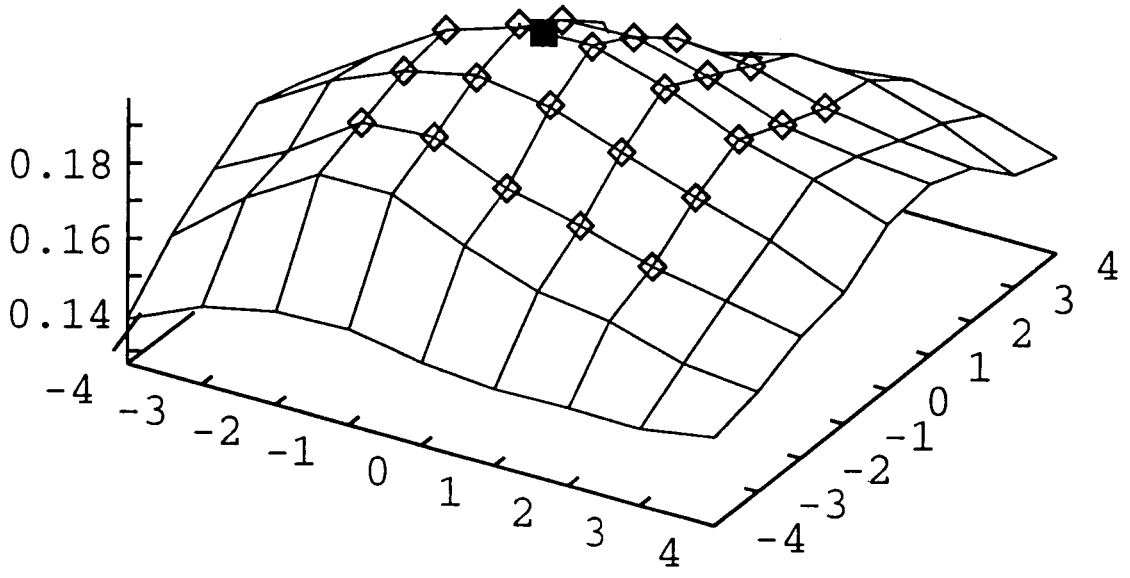

Fig. 2.

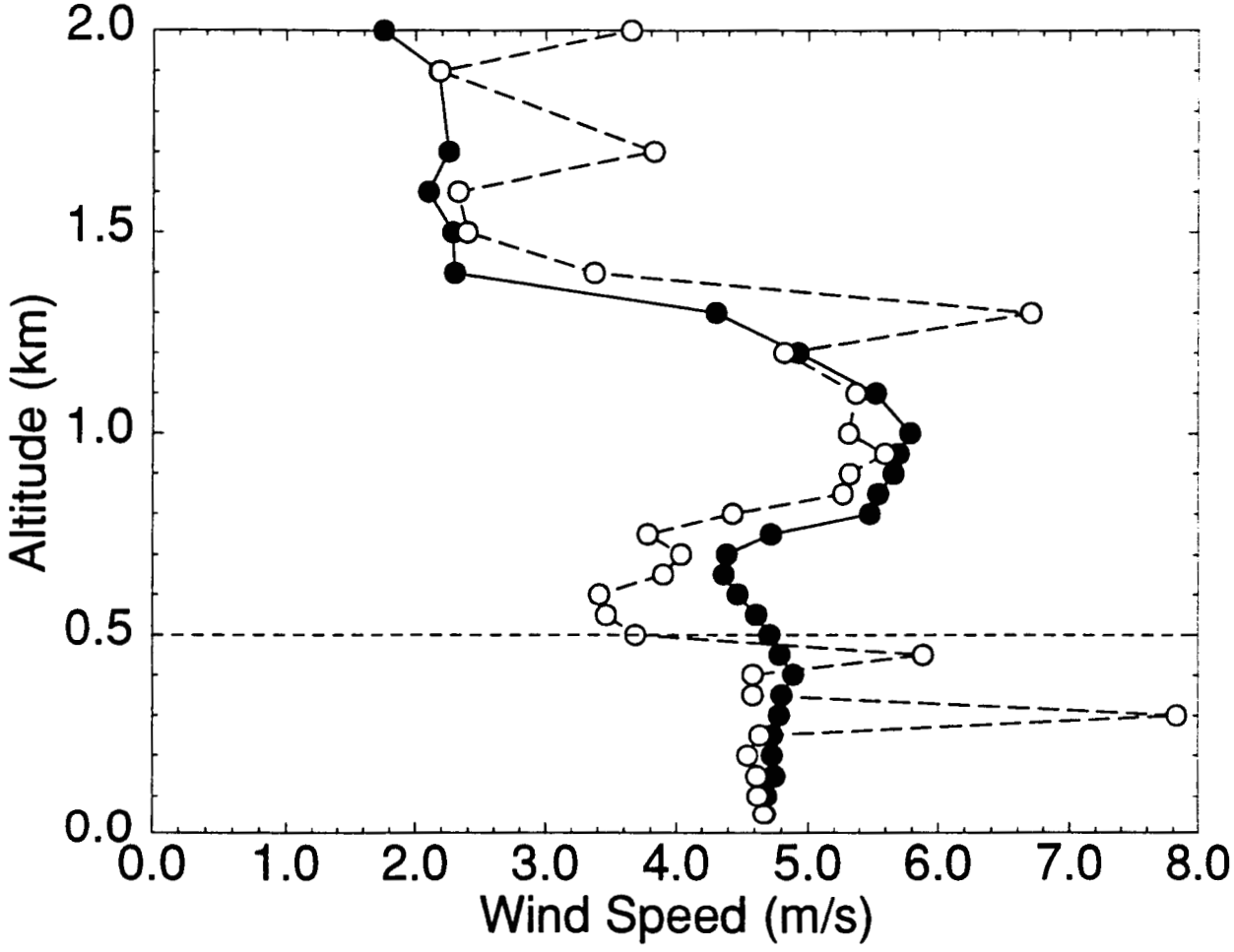

Fig. 3.

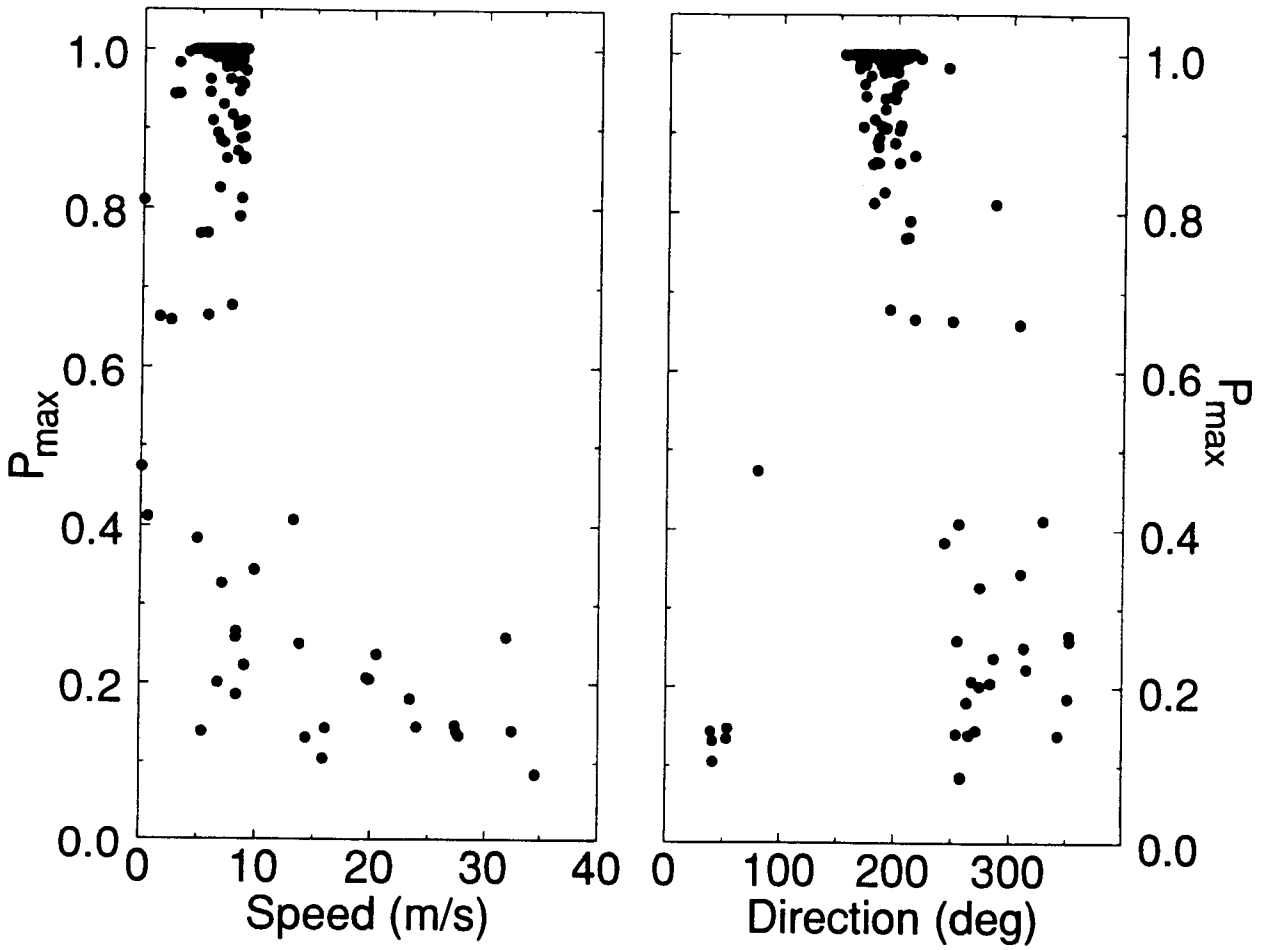
1.0
0.8
0.6
0.4
0.2
0.0
P_{max}
0
10
20
30
40
Speed (m/s)
0
100
200
300
Direction (deg)
1.0
0.8
0.6
0.4
0.2
0.0
P_{max}

Fig. 4.

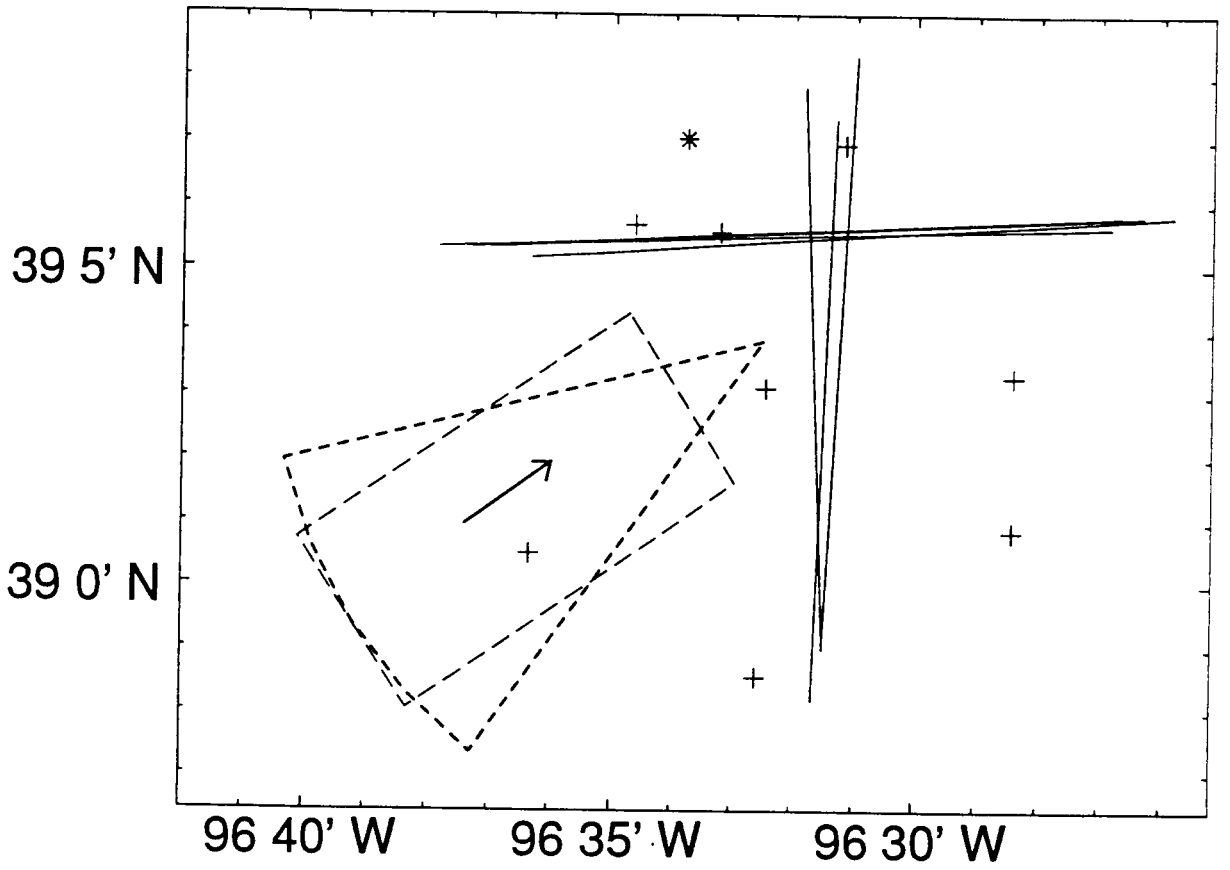

Fig. 7.

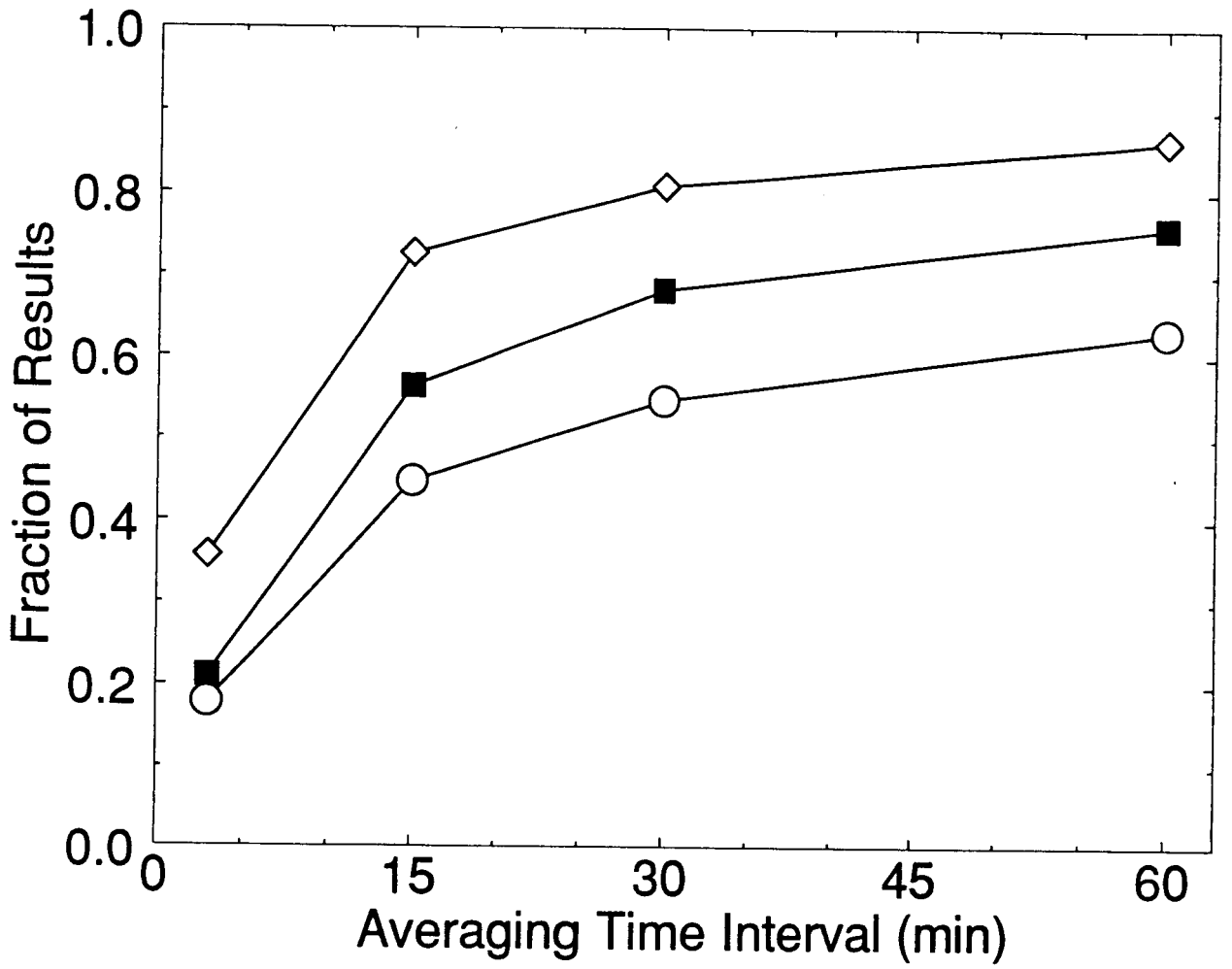
1.0
0.8
0.6
0.4
0.2
0.0
Fraction of Results
0
15
30
45
60
Averaging Time Interval (min)

Fig. 5.

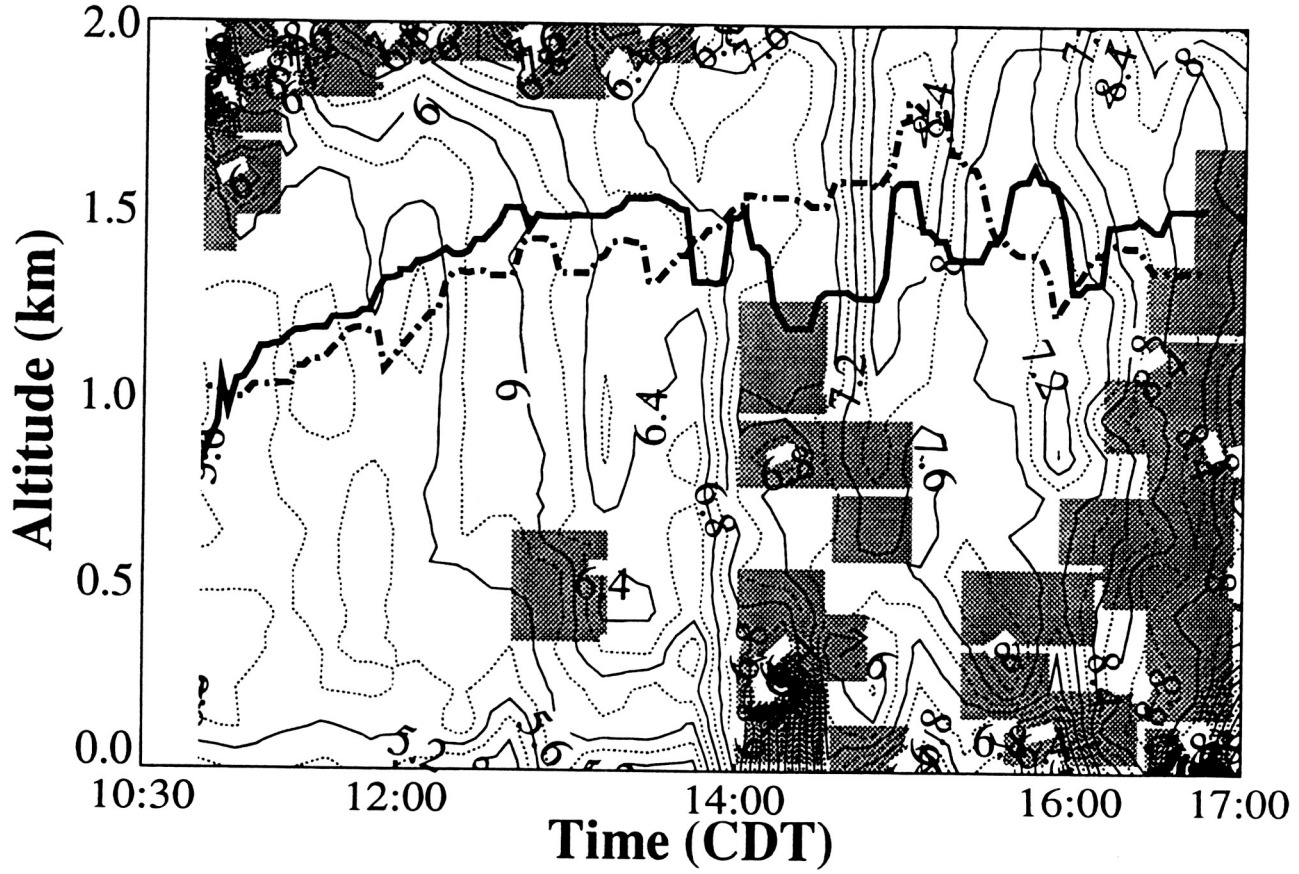

Fig. 6.

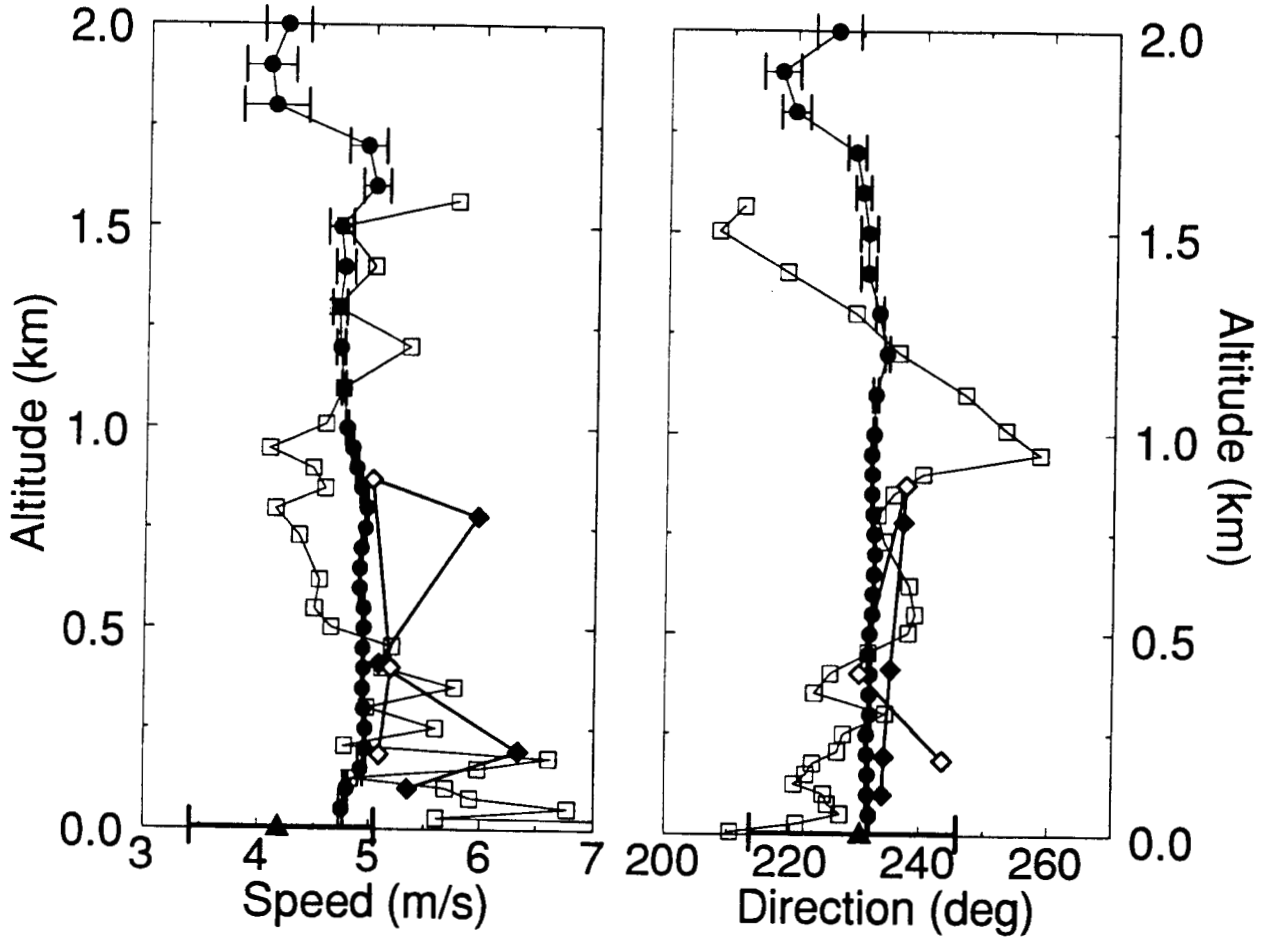
2.0
1.5
1.0
0.5
0.0
Altitude (km)
3
4
5
6
7
Speed (m/s)
200
220
240
260
Direction (deg)
2.0
1.5
1.0
0.5
0.0
Altitude (km)

Fig. 8.

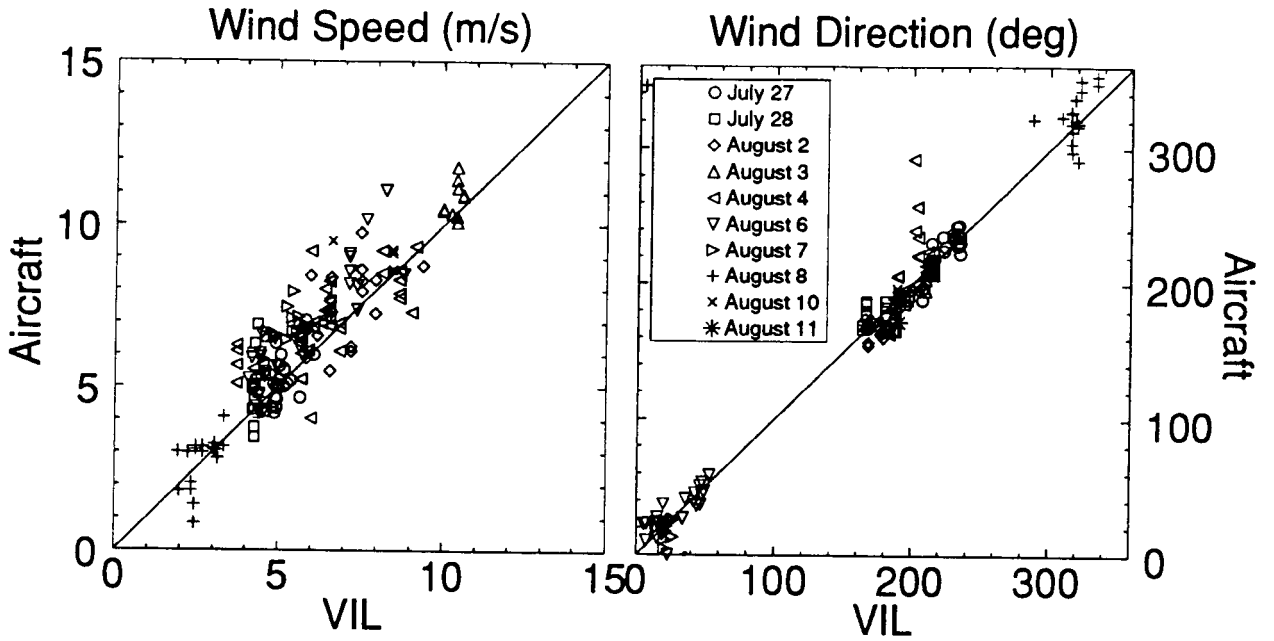
Wind Speed (m/s)
Wind Direction (deg)
Aircraft
VIL
July 27
July 28
August 2
August 3
August 4
August 6
August 7
August 8
August 10
August 11
0
5
10
15
100
200
300
150

Fig. 9.

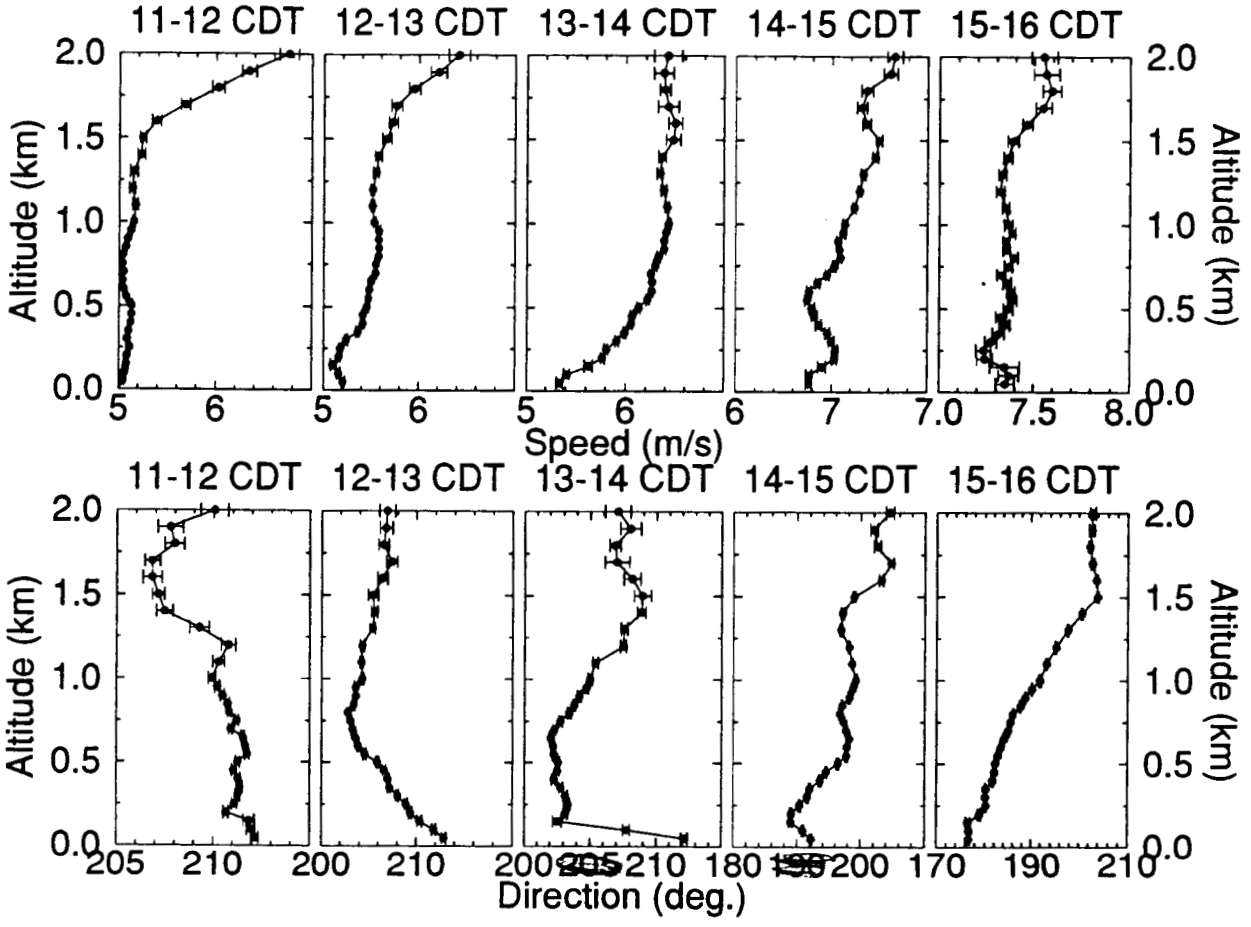
11-12 CDT
12-13 CDT
13-14 CDT
14-15 CDT
15-16 CDT
Altitude (km)
Speed (m/s)
Direction (deg.)

Fig. 10.

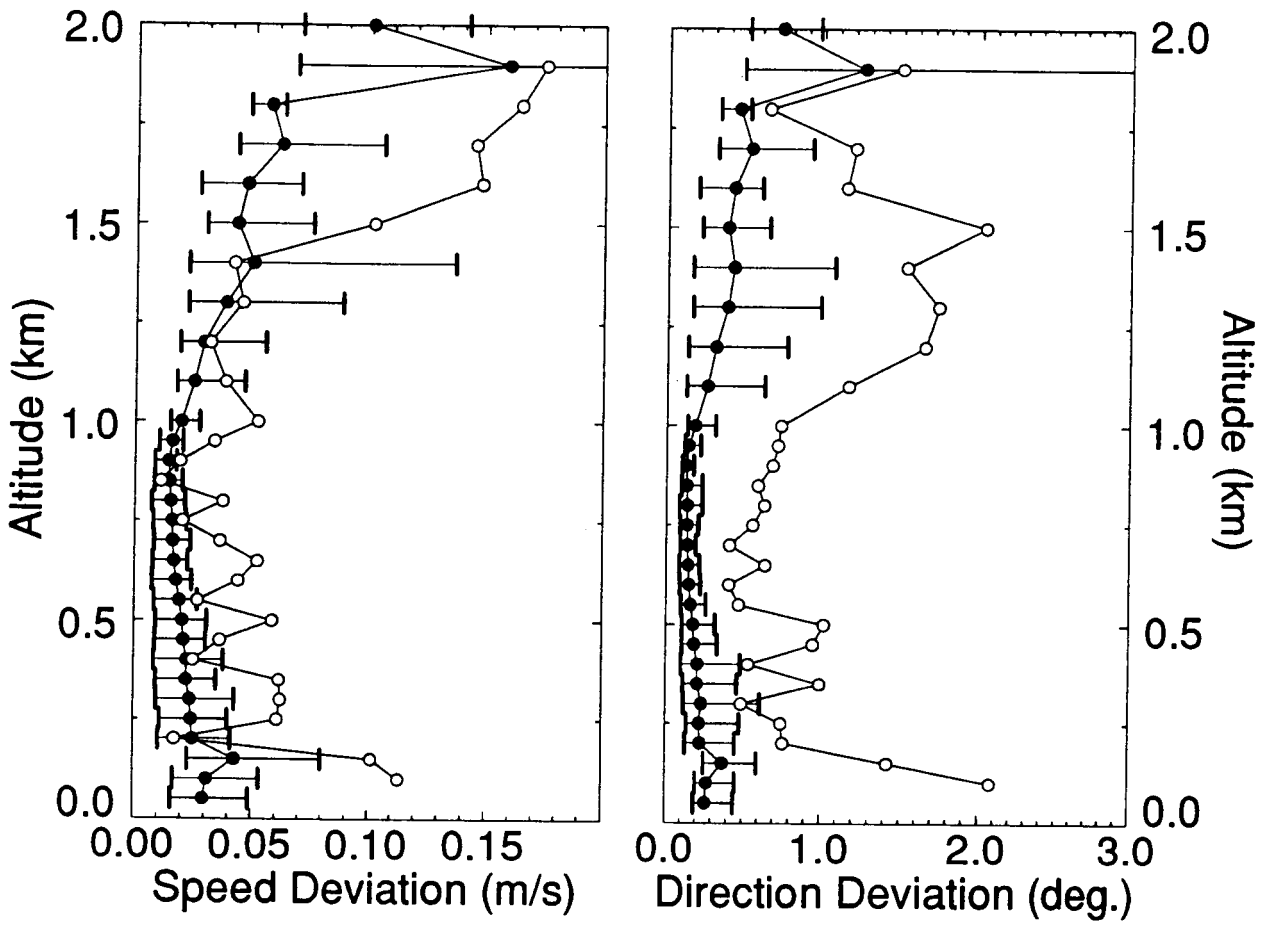
2.0
1.5
1.0
0.5
0.0
Altitude (km)
0.00 0.05 0.10 0.15
Speed Deviation (m/s)
0.0 1.0 2.0 3.0
Direction Deviation (deg.)
Altitude (km)

Fig. 11.

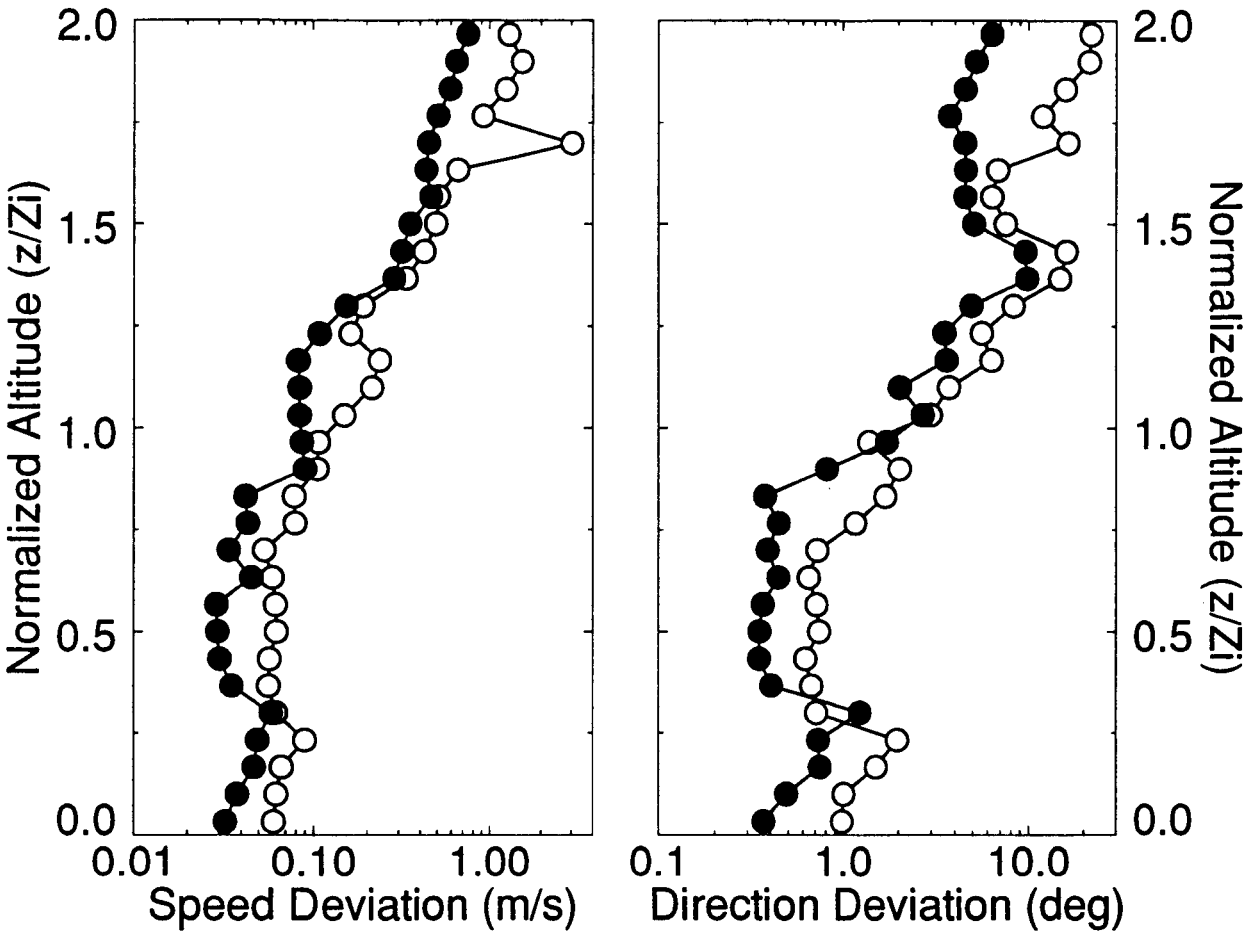
2.0
1.5
1.0
0.5
0.0
Normalized Altitude (z/Zi)
0.01
0.10
1.00
Speed Deviation (m/s)
0.1
1.0
10.0
Direction Deviation (deg)
Normalized Altitude (z/Zi)

Fig. 12.

Calculation of Divergence and Vertical Motion from Volume-Imaging Lidar Data

P. W. Young

Department of Physics

University of Wisconsin - Platteville

Platteville, WI 53818

and

E. W. Eloranta

University of Wisconsin - Madison

Deparment of Atmospheric and Oceanic Sciences

1225 West Dayton Street

Madison, WI 53706

ABSTRACT

Boundary layer divergences are calculated from a sequence of images of the inhomogeneities in aerosol backscattering observed with Volume-Imaging Lidar. Two-dimensional spatial cross correlations are calculated between successive horizontal plane maps, 10 km x 5 km, which are interpolated from the lidar returns. The first map represents the actual aerosol pattern; the second map is generated with an assumed divergence to remove the effects of that divergence from the image. The divergence is determined from an optimization of the correlation versus this assumed divergence. The results from this process are consistent with predictions for divergence over the spatial scale measured, and the apparent resolution of the results agrees with the image resolution.

1. INTRODUCTION

Horizontal divergence and vertical velocity are important parameters in the modeling of atmospheric processes at all scales. However, these quantities are very difficult to measure. On the synoptic scale vertical motion is important to weather prediction, climate modeling, and the study of general circulation. At present the most reliable measures of large-scale vertical motion come from analyzed wind fields produced by the National Meteorological Center and the European Center for Medium-Range Weather Forecasts [*Lambert*, 1989]. Radar wind profilers offer the potential for direct measurements of these large-scale motions, but their accuracy has not been fully established [*Gage*, 1990].

Mesoscale divergences and vertical motions are important in the study of convective storm systems and other boundary layer convergence processes. Single- and multi- Doppler radar systems have been used to measure average divergence over scales of 15 to 80 km (700 to 20,000 km^2) [*Browning and Wexler*, 1968; *Rabin and Zrnic*, 1980]. The divergence and other turbulence terms were determined from harmonic analysis of the azimuthal Doppler velocity field obtained with the scanning Doppler radar. The maximum fair-weather divergences measured over the above scales were of the order 10^{-5} s^{-1}. Vertical velocities were calculated from the divergences.

Less effort has been put into measuring smaller scale divergences and vertical velocities, although they influence the larger scale motions and are very important in boundary layer processes. Also, these smaller scales encompass subjects such as flow over obstacles and pollution studies. Doppler lidar data have been used to determine divergence and other turbulence parameters over scales between 150 m and 12 km [*Eberhard, et al*, 1989; *Gultepe, et al*, 1990; *Gal-Chen, et al*, 1992]. The divergences were calculated using the VAD technique developed for Doppler radar. The turbulent fluxes were computed from the

variance of the radial velocities. Small-scale vertical motions in the boundary layer have also been measured directly with radar wind profilers [*Ecklund*, et al 1988] and tower-mounted anemometers [*Skibin, et al*, 1985]. The measurements were averaged over short time intervals to provide the small-scale motions. Divergences at ground level have been measured over scales from 300 m to 6 km (0.04 to 15 km^2) using an optical propagation technique [*Kjelaas and Ochs*, 1974; *Fritz and Wang*, 1979]. The divergence was calculated from transverse velocities measured from the optical propagation along three legs of a triangle. The maximum values of the divergence measured over these areas ranged from 10^{-2} s^{-1} for the smaller area down to 10^{-3} s^{-1} for the larger area. Figure 1 summarizes these clear-weather divergence measurements over the micro- and meso-scales.

This paper describes a method for determining the spatially averaged horizontal divergence in the boundary layer from Volume-Imaging Lidar (VIL) data. The VIL produces a time sequence of images of the aerosol structure in 30° to 40° sectors of the boundary layer out to 15 km (60 km^2). Sequential images are correlated to determine the vertical profile of the horizontal divergence over the area of the images. From Figure 1 the maximum fair-weather divergences over the VIL area are expected to be of the order 10^{-4} s^{-1}.

2. METHOD OF DATA ANALYSIS

The time evolution of the atmospheric aerosol distribution in a particular volume of the boundary layer is due to the wind and turbulence, unless there are sources or sinks inside the area. The mean wind translates the distribution. Spatial variations in the wind, including the divergence, alter the pattern of the inhomogeneities in the distribution. VIL produces a time sequence of maps of this distribution from the aerosol backscattering of the laser beam. For wind and divergence calculations the data are processed to produce a vertical stack of

horizontal images which represent the aerosol distribution at constant altitude. The evenly spaced grid points in the images are produced by linear interpolation of the lidar returns. Each data point in the rectangular grid is the weighted average of all the lidar returns located in the eight cells surrounding the point. The weighting factor is inversely proportional to the distance from the grid point to the coordinates of the lidar return. The interpolation process also includes a first order correction for the image distortion caused by the mean wind over the scan time [*Schols and Eloranta*, 1992].

Calculations of vertical profiles of the mean horizontal wind from cross correlations of VIL images have been performed by *Schols and Eloranta* [1992] and *Piironen and Eloranta* [this issue]. The two-dimensional spatial cross correlation function (CCF) is calculated between two successive images in the same horizontal plane. The coordinates of the maximum of the CCF represent the mean displacement of the inhomogeneities in the distribution between the two images. This displacement divided by the time interval between the two images gives the mean horizontal velocity over the area. Time averaging of the mean velocity is accomplished by averaging the CCF for several time intervals before computing the velocity. These calculations are performed on image planes at different altitudes to construct a vertical profile of the horizontal velocity.

This method for calculating the mean wind over an area averages out the effects of the spatial variations in the wind. However, the horizontal divergence can be determined using the CCF method by incorporating the effects of the divergence on the two-dimensional distribution before calculating the CCF. The divergence in the horizontal wind field stretches (or compresses) the inhomogeneities in the aerosol distribution over time. The aerosol in a rectangle of area $A = L_x \times L_y$ at time t_1 is translated by the mean wind and spread by the divergence into the following area at time $t_2 = t_1 + \Delta t$: [*Hess*, 1959]

$$A' \approx L_x \left(1 + \frac{\partial u}{\partial x}\Delta t\right) \times L_y \left(1 + \frac{\partial v}{\partial y}\Delta t\right) \quad (1)$$

where

x,y = position coordinates in area, with x along the sector axis and y transverse to the axis;

u,v = velocity components along x and y, respectively;

L_x,L_y = image dimensions at time t_1;

Δt = time between images.

Therefore, in the VIL image at time t_2 the aerosol patterns are not only shifted by the mean wind, they are also spread out (or compressed) horizontally by the divergence. The effect of the divergence can be removed from the two-dimensional VIL image at time t_2 by recalculating an image of size A from the VIL return data from area A' centered on the mean wind displacement. The interpolation process is repeated with a grid size based on A' while the grid size in the final image is left consistent with A. This effectively compresses (or stretches) the inhomogeneities in the image back into their original shape. The maximum of the CCF between this "corrected" image at t_2 and the actual image at t_1 should be greater than the maximum of the corresponding CCF between the actual images at both times. Thus, the value of the horizontal divergence in the time interval between two VIL images can be determined by optimizing the maximum of the CCF between the two images versus $\partial u/\partial x$ and $\partial v/\partial y$.

This process has been applied to lidar data taken with the University of Wisconsin VIL [*Eloranta and Forrest*, 1992]. The data were taken in a 40° sector out to a range of 15 km and up to an altitude of 2 km. For the divergence calculations the original image area was a 10 km x 5 km rectangle between the ranges of 4 km and 14 km. The images of this area

were processed into 200 x 100 data arrays. The vertical spacing between image planes was 50 m. The time interval between successive images was 180 to 200 s.

The maxima of the CCFs between successive images (corresponding to the mean wind displacement) ranged from about 0.1 to 0.4 for the data analyzed. The image at time t_2 was taken from the same area as the image at t_1 so the CCF maximum was displaced from the origin by the mean wind. The value of the CCF maximum was determined from a two-dimensional, 2nd order polynomial fit to the CCF data about the peak. The correlation peak is not a 2nd order polynomial, but the polynomial is an acceptable approximation over a small square of grid points around the peak. When the actual image at time t_2 was replaced by an image processed from the area adjusted for the divergence according to equation (1), the CCF maximum improved as seen in Figure 2. The amount of improvement ranged from 0% (when the divergence was zero) to about 10%.

Optimization of the CCF maximum was carried out by calculating the CCFs between the actual image at t_1 and images at t_2 adjusted for an array of assumed $\partial u/\partial x$ and $\partial v/\partial y$ in equation (1). The increments in $\partial u/\partial x$ and $\partial v/\partial y$ were chosen to match the image resolution, 50 m. The images were altered symmetrically so the incremental changes in L_x and L_y were 100 m, corresponding to increments of 5×10^{-5} s^{-1} and 10×10^{-5} s^{-1} for $\partial u/\partial x$ and $\partial v/\partial y$, respectively. Figure 3 shows a plot of these calculations. The optimum values for $\partial u/\partial x$ and $\partial v/\partial y$ were determined by fitting a two-dimensional, 2nd-order polynomial in $\partial u/\partial x$ and $\partial v/\partial y$ to the graph. The divergence was identified as the sum of these optimum values. Time averaging of the divergence was achieved by performing these optimization calculations on time-averaged CCFs (i.e. the average of several sequential CCFs).

This CCF technique for calculating divergence is limited by the resolution in the two-dimensional images, 50 m x 50 m. Stretching the image by this amount produces $\partial u/\partial x$ and

$\partial v/\partial y$ values of 2.5×10^{-5} s^{-1} and 5×10^{-5} s^{-1}, respectively. These values provide a rough estimate of the limiting resolution for the technique. The resulting resolution in the divergence is $\sim 6 \times 10^{-5}$ s^{-1}. This limit is considerably larger than the limitations on mean wind calculations from CCFs discussed in *Piironen and Eloranta* [this issue]. They report mean wind uncertainties of less than 0.1 m/s using CCF calculations over approximately the same area. This uncertainty in the mean wind corresponds to a divergence of less than 2×10^{-5} s^{-1}.

The continuity equation was used to relate the gradient of the vertical motion to the horizontal divergence,

$$\left(\frac{\partial u}{\partial x} + \frac{\partial v}{\partial y}\right) + \frac{\partial w}{\partial z} = -\frac{1}{\rho}\frac{\partial \rho}{\partial t} \qquad (2)$$

where

z = vertical coordinate;

w = vertical component of velocity;

ρ = density of fluid.

For an incompressible fluid the gradient of the vertical wind is the negative of the horizontal divergence. Therefore, the average vertical motion over the area imaged by the VIL can be determined from the integral of the vertical profile of the divergences.

3. RESULTS

This section presents results of divergence and vertical motion calculations on VIL data taken as part of the First ISLSCP Field Experiment (FIFE) 1989 on the Konza Prairie research site near Manhattan, Kansas. The VIL scans were centered on azimuth 236°. Two data sets representing different wind conditions were chosen to test the divergence algorithm.

The first set was collected between 1145 and 1240 CDT on August 3, 1989. The sky was overcast with a stratocumulus clouddeck which was just beginning to break up during the data period. The lowest clouds extended down to 400 m at the beginning of period. By 1240 CDT the lowest clouds had risen to 550 m. These low clouds interfered somewhat with the divergence analysis between 400 and 600 m. The wind was relatively constant beteen 10 and 11 m/s at 220°. This wind was approaching the lidar 26° off the center angle of the scan. The wind profile midway through the time interval is shown in Figure 4.

Because of the relatively high wind speed, the divergence calculations were performed on CCFs averaged over about 15 minutes (5 scans). Figure 5 shows the divergence profiles below the clouddeck at three times selected so the data averages do not overlap. Between about 150 m and 500 m the horizontal divergence appears relatively constant at an average of -6×10^{-5} s^{-1} with a standard deviation of 7×10^{-5} s^{-1} for the 24 data points. If the data at 150 m are omitted, the standard deviation is only 5×10^{-5} s^{-1}. Integrating the average divergence up to 500 m gives a 3 cm/s upward velocity at 500 m. The magnitude of the divergence is consistent with the expected divergence over 50 km^2 from Figure 1, and the standard deviation is approximately equal to the expected resolution, $\sim 6 \times 10^{-5}$ s^{-1}.

Above 500 m and below 150 m the results fluctuate much more than the estimated resolution. The fluctuations above 500 m can be attributed to interference from the low-hanging clouds. The large fluctuations at low altitudes are consistent with the observed deterioration of low altitude velocity calculations from CCFs [*Piironen and Eloranta*, this issue].

The second data set was collected between 0817 and 1045 CDT on July 28, 1989. This day was mostly clear with some cirrus. A few scattered boundary layer clouds developed just after this period. The mixed layer increased from about 100 m at the start to about 750 m

at the end. The winds were weaker than on August 3, starting at about 3.5 m/s at 210° and increasing steadily to about 4.5 m/s at 195° by the end. The wind was approaching the lidar between 26° and 41° from the center angle of the scan. Figure 6 shows the wind profiles during the data interval.

The divergence calculations for this day were performed on CCFs averaged over just 10 minutes (3 scans). Figure 7 shows divergence profiles for three times over 30 minutes, the same time span observed on August 3. In contrast to Figure 5, the individual profiles are not constant below the mixed layer, and on this day the divergence changed significantly with time. At the lower altitudes the profiles shift from convergent to divergent within the half hour period. Over the entire 2½-hour period, the divergence below the mixed layer varied from about -25×10^{-5} to $+25 \times 10^{-5}$ s^{-1}. Figure 8 shows these variations at a single altitude. The divergence changed continuously for the full data period.

Because the divergence was changing with both time and altitude, the standard deviation of all the divergence values would be greater than the resolution. Instead, the resolution is estimated from the standard deviation of the *difference* between divergences at successive, independent times which is 11×10^{-5} s^{-1}. These fluctuations in the *difference* correspond to an uncertainty of less than 8×10^{-5} s^{-1} on the divergence, comparable to the estimated resolution based on the image resolution. Furthermore, a temporal correlation calculation on the data at all elevations indicates a correlation time of 20 to 30 minutes for the divergence on this day.

However, it is also recognized that these observed correlations in the divergence might be produced by similarities in the aerosol maps which persist for 20 to 30 minutes. All the images involved in the divergence calculations represent the same data area, so the images are correlated. It is possible that this correlation in the images is producing the observed

correlation in the divergence. Under this assumption, the temporal variations in the divergence would merely represent the random variations due to the uncertainties in the measurements. The standard deviation of the data would be the resolution on the divergence. This value would represent the upper limit on the resolution for this technique. Figure 9 represents this interpretation of the results for July 28. This figure contains plots of all the gradient ($\partial u/\partial x$ and $\partial v/\partial y$) and divergence values measured below the mean mixed layer. The solid line on the divergence graph represents the divergence calculated from the CCF averaged over the entire 2½-hour time period. The data points in each graph all average out to about zero, and the scatter could be viewed as just the uncertainty in the measurement. The standard deviations for $\partial u/\partial x$, $\partial v/\partial y$, and divergence are 7×10^{-5}, 10×10^{-5}, and 11×10^{-5} s^{-1}, respectively. The scatter in $\partial v/\partial y$ is greater than that in $\partial u/\partial x$ because the transverse dimension is smaller. The 11×10^{-5} s^{-1} standard deviation in the divergence represents the upper limit on the resolution for this technique. This value is about twice the resolution estimated from the image resolution, but it is still the same order of magnitude as the expected maximum divergence over the area.

4. CONCLUSIONS

Horizontal divergence values, spatially averaged over 50 km^2, have been calculated from VIL data taken during FIFE. On an overcast day with medium winds the divergence below the clouds was relatively constant around -6×10^{-5} s^{-1} for over a half hour. On a clear day with light winds the divergence changed continuously between -25×10^{-5} and $+25 \times 10^{-5}$ s^{-1} with a correlation time around 20 minutes. These measured divergences are consistent with the expected scale variations presented in Figure 1. The internal consistency of the results indicate that the uncertainty on the divergence is about 7×10^{-5} s^{-1}, a value consistent with

the spatial resolution of the images. This indicates that these results are as reliable as can be expected from the lidar data available.

Even if this internal consistency of the results is rejected, the most conservative interpretation of the data yields an upper limit on the resolution for the technique of 11 x 10^{-5} s^{-1} which is the standard deviation of all the results below the mean mixed layer. This upper limit is less than twice the resolution based on the image resolution, and it is still the same order of magnitude as the expected maximum divergence over a 50 km^2 area. With reasonable improvements in the data collection procedures, this resolution can be reduced enough to measure divergences on this scale.

Further development of this technique for measuring divergence with VIL will require improvements in the VIL to improve the resolution. The present resolution is limited by the image size and resolution. Increasing the repetition rate of the VIL would improve both these limations. The rate could be increased from 30 Hz to 1 kHz without interference from wrap-around returns from distant clouds. About 300 Hz would allow for 360° scans with smaller azimuthal steps in the same time interval. With a 360° image out to 15 km the image grid could be increased to 20 x 20 km. The additional factor of three in the repetition rate would also allow for smaller azimuthal steps, thus decreasing the image resolution to about 20 m. These two factors combined would provide a divergence resolution of about 5 x 10^{-6} s^{-1}. The increased image area and resolution would also improve the image correlation, possibly improving the resolution even more. With this level of performance the VIL could be used to monitor even weak divergences over the 400 km^2 area, thus complementing the existing data on horizontal divergence. This area would also overlap with Doppler radar's capabilities allowing for comparisons.

Acknowledgements: The authors thank Dan Forrest for designing the software for the data acquisition system and Antti Piironen for the CCF software. This work was partially supported by a SAIF grant from University of Wisconsin - Platteville and by NASA Goddard Grant NAG 5-902 and ARO Grants DAAL03-86-K-0024 and DAAL03-91-G-0222.

REFERENCES

Boers, R., E.W. Eloranta and R.L. Coulter, Lidar observations of mixed layer dynamics: tests of parameterized entrainment models of mixed layer growth rate, *J. Climate Appl. Meteorol.*, *23*, 247-266, 1984.

Browning, K.A., and R. Wexler, The detemination of kinematic properties of a wind field using Doppler radar, *J. Appl. Meteorol.*, *7*, 105-113, 1968.

Eberhard, W.L., R.E. Cupp and K.R. Healy, Doppler lidar measurement of profiles of turbulence and momentum flux, *J. Atmos. Oceanic Technol.*, *6*, 809-819, 1989.

Ecklund, W.L., D.A. Carter and B.B. Balsley, A UHF wind profiler for the boundary layer: brief description and initial results, *J. Atmos. Oceanic Technol.*, *5*, 432-441, 1988.

Eloranta, E.W., and D.K. Forrest, Volume-Imaging Lidar observations of the convective structure surroundiing the flight path of a flux-measuring aircraft, *J. Geophys. Res.*, *97*, 18,383-18,393, 1992.

Fritz, R.B., and T.-I. Wang, Chapt. 9. Optical systems measuring surface-level convergence during PHOENIX, in *Project PHOENIX*, Report No. 1, edited by W.H. Hooke, pp. 104-111, NOAA.ERL, Boulder, CO, 1979.

Gage, K.S., Radar observations of the free atmosphere: structure and dynamics, in *Radar in Meteorology: Battan Memorial and 40th Anniversary Radar Meteorology Conference*, edited by D. Atlas, pp. 534-565, American Meteorological Society, Boston, 1990.

Gal-Chen, T., M. Xu and W.L. Eberhard, Estimations of atmospheric boundary layer fluxes and other turbulence parameters from Doppler lidar data, *J. Geophys. Res., 97*, 18,409-18,423, 1992.

Gultepe, I., A.J. Heymsfield and D.H. Lenschow, A comparison of vertical velocity in cirrus obtained from aircraft and lidar divergence measurements during FIRE, *J. Atmos. Oceanic Technol., 7*, 58-67, 1990.

Hess, Seymour L., *Introduction to Theoretical Meteorology*, 362 pp., Henry Holt and Company, New York, 1959.

Kjelaas, A.G., and G.R. Ochs, Study of divergence in the boundary layer using optical propagation techniques, *J. Appl. Meteorol., 13,* 242-248, 1974.

Lambert, Steven J., A comparison of divergent winds from the National Meteorological Center and the European Centre for Medium Range Weather Forecasts global analyses for 1980-1986, *Mon. Wea. Rev., 117*, 995-1005, 1989.

Piironen, A.K., and E.W. Eloranta, An accuracy analysis of the wind profiles calculated from Volume Imaging Lidar data, *J. Geophys. Res.*, this issue.

Rabin, R., and D. Zrnic, Subsynoptic-scale vertical wind revealed by dual Doppler-radar and VAD analysis, *J. Atmos. Sci., 37,* 644-654, 1980.

Rabin, R., and I. Zawadzki, On the single-Doppler measurements of divergence in clear air, *J. Atmos. Oceanic Technol., 1*, 50-57, 1984.

Schols, J.L., and E.W. Eloranta, Calculation of area-averaged vertical profiles of the horizontal wind velocity from Volume-Imaging Lidar data, *J. Geophys. Res., 97*, 18,395-18,407, 1992.

Skibin, D., J.C. Kaimal and J.E. Gaynor, Measurement errors in vertical wind velocity at the Boulder Atmospheric Observatory, *J. Atmos. Oceanic Technol., 2*, 598-604, 1985.

Stull, Roland B., *An Introduction to Boundary Layer Meteorology*, 666 pp., Kluwer Academic Publishers, Dordrecht, 1988.

Vachalek, Roger E., Case studies of divergence and vertical velocities calculated using different sensing systems, M.S. thesis, Univ. of Wisconsin, Madison, 1987.

FIGURE CAPTIONS

Fig. 1. Scale dependence of the fair-weather divergence measurements from the literature. The optical propagation data are plotted as the open triangle [*Kjelaas and Ochs*, 1974] and the solid triangles [*Fritz and Wang*, 1979]. Doppler radar measurements are plotted as solid squares [*Rabin and Zrnic*, 1980] and open squares [*Rabin and Zawadzki*, 1984]. The solid circle represents lidar measurements by *Boers, Eloranta, and Coulter* [1984]. The open circles are the median values from an experiment involving several sensors reported by *Stull* [1988, after *Vachalek*, 1987]. The VIL measurements reported in this paper are spatially averaged over 50 km^2.

Fig. 2. A comparison of the CCF calculated between the actual images at both t_1 and t_2 (solid line) and the CCF calculated with a divergence-corrected image at time t_2 (dotted line). The largest cross correlation was found with $\partial u/\partial x = 10 \times 10^{-5}$ s^{-1} and $\partial v/\partial y = -10.0 \times 10^{-5}$ s^{-1}. The graphs show the cross sections of the two-dimensional cross correlation function around the peak. The CCFs were averaged over 3 images (10 min.).

Fig. 3. CCF maxima as a function of assumed divergence for the same lidar data represented in Figure 2. The divergence was determined by fitting a 2nd order polynomial to this graph: $\partial u/\partial x = 12.4 \times 10^{-5}$ s^{-1}, $\partial v/\partial y = -6.6 \times 10^{-5}$ s^{-1}, divergence $= 5.8 \times 10^{-5}$ s^{-1}.

Fig. 4. Wind velocity profile at 1213 CDT on August 3, 1989. The velocity and direction were calculated from the shift in the location of the CCF peak. The CCFs were averaged over 5 images (17 min.).

Fig. 5. Divergence profiles for 1157 CDT (circles), 1213 CDT (squares), and 1228 CDT (triangles) on August 3, 1989. The data from 150 m to 500 m appear constant at an average of -6×10^{-5} s^{-1} with a standard deviation of 7×10^{-5} s^{-1}.

Fig. 6. Wind velocity profiles at hour intervals on July 28, 1989. The velocity and direction were calculated from the shift in the location of the CCF peak. The CCFs were averaged over 3 images (10 min.).

Fig. 7. Divergence profiles for 0922 CDT (circles), 0939 CDT (triangles), and 0954 CDT (squares) on July 28, 1989. The solid symbols with solid lines represent data below the mean mixed layer; the open symbols with dotted lines show additional data above the mixed layer.

Fig. 8 Time evolution of the divergence at 200 m on July 28, 1989. Each point represents a 10 minute average; the points are spaced so the averages do not overlap.

Fig. 9. Scatter plots of all the gradient and divergence results below the mean mixed layer on July 28, 1989. The divergence data are the sum of the corresponding data for the gradients. The points were selected from profiles separated by 10 minutes so they represent independent CCFs. The solid line in the divergence profile shows the divergence values calculated from the CCFs averaged over the entire 2½ hour period.

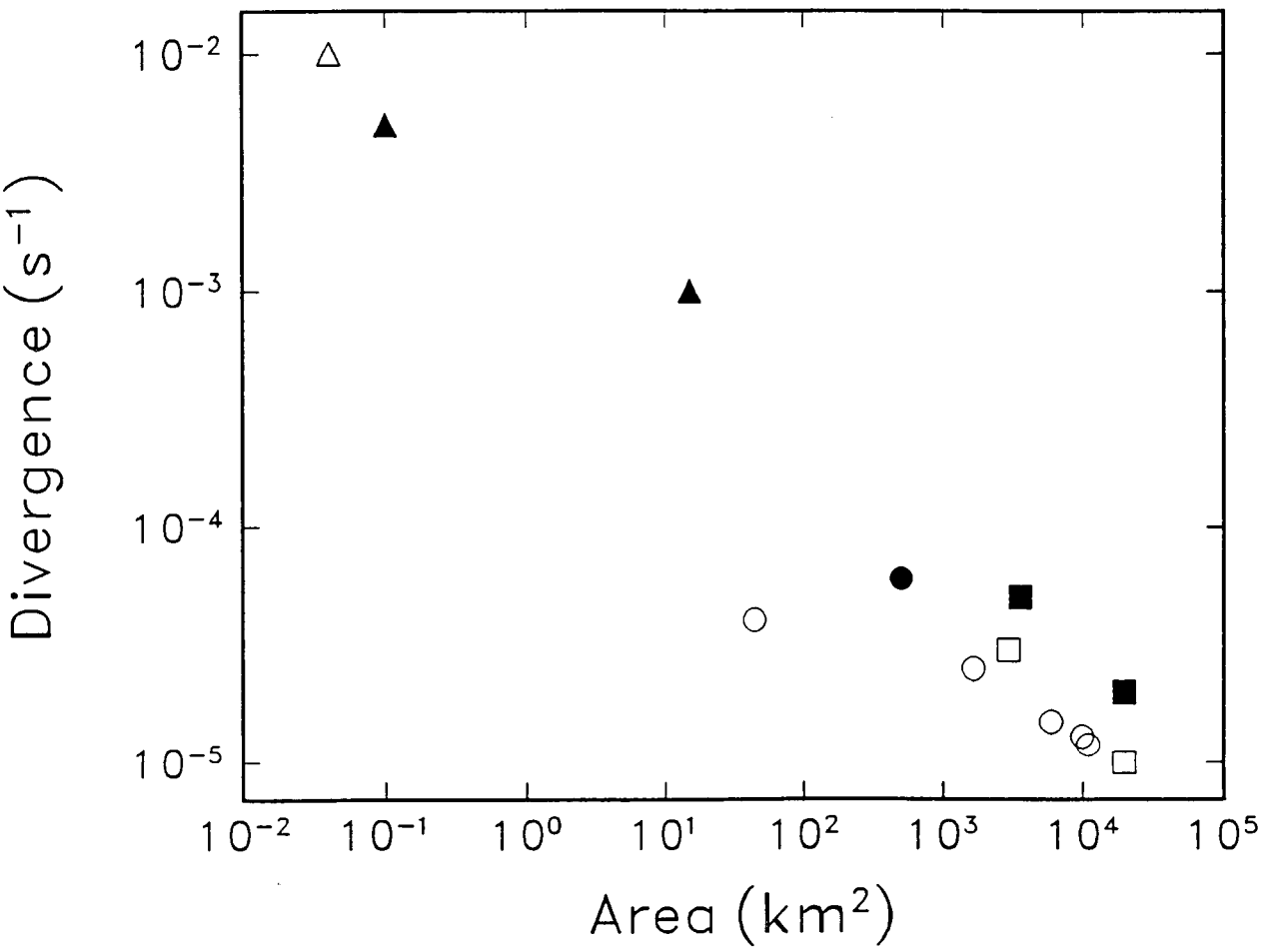
Divergence (s^{-1})
10^{-2}
10^{-3}
10^{-4}
10^{-5}
10^{-2} 10^{-1} 10^{0} 10^{1} 10^{2} 10^{3} 10^{4} 10^{5}
Area (km^2)

Fig. 1

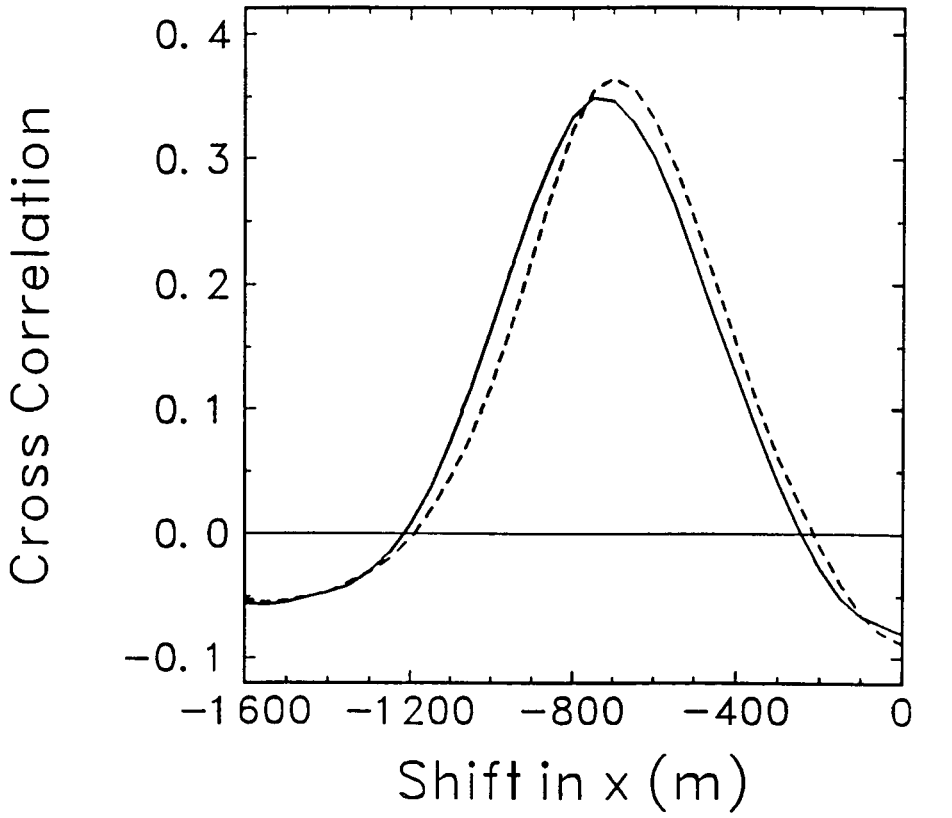
Cross Correlation
0. 4
0. 3
0. 2
0. 1
0. 0
−0. 1
−1 600
−1 200
−800
−400
0
Shift in x (m)

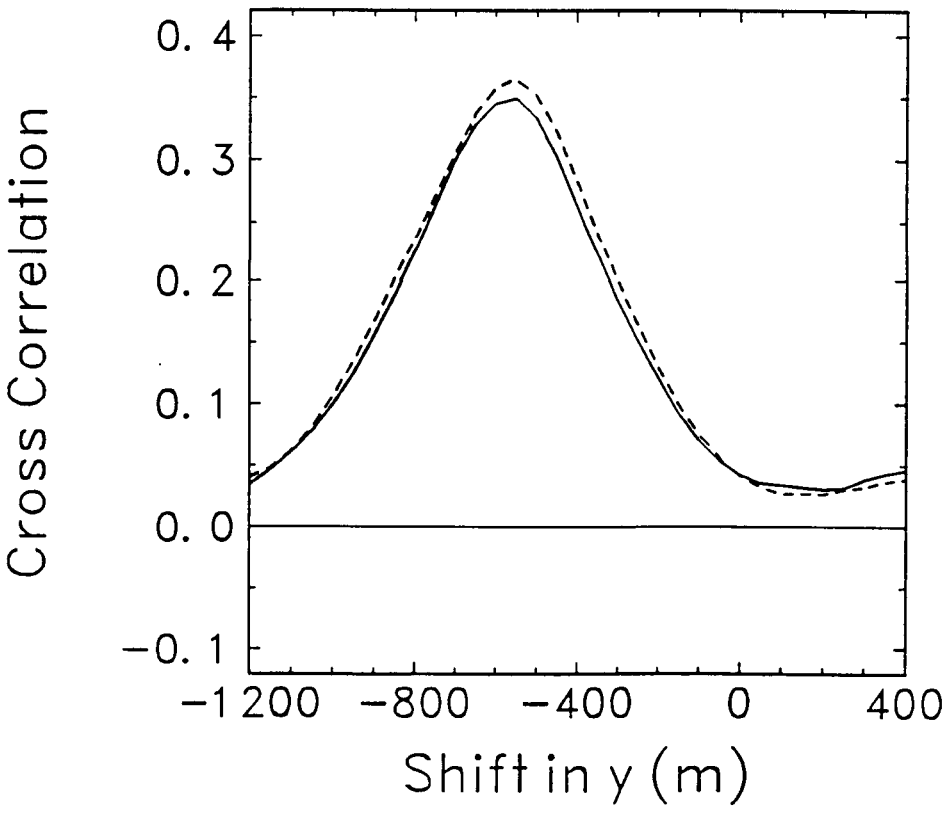
Cross Correlation
0. 4
0. 3
0. 2
0. 1
0. 0
−0. 1
−1 200
−800
−400
0
400
Shift in y (m)

Fig. 2

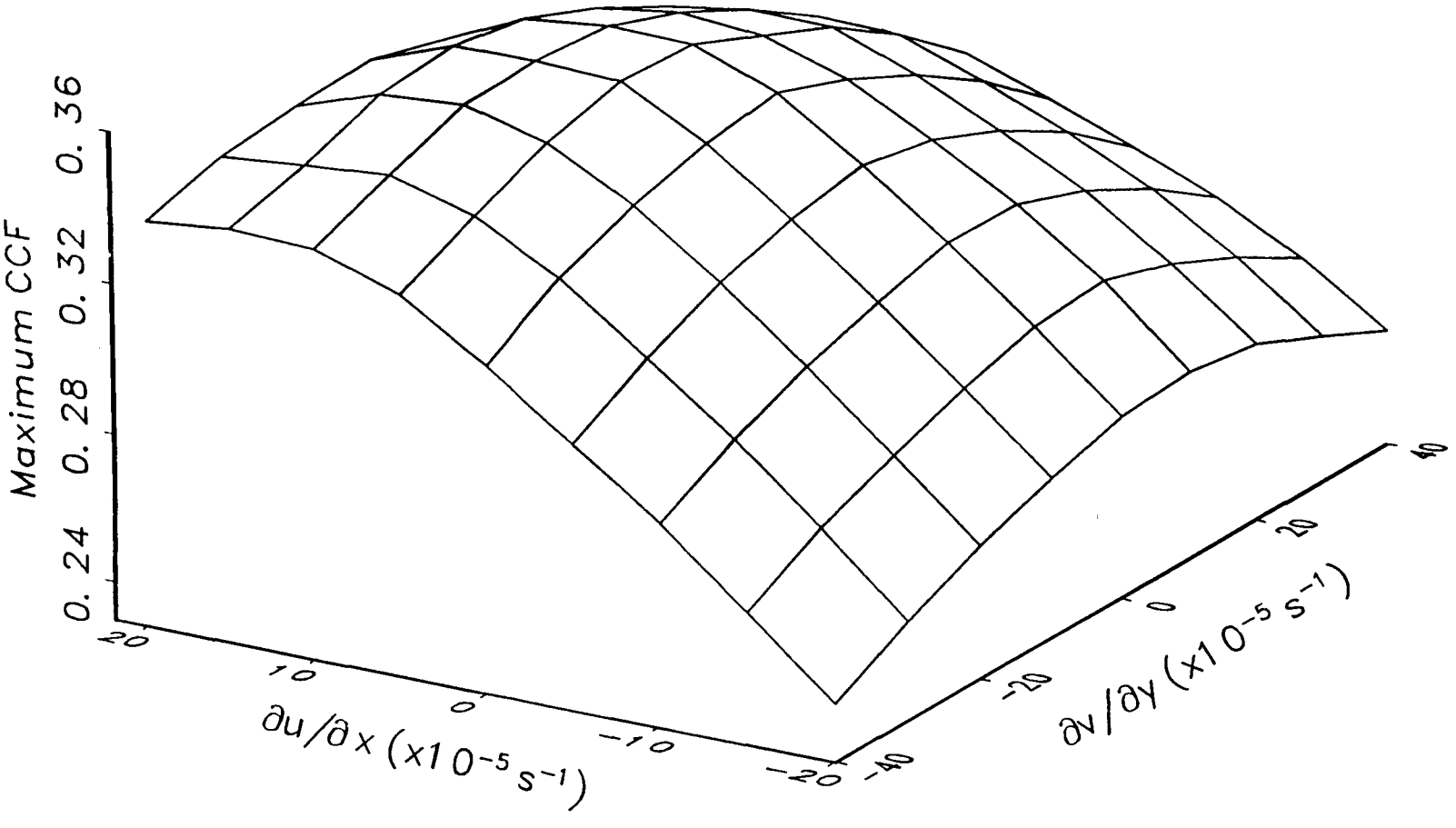
Maximum CCF
0.24
0.28
0.32
0.36
20
10
0
-10
-20
∂u/∂x (x10⁻⁵ s⁻¹)
-40
-20
0
20
40
∂v/∂y (x10⁻⁵ s⁻¹)

Fig. 3

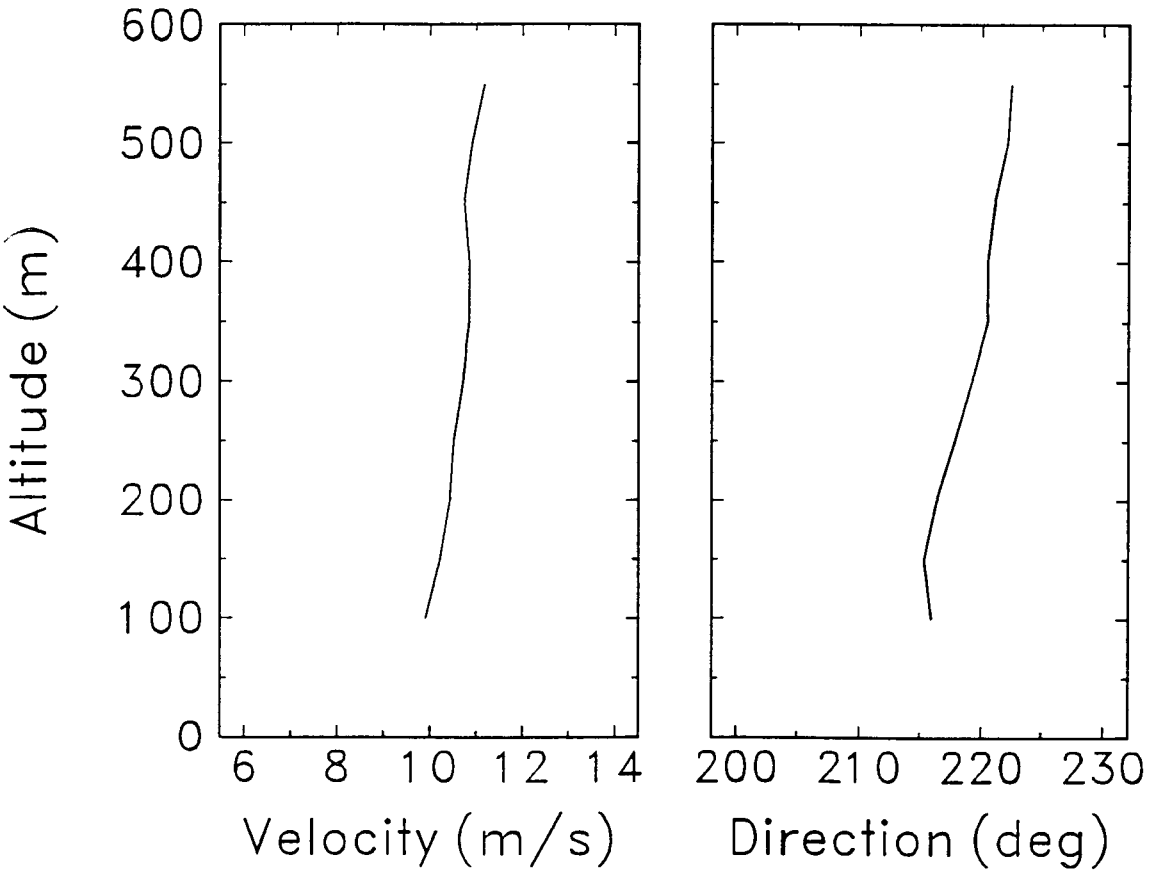
600
500
400
300
200
100
0
Altitude (m)
6
8
10
12
14
Velocity (m/s)
200
210
220
230
Direction (deg)

Fig. 4

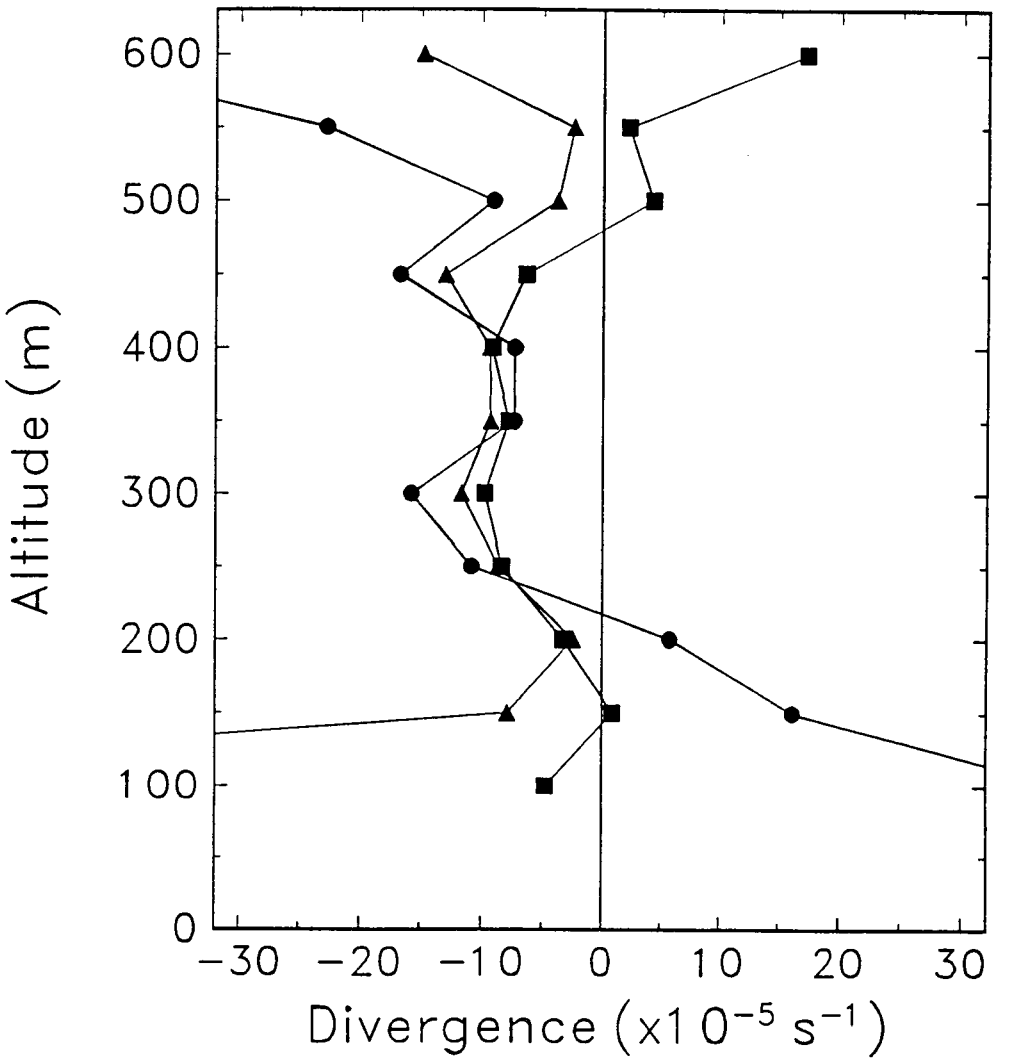
600
500
400
300
200
100
0
Altitude (m)
−30
−20
−10
0
10
20
30
Divergence (x10^{-5} s^{-1})

Fig.5

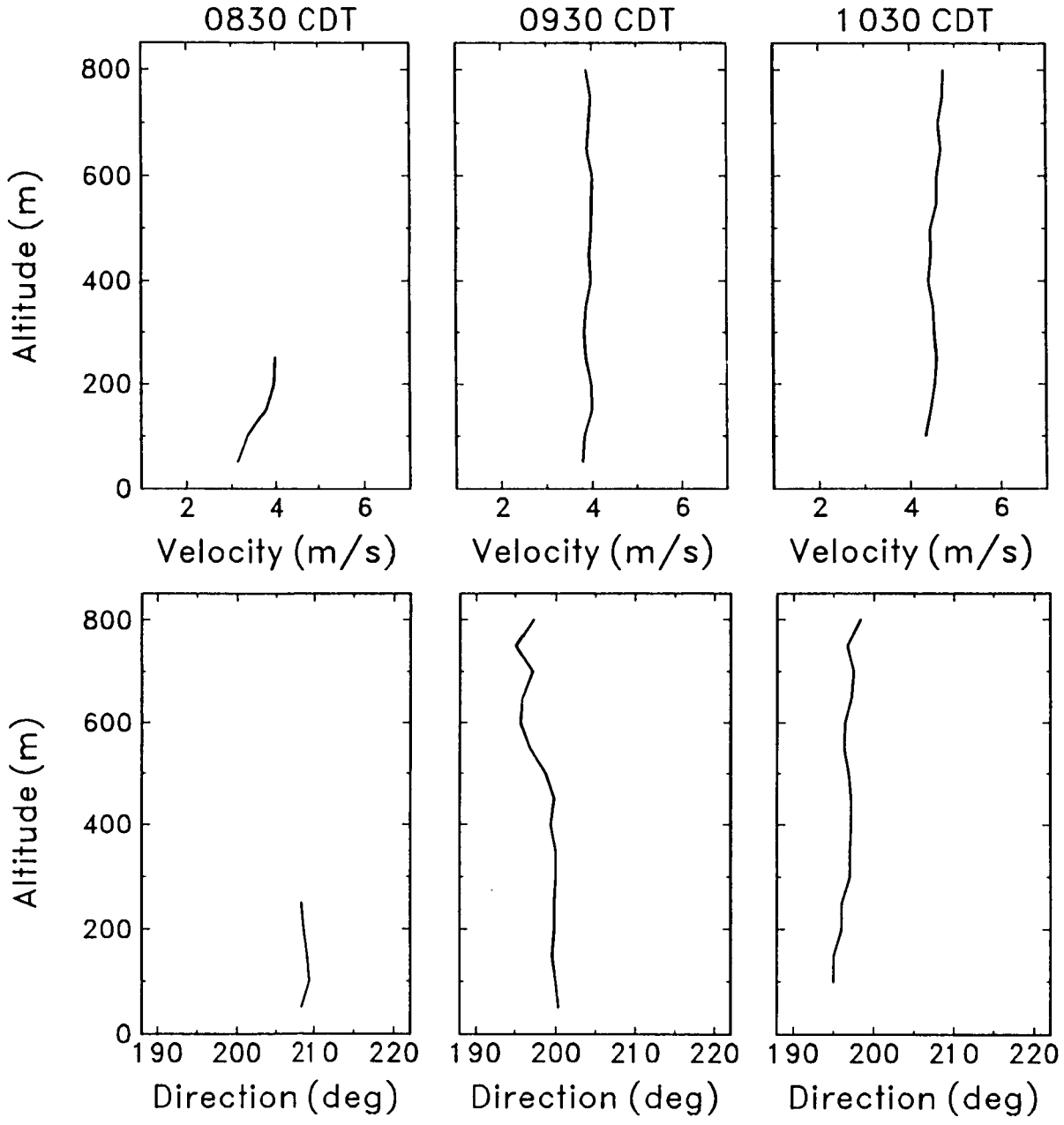
0830 CDT
0930 CDT
1030 CDT
Altitude (m)
800
600
400
200
0
2
4
6
Velocity (m/s)
190
200
210
220
Direction (deg)

Fig. 6

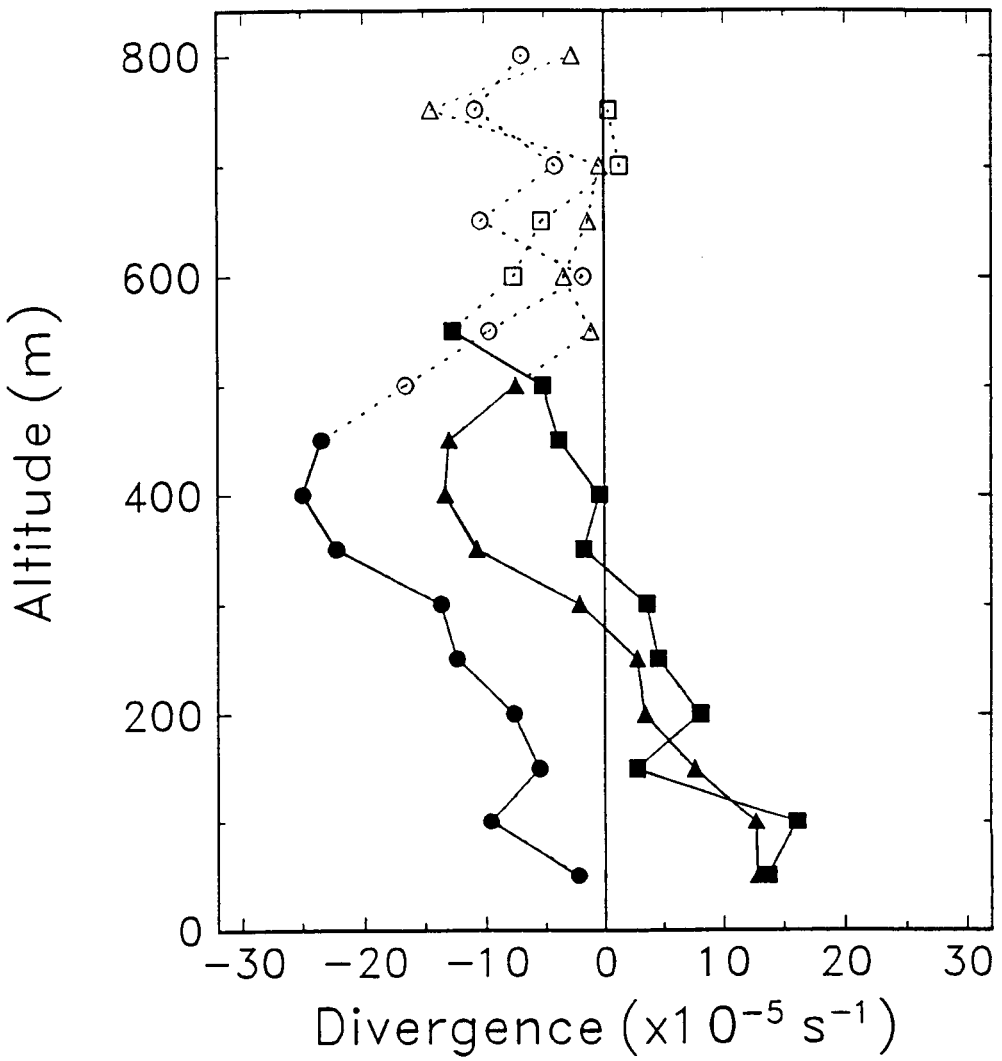
800
600
400
200
0
Altitude (m)
−30
−20
−10
0
10
20
30
Divergence (x10^{-5} s^{-1})

Fig. 7

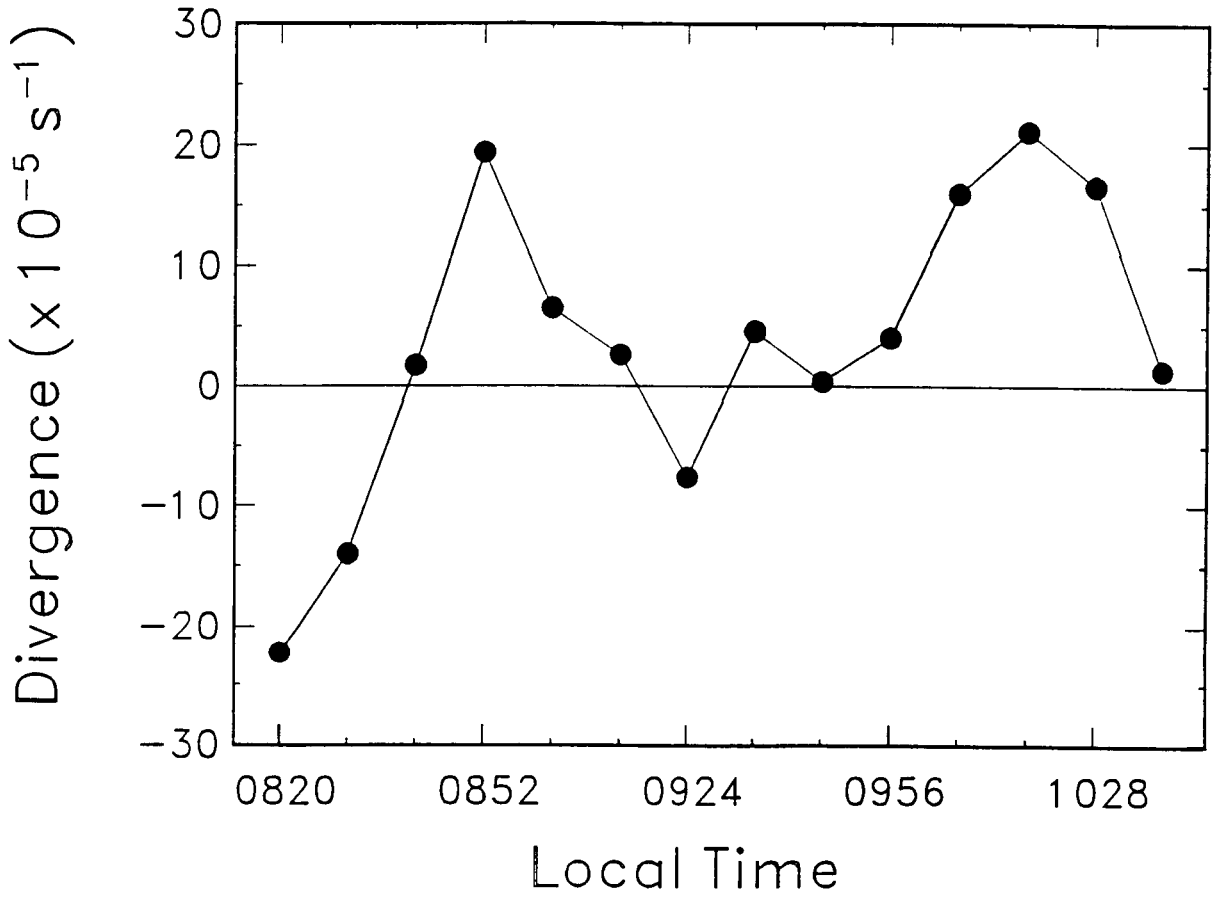
Divergence (x 10^{-5} s^{-1})
30
20
10
0
−10
−20
−30
0820
0852
0924
0956
1028
Local Time

Fig. 8

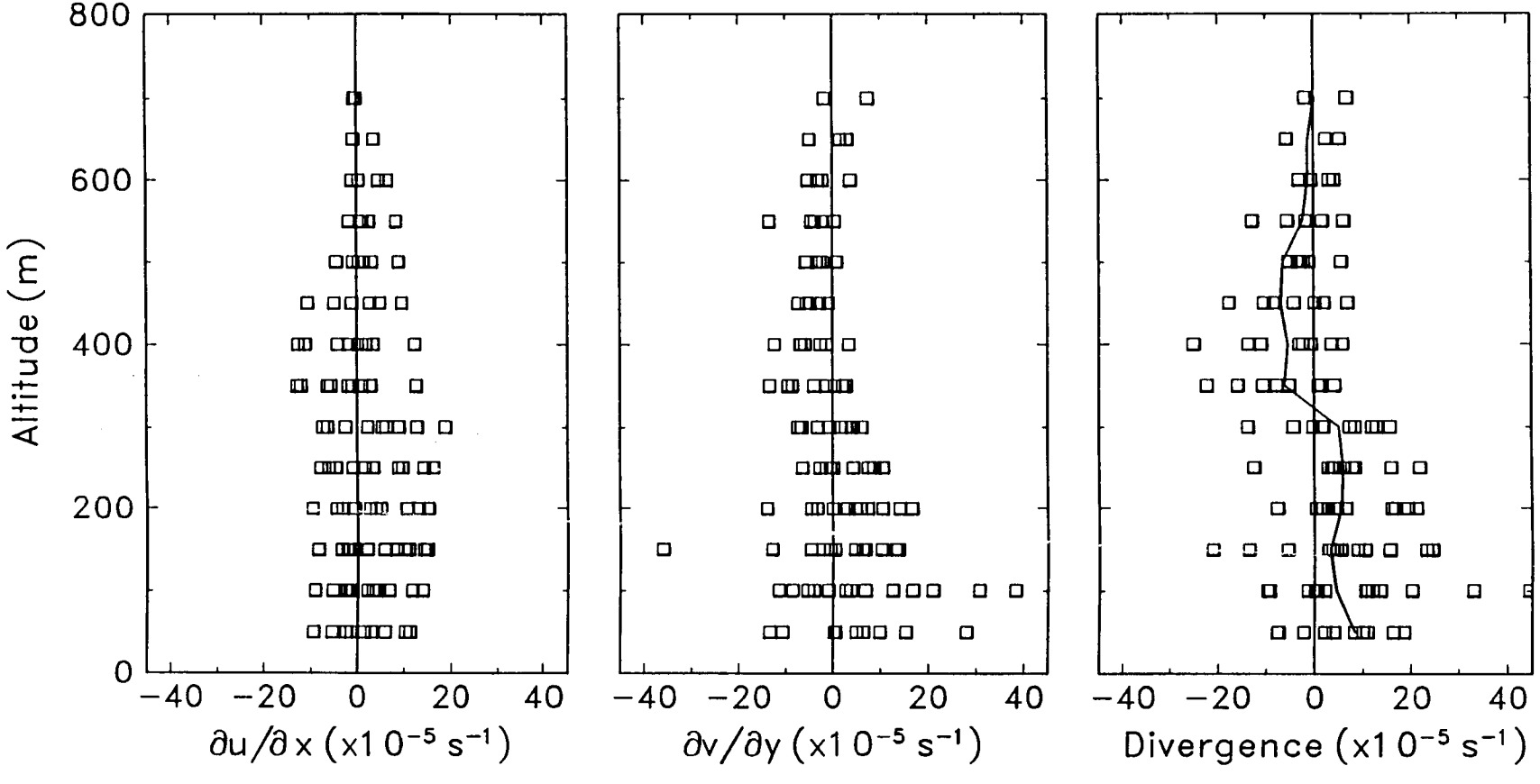
800
600
400
200
0
Altitude (m)
−40 −20 0 20 40
∂u/∂x (x10⁻⁵ s⁻¹)
−40 −20 0 20 40
∂v/∂y (x10⁻⁵ s⁻¹)
−40 −20 0 20 40
Divergence (x10⁻⁵ s⁻¹)

Fig. 9